PHYSICAL REVIEW C **111**, 035202 (2025)

Measurement of the nucleon spin structure functions for $0.01 < Q^2 < 1\,\mathrm{GeV}^2$ using CLAS

A. Deur,[34,47,29] S. E. Kuhn,[29] M. Ripani,[18] X. Zheng,[47,*] A. G. Acar,[48] P. Achenbach,[34] K. P. Adhikari,[29,34,25]
J. S. Alvarado,[39] M. J. Amaryan,[29] W. R. Armstrong,[1] H. Ataç,[33] H. Avakian,[34] L. Baashen,[12] N. A. Baltzell,[34,46] L. Barion,[16]
M. Bashkanov,[48] M. Battaglieri,[18] B. Benkel,[20] F. Benmokhtar,[10] A. Bianconi,[35,19] A. S. Biselli,[11] W. A. Booth,[48] F. Bossù,[7]
P. Bosted,[34,†] S. Boiarinov,[34] K.-Th. Brinkmann,[30] W. J. Briscoe,[14] S. Bueltmann,[29] V. D. Burkert,[34] D. S. Carman,[34]
P. Chatagnon,[34] J.-P. Chen,[34] G. Ciullo,[16,36] P. L. Cole,[23] M. Contalbrigo,[16] V. Crede,[13] A. D'Angelo,[37,20] N. Dashyan,[49]
R. De Vita,[18,‡] M. Defurne,[7] S. Diehl,[30,41] C. Djalali,[28] V. A. Drozdov,[32] R. Dupre,[39] H. Egiyan,[34,44] A. El Alaoui,[38]
L. El Fassi,[25,1] L. Elouadrhiri,[34] P. Eugenio,[13] J. C. Faggert,[47,15] S. Fegan,[48] R. Fersch,[8,9,§] A. Filippi,[21] K. Gates,[42]
G. Gavalian,[34,29] G. P. Gilfoyle,[45] R. W. Gothe,[46] L. Guo,[12,34] H. Hakobyan,[38,49] M. Hattawy,[29] F. Hauenstein,[34] D. Heddle,[8,34]
A. Hobart,[39] M. Holtrop,[44] D. G. Ireland,[42] E. L. Isupov,[32] H. Jiang,[42] H. S. Jo,[22] S. Joosten,[1] H. Kang,[31] C. Keith,[34]
M. Khandaker,[27,‖] W. Kim,[22] F. J. Klein,[6] V. Klimenko,[41] P. Konczykowski,[7] K. Kovacs,[47] A. Kripko,[30] V. Kubarovsky,[34]
L. Lanza,[20,37] S. Lee,[1] P. Lenisa,[16,36] X. Li,[24] E. Long,[44] I. J. D. MacGregor,[42] D. Marchand,[39] V. Mascagna,[35,19]
D. Matamoros,[39] B. McKinnon,[42] D. Meekins,[34] S. Migliorati,[35,19] T. Mineeva,[38] M. Mirazita,[17] V. Mokeev,[34,32]
C. Munoz Camacho,[39] P. Nadel-Turonski,[34,14] T. Nagorna,[18] K. Neupane,[46] S. Niccolai,[39] M. Osipenko,[18] A. I. Ostrovidov,[13]
P. Pandey,[24] M. Paolone,[26] L. L. Pappalardo,[16,36] R. Paremuzyan,[34] E. Pasyuk,[34,2] S. J. Paul,[40] W. Phelps,[8,34] S. K. Phillips,[44]
J. Pierce,[47,¶] N. Pilleux,[39] M. Pokhrel,[29] J. W. Price,[3] Y. Prok,[29,47] A. Radic,[38] Trevor Reed,[12] J. Richards,[41] G. Rosner,[42]
P. Rossi,[34,17] A. A. Rusova,[32] C. Salgado,[27] A. Schmidt,[14] R. A. Schumacher,[5] Y. G. Sharabian,[34] E. V. Shirokov,[32]
U. Shrestha,[41] S. Širca,[43] N. Sparveris,[33] M. Spreafico,[18] S. Stepanyan,[34] I. I. Strakovsky,[14] S. Strauch,[46] V. Sulkosky,[24]
J. A. Tan,[22] M. Tenorio,[29] N. Trotta,[41] R. Tyson,[34] M. Ungaro,[34,41] D. W. Upton,[47,29] S. Vallarino,[18] L. Venturelli,[35,19]
H. Voskanyan,[49] E. Voutier,[39] D. P. Watts,[48] X. Wei,[34] M. H. Wood,[4,46] N. Zachariou,[48] J. Zhang,[47,29] and M. Zurek[1]
(The CLAS Collaboration)

[1]*Argonne National Laboratory, Argonne, Illinois 60439, USA*
[2]*Arizona State University, Tempe, Arizona 85287, USA*
[3]*California State University, Dominguez Hills, Carson, California 90747, USA*
[4]*Canisius College, Buffalo, New York 14208, USA*
[5]*Carnegie Mellon University, Pittsburgh, Pennsylvania 15213, USA*
[6]*Catholic University of America, Washington, D.C. 20064, USA*
[7]*CEA, IRFU,Université Paris-Saclay, F-91191 Gif-sur-Yvette, France*
[8]*Christopher Newport University, Newport News, Virginia 23606, USA*
[9]*College of William and Mary, Williamsburg, Virginia 23187, USA*
[10]*Duquesne University, 600 Forbes Avenue, Pittsburgh, Pennsylvania 15282, USA*
[11]*Fairfield University, Fairfield, Connecticut 06824, USA*
[12]*Florida International University, Miami, Florida 33199, USA*
[13]*Florida State University, Tallahassee, Florida 32306, USA*
[14]*The George Washington University, Washington, D.C. 20052, USA*
[15]*Georgia Institute of Technology, Atlanta, Georgia 30332, USA*
[16]*INFN, Sezione di Ferrara, 44100 Ferrara, Italy*
[17]*INFN, Laboratori Nazionali di Frascati, 00044 Frascati, Italy*
[18]*INFN, Sezione di Genova, 16146 Genova, Italy*
[19]*INFN, Sezione di Pavia, 27100 Pavia, Italy*
[20]*INFN, Sezione di Roma Tor Vergata, 00133 Rome, Italy*
[21]*INFN, Sezione di Torino, 10125 Torino, Italy*
[22]*Kyungpook National University, Daegu 41566, Republic of Korea*
[23]*Lamar University, 4400 MLK Boulevard, P.O. Box 10046, Beaumont, Texas 77710, USA*
[24]*Massachusetts Institute of Technology, Cambridge, Massachusetts 02139, USA*

---

[*] Contact author: xiaochao@jlab.org

[†] Present address: College of William and Mary, Williamsburg, Virginia 23187, USA.

[‡] Present address: Thomas Jefferson National Accelerator Facility, Newport News, Virginia 23606, USA.

[§] Deceased.

[‖] Present address: Idaho State University, Pocatello, Idaho 83209, USA.

[¶] Present address: Oak Ridge National Laboratory, 1 Bethel Valley Road, Oak Ridge, Tennessee 37830, USA.

2469-9985/2025/111(3)/035202(34)

[25]*Mississippi State University, Mississippi State, Mississippi 39762, USA*
[26]*New Mexico State University, PO Box 30001, Las Cruces, New Mexico 88003, USA*
[27]*Norfolk State University, Norfolk, Virginia 23504, USA*
[28]*Ohio University, Athens, Ohio 45701, USA*
[29]*Old Dominion University, Norfolk, Virginia 23529, USA*
[30]*II Physikalisches Institut der Universitãt Giessen, 35392 Giessen, Germany*
[31]*Seoul National University, Seoul 08826, Republic of Korea*
[32]*Skobeltsyn Institute of Nuclear Physics, Lomonosov Moscow State University, 119234 Moscow, Russia*
[33]*Temple University, Philadelphia, Pennsylvania 19122, USA*
[34]*Thomas Jefferson National Accelerator Facility, Newport News, Virginia 23606, USA*
[35]*Università di Brescia, 25123 Brescia, Italy*
[36]*Università di Ferrara, 44121 Ferrara, Italy*
[37]*Università di Roma Tor Vergata, 00133 Rome, Italy*
[38]*Universidad Técnica Federico Santa María, Casilla 110-V Valparaíso, Chile*
[39]*Université Paris-Saclay, CNRS/IN2P3, IJCLab, 91405 Orsay, France*
[40]*University of California Riverside, 900 University Avenue, Riverside, California 92521, USA*
[41]*University of Connecticut, Storrs, Connecticut 06269, USA*
[42]*University of Glasgow, Glasgow G12 8QQ, United Kingdom*
[43]*University of Ljubljana, 1000 Ljubljana, Slovenia*
[44]*University of New Hampshire, Durham, New Hampshire 03824, USA*
[45]*University of Richmond, Richmond, Virginia 23173, USA*
[46]*University of South Carolina, Columbia, South Carolina 29208, USA*
[47]*University of Virginia, Charlottesville, Virginia 22904, USA*
[48]*University of York, York YO10 5DD, United Kingdom*
[49]*Yerevan Physics Institute, 375036 Yerevan, Armenia*

(Received 20 September 2024; accepted 28 January 2025; published 25 March 2025)

The spin structure functions of the proton and the deuteron were measured during the EG4 experiment at Jefferson Lab in 2006. Data were collected for longitudinally polarized electron scattering off longitudinally polarized NH_3 and ND_3 targets, for Q^2 values as small as 0.012 and 0.02 GeV^2, respectively, using the CEBAF Large Acceptance Spectrometer. This is the archival paper of the EG4 experiment that summarizes the previously reported results of the polarized structure functions g_1, A_1F_1, and their moments $\overline{\Gamma}_1$, $\overline{\gamma}_0$, and $\overline{I}_{\rm TT}$, for both the proton and the deuteron. In addition, we report on new results on the neutron g_1 extracted by combining proton and deuteron data and correcting for Fermi smearing, and on the neutron moments $\overline{\Gamma}_1$, $\overline{\gamma}_0$, and $\overline{I}_{\rm TT}$ formed directly from those of the proton and the deuteron. Our data are in good agreement with the Gerasimov-Drell-Hearn sum rule for the proton, deuteron, and neutron. Furthermore, the isovector combination was formed for g_1 and the Bjorken integral $\overline{\Gamma}_1^{p-n}$, and it was compared to available theoretical predictions. All of our results, to the best of our knowledge, provide for the first time extensive tests of spin observable predictions from chiral effective field theory (χEFT) in a Q^2 range commensurate with the pion mass. They motivate further improvement in χEFT calculations from other approaches such as the lattice gauge method.

DOI: 10.1103/PhysRevC.111.035202

I. INTRODUCTION

The study of nucleon structure has been an active field of research ever since the discovery that nucleons were composite [1–3]. It is now well known that the nucleon, like all hadrons, is made of partons (quarks, antiquarks, and gluons) and that its structure is dominantly ruled by the strong nuclear interaction described by quantum chromodynamics (QCD) [4,5]. However, the behavior of the QCD coupling constant α_s [6–8] determines that our understanding of nucleon structure at long distance is not as developed as that at short distance. At high energy-momentum (short distance) typically well above the GeV scale, $\alpha_s \ll 1$, which allows us to treat QCD perturbatively. Presently, the approximations of observables are typically known to order α_s^3, and some to α_s^5. However, at low-energy momentum, $\alpha_s \gtrsim 1$, and a perturbative expansion in α_s becomes inapplicable. The problem is further complicated by the rise of complex phenomena, e.g., the confinements of partons, the emergence of hadronic degrees of freedom or the spontaneous breaking of QCD's near $SU(3)_L \times SU(3)_R$ chiral symmetry. In this domain, due to the lack of a mature analytic technique based on the QCD Lagrangian, effective theories or models are often used. In particular, chiral effective field theory (χEFT) [9], based on the observed spontaneous breaking of the chiral symmetry in hadronic states, has successfully predicted hadronic observables at low energies.

The principle of χEFT is that it describes the nucleon in terms of effective hadronic degrees of freedom instead of the fundamental quark and gluon fields. It is completely nonperturbative in terms of α_s because it employs series whose expansion parameters are based, *e.g.*, on the pion mass, the nucleon-Δ_{1232} mass gap or the characteristic energy scale of the chiral symmetry breaking. However, while leading-order (LO) calculations of χEFT are relatively tractable, next-to-leading-order (NLO) and higher order calculations are much more involved. An important experimental task is therefore to provide precise hadron structure data that can test, and potentially guide, χEFT calculations and other approaches to nonperturbative QCD. Such data must cover the domain of low momentum transfer squared (Q^2) where χEFT applies, typically below a few tenths of GeV^2. Especially important in this context are low Q^2 nucleon spin structure data [10–18] which are challenging to obtain experimentally but are crucial for the development of χEFT [19]. One such experimental endeavor is that of the Jefferson Lab (JLab) Experimental Group EG4, constituted of experiments E03-006 and E05-111 that used the CEBAF Large Acceptance Spectrometer (CLAS) in Hall B [20]. EG4 was designed to test χEFT predictions by precisely measuring the longitudinal spin structure function g_1 and its moments for the proton and the deuteron down to $Q^2 \simeq 0.01$ GeV^2. These low Q^2 data, reported in two letters [21,22], provided benchmarks for χEFT calculations. This document is the archival article that presents in detail the EG4 experiments, data analysis procedure for the inclusive scattering channel, results on the proton and the deuteron, and followup analysis and results on the neutron spin structure functions. Additional results on the target- and double-spin asymmetries of pion electroproduction are available [23], but these were focused on the semi-inclusive channel and are not included here.

The article is arranged as follows: In Sec. II we present the formalism of unpolarized and polarized electron scattering. We introduce the nucleon structure functions, their moments, and polarized sum rules, which are relevant not only for testing χEFT but also to form observables that have no known method of direct measurement. In Sec. III we describe EG4 and the special features that distinguish it from other CLAS experiments. In Sec. IV we describe the analysis procedure of extracting the polarized yield differences from the data. In Sec. V we describe the Monte Carlo simulation, the normalization of the data using the elastic scattering yield, and the extraction of the structure function g_1. In Sec. VI A we present results on g_1, A_1F_1 of the proton and the deuteron, followed by the procedure to extract the neutron g_1 results in Sec. VI B. We present results for and discussions of all the moments in Sec. VII. We then summarize, conclude, and provide perspectives in Sec. VIII. All results on the structure functions and their moments reported in this article are included as Supplemental Material [24].

II. FORMALISM

All formalism presented in this section is based on Ref. [10] or Ref. [14], and the algebraic manipulations therein.

A. Inclusive electron scattering

Within the approximation of one-photon exchange between the lepton and the target (Fig. 1), the scattering process is described by two kinematic variables: the virtuality of the exchanged photon $Q^2 \equiv -q^2$ and the invariant mass of the photon-target system $W \equiv \sqrt{(q+P)^2}$. The virtual photon can be viewed as a probe of the substructure of the target nucleus (or nucleon) and Q^2 describes the (inverse) space-time resolution of the probe. For the fixed-target case, one has

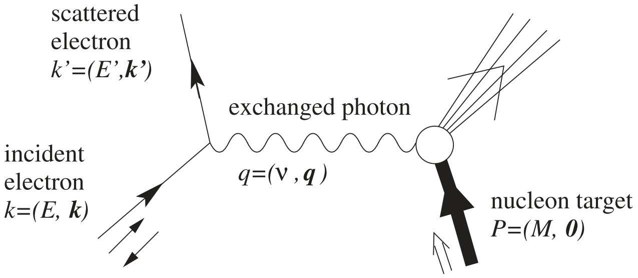

FIG. 1. The one-photon exchange process of polarized electron scattering off a polarized nucleon. The 4-momenta of the incident and the scattered electrons are $k = (E, \boldsymbol{k})$ and $k' = (E', \boldsymbol{k}')$, respectively, and the helicity of the incident electron is indicated by the thin arrows. The nucleon target, if at rest, has $P = (M, \boldsymbol{0})$ and its spin is indicated by the outlined arrow.

$$Q^2 = 2EE'(1-\cos\theta), \tag{1}$$

where θ is the scattering angle of the electron, i.e., the angle formed by $\boldsymbol{k}$ and $\boldsymbol{k}'$, and

$$W_{\text{nucl}} = \sqrt{M_T^2 + 2M_T\nu - Q^2}. \tag{2}$$

Here M_T is usually the mass of the nuclear target in the case of nuclear scattering. However, when we study inelastic scattering from the nucleons, the nucleon mass M is used instead:

$$W = \sqrt{M^2 + 2M\nu - Q^2}. \tag{3}$$

Unless indicated otherwise, Eq. (3) will be used hereafter for the definition of the invariant mass. Alternatively to W, one may characterize the scattering process using the Bjorken scaling variable [25] $x \equiv -q^2/(2P\cdot q) = Q^2/(W^2 - M^2 + Q^2)$, or for fixed targets:

$$x = \frac{Q^2}{2M\nu}. \tag{4}$$

B. Cross sections and structure functions

For inclusive unpolarized inelastic scattering off a spin-1/2 target, the differential cross section for detecting the final-state lepton in the solid angle dΩ and in the final energy range (E', $E' + \mathrm{d}E'$) in the laboratory frame can be written as

$$\frac{\mathrm{d}^2\sigma_u}{\mathrm{d}\Omega \mathrm{d}E'} = \left(\frac{\mathrm{d}^2\sigma}{\mathrm{d}\Omega}\right)_{\text{Mott}} \times\left[\frac{1}{\nu}F_2(x,Q^2) + \frac{2}{M}F_1(x,Q^2)\tan^2\frac{\theta}{2}\right], \tag{5}$$

where $F_1(x,Q^2)$ and $F_2(x,Q^2)$ are the two unpolarized structure functions characterizing the target structure for unpolarized inclusive lepton scattering. The Mott cross section (representing scattering off a point-like, spinless, infinitely heavy target) is

$$\left(\frac{d^2\sigma}{d\Omega}\right)_{\text{Mott}} = \frac{\alpha^2 \cos^2\frac{\theta}{2}}{4E^2 \sin^4\frac{\theta}{2}}, \tag{6}$$

with α the quantum electrodynamics (QED) coupling.

In the polarized case where the electrons and the spin-1/2 target are polarized along the beam direction, the helicity-dependent cross section difference is

$$\begin{aligned}\frac{d^2\sigma_{\uparrow\Uparrow}}{d\Omega dE'} - \frac{d^2\sigma_{\uparrow\Downarrow}}{d\Omega dE'} &= -\frac{4\alpha^2 E'}{M\nu E Q^2}\left[(E + E'\cos\theta)g_1(x, Q^2) - 2Mxg_2(x, Q^2)\right] \\ &= -\frac{4\alpha^2 E'}{M\nu E Q^2}\left[\left(E + E'\cos\theta + \frac{Q^2}{\nu}\right)g_1 - \frac{Q^2}{\nu}F_1 A_2\right],\end{aligned} \tag{7}$$

where the $\uparrow$ ($\downarrow$) and $\Uparrow$ ($\Downarrow$) represent the electron and the target spin directions being parallel (antiparallel) to the beam direction, respectively. The spin-dependent properties of the target are characterized for inclusive lepton scattering by $g_1(x, Q^2)$ and $g_2(x, Q^2)$, the longitudinal and transverse polarized structure functions, respectively. The second line on the right-hand side (RHS) of Eq. (7) indicates that one can extract $g_1(x, Q^2)$ from this cross section difference assuming a model for the product $F_1(x, Q^2)A_2(x, Q^2)$, where A_2 is the virtual photon asymmetry to be defined in the next section.

C. Virtual photon cross sections

The formalism provided in the previous two sections focused on the interaction cross section between the incident electron and the target. It is often useful to also study cross sections for the virtual photon being absorbed by the target, and their dependence on the photon polarization. We follow the formalism of Refs. [5,26,27].

The photon polarization 4-vector, e^μ, includes two transverse polarization modes that satisfy $e_T^2 = -1$ and a longitudinal polarization mode that satisfies $e_L^2 = 1$. The total cross section of the photon absorption by the spin-1/2 target can be separated into two terms: the longitudinal and transverse virtual photon cross sections

$$\sigma_L = \frac{4\pi^2\alpha}{K}\left[\left(1 + \frac{\nu^2}{Q^2}\right)\frac{F_2}{\nu} - \frac{F_1}{M}\right], \tag{8}$$

$$\sigma_T = \frac{4\pi^2\alpha}{K}\left[\frac{F_1}{M}\right], \tag{9}$$

which are associated with the longitudinally and transversely polarized virtual photons, respectively. The virtual photon equivalent energy K (sometimes called virtual photon flux) in Eqs. (8) and (9) is not a direct observable and different definitions have been proposed: the Hand convention $K_H \equiv \nu(1 - x)$, the Gilman convention $K_G \equiv \sqrt{\nu^2 + Q^2}$, or using the photon energy $K_A \equiv \nu$. For now, we will continue to use K instead of choosing a convention. The ratio of the longitudinal to transverse cross sections R is

$$R \equiv \frac{\sigma_L}{\sigma_T} = \frac{F_2}{2xF_1}(1 + \gamma^2) - 1, \tag{10}$$

where

$$\gamma^2 = \frac{Q^2}{\nu^2} = \frac{(2Mx)^2}{Q^2}. \tag{11}$$

Using the "relative longitudinal polarization" [1] of the virtual photon ϵ, the total photon absorption cross section can be written as

$$\frac{d^2\sigma_u}{d\Omega dE'} = \Gamma(\sigma_T + \epsilon\sigma_L), \tag{12}$$

with

$$\epsilon = \frac{1}{[1 + 2(1 + 1/\gamma^2)\tan^2(\theta/2)]}, \tag{13}$$

and the photon flux factor Γ

$$\Gamma = \frac{\alpha}{2\pi^2}\frac{E'}{E}\frac{K}{Q^2}\frac{1}{1 - \epsilon}. \tag{14}$$

For the polarized case, one can similarly divide the virtual photon absorption cross section by a spin-1/2 target into several components based on the polarization of the photon, and the total spin of the photon and the target projected along the direction of the photon momentum $\boldsymbol{q}$ (1/2 and 3/2 for the photon spin antiparallel and parallel to the target spin, respectively), and a component σ_I resulting from the interference between transverse and longitudinal virtual photon-nucleon amplitudes [5]. From these components one further defines

$$\sigma_T = (\sigma_{1/2} + \sigma_{3/2})/2, \tag{15}$$

$$\sigma_{\text{TT}} = (\sigma_{1/2} - \sigma_{3/2})/2, \tag{16}$$

$$\sigma_{\text{LT}} = \sigma_I. \tag{17}$$

These spin-dependent virtual photon cross sections relate to the nucleon polarized structure functions as

$$\sigma_{\text{LT}} = \frac{4\pi^2\alpha}{MK}\gamma(g_1 + g_2), \tag{18}$$

$$\sigma_{\text{TT}} = \frac{4\pi^2\alpha}{MK}(g_1 - \gamma^2 g_2). \tag{19}$$

Finally, two virtual photon asymmetries are also commonly employed. The first is the longitudinal asymmetry A_1:

$$A_1 \equiv \frac{\sigma_{\text{TT}}}{\sigma_T} = \frac{g_1 - \gamma^2 g_2}{F_1}, \tag{20}$$

from which we obtain

$$\sigma_{\text{TT}} = \frac{4\pi^2\alpha}{MK}A_1 F_1. \tag{21}$$

---

[1] It is called "photon transverse polarization" in Ref. [26]. However, since this is the weighting factor of σ_L, not σ_T, we prefer "relative longitudinal polarization."

The second is the longitudinal-transverse interference asymmetry:

$$A_2 \equiv \frac{\sigma_{\rm LT}}{\sigma_T} = \frac{\gamma(g_1+g_2)}{F_1}. \tag{22}$$

The asymmetries A_1, A_2, and g_1/F_1 are related as

$$A_1 + \gamma A_2 = (1+\gamma^2)\frac{g_1}{F_1}. \tag{23}$$

Note that one can use either $g_{1,2}$ or $A_{1,2}F_1$ to describe the polarized cross section, Eq. (7).

D. Sum rules and moments of structure functions

In this section we present the Bjorken, GDH, generalized GDH, and generalized polarizability sum rules, which all involve moments of polarized structure functions or, equivalently, $\sigma_{\rm TT}$ and $\sigma_{\rm LT}$. For reviews of nucleon spin structure and additional sum rules, see Refs. [12,14,15,17].

1. Bjorken sum rule

The Bjorken sum rule, derived for $Q^2 \to \infty$ using current algebra and isospin symmetry [28,29], predates QCD and is not a QCD prediction. However, its generalization to include the Q^2-dependence appearing at finite Q^2 [30–32] stems from pQCD. Studying the sum rule in the pQCD domain ($Q^2 \gtrsim 1$ GeV^2) therefore tests whether QCD correctly describes the strong force when spin degrees-of-freedom are explicit. The Bjorken sum has been actively measured at CERN [33–41], DESY [42], JLab [43–45], and SLAC [46–51], with measurement agreeing to better than 10% with the sum rule expectation [17]. Measurements performed with the higher-energy accelerators, CERN and SLAC, provide data at larger Q^2 values, offering extensive coverage of the low-x part of the Bjorken sum. Measurements at the lower-energy facilities, DESY and JLab, covered the smaller Q^2 range while overlapping with the SLAC data. Due to their lower energy, DESY and JLab have a limited low-x reach, which is supplemented by extrapolating the low-x data obtained from CERN and SLAC.

The original Bjorken sum rule ($Q^2 \to \infty$) reads

$$\Gamma_1^{p-n}(Q^2)|_{Q^2\to\infty} = \int_0^1 \left[g_1^p(x,Q^2) - g_1^n(x,Q^2)\right]dx = \frac{g_a}{6}, \tag{24}$$

where g_a is the axial coupling constant measured in neutron beta decay. Equation (24) can be generalized for finite Q^2 by accounting for gluon radiation and higher-twist (HT) effects:

$$\Gamma_1^{p-n}(Q^2) = \frac{g_a}{6} f(Q^2) + \text{HT}, \tag{25}$$

where [30]

$$f(Q^2) = 1 - \frac{\alpha_s(Q^2)}{\pi} - 3.58\left(\frac{\alpha_s(Q^2)}{\pi}\right)^2 - 20.2\left(\frac{\alpha_s(Q^2)}{\pi}\right)^3 - 175.7\left(\frac{\alpha_s(Q^2)}{\pi}\right)^4 + \mathcal{O}(\alpha_s^5), \tag{26}$$

and HT contains higher-twist corrections proportional to powers of $1/Q^2$.

Beside the pQCD domain, the Bjorken sum rule is also important at low Q^2 due to its close connection to the GDH sum rule (see next section). The behavior of the Bjorken sum at $Q^2 < 1$ GeV^2 was precisely mapped by several experiments at JLab [43,44,52,53]. Note that Eqs. (24)–(26) are not valid in the low Q^2 domain and Bjorken sum rule predictions are provided by either models using nonperturbative approaches [54–59] or χEFT calculations [60,61].

2. Gerasimov-Drell-Hearn (GDH) sum rule

The GDH sum rule [62–64] is based on dispersion relations, unitarity, relativity, and gauge invariance and is derived for real photoproduction ($Q^2 = 0$). Like the Bjorken sum rule, the GDH sum rule is derived in a more general context than that of QCD and also predates it. In particular, the GDH sum rule applies to any type of target. For targets whose internal structure is governed by the strong interaction, such as nucleons and nuclei, the sum rule provides a path to study QCD [17]. For real photons, the GDH sum rule gives

$$\int_{\nu_{\rm thr}}^{\infty} \frac{\sigma_A - \sigma_P}{\nu} d\nu = -4\pi^2\alpha \frac{\kappa^2}{M_T^2} S, \tag{27}$$

where σ_A and σ_P are the photo-absorption cross sections for target and photon spins antiparallel (A) and parallel (P). [For spin-1/2 targets, these are the same as $\sigma_{1/2}$ and $\sigma_{3/2}$ in Eqs. (15) and (16).] Here, M_T and S are the mass and the spin of the target, and $\nu_{\rm thr}$ is the minimal photon energy for inelastic excitation of the target. In the context of (virtual) photon absorption on a nucleon, this threshold energy corresponds to the pion production threshold:

$$\nu_{\rm thr} = m_\pi + \frac{m_\pi^2 + Q^2}{2M}, \tag{28}$$

with m_π the pion mass. The anomalous magnetic moment of the target κ is defined by the total magnetic moment of the particle $\boldsymbol{\mu} = \frac{e(Q/e+\kappa)}{M_T}\boldsymbol{S}$ with Q/e the charge of the target in units of the elementary charge, and can be related to the gyromagnetic ratio g as $\kappa = g/2 - Q/e$. The RHS of Eq. (27) is −204 µb for the proton ($S = \frac{1}{2}$, $\kappa = 1.793$, and $g/2 = 2.793$), −234 µb for the neutron ($S = \frac{1}{2}$, $\kappa = -1.913$, and $g/2 = -1.913$), and 0.65 µb for the deuteron ($S = 1$, $\kappa = -0.143$, and $g/2 = 0.857$). Whereas the overall consensus [64] is that the GDH sum rule is theoretically very solid, the question of its validity has been debated, mainly regarding whether $\sigma_{\rm TT}/\nu$ decreases fast enough with ν for the integral to converge. Concurrently, its experimental verification has been the focus of several experiments at MAMI and ELSA [65–69], BNL [70], JLab [21,71], GRAAL (ESRF) [72], and HIGS (TUNL) [73] providing results that show, given reasonable assumptions for the large ν behavior of its integrand, the GDH sum rule is valid for the proton to within the 10% precision of the world data [21,22,64,74].

The GDH integral for the nucleon, when expressed with spin structure functions using Eq. (19), is an integral over g_1 [75]. Like the Bjorken sum, the small correction from g_2 vanishes when $Q^2 \to 0$, see Eq. (11). Therefore, the formal expression of the (isovector) GDH and Bjorken integrals are proportional, whereas the domains of applicability of the sum rules are disjoint at high Q^2 and $Q^2 = 0$, respectively. Several methods have been proposed to bridge the two sum rules. Generalization to finite Q^2 values for the left-hand side of Eq. (27) is straightforward since $\sigma_{\rm TT}$ or equivalently g_1 and g_2 exist also at nonzero Q^2. A commonly used definition is [10,27]

$$\bar{I}_{\rm TT}(Q^2) \equiv \frac{M^2}{8\pi^2\alpha}\int_{\nu_{\rm thr}}^{\infty}\frac{K}{\nu}\frac{\sigma_{\rm TT}}{\nu}d\nu. \tag{29}$$

Note that hereafter in this article, a line above a symbol signifies that it does not include the contribution from elastic scattering. At finite Q^2, Eq. (29) can be expanded using Eq. (21):

$$\bar{I}_{\rm TT}(Q^2) = \frac{M^2}{8\pi^2\alpha}\int_{\nu_{\rm thr}}^{\infty}\frac{K}{\nu}2\frac{\frac{4\pi^2\alpha}{MK}A_1F_1}{\nu}d\nu$$
$$= \frac{2M^2}{Q^2}\int_0^{x_{\rm th}} A_1F_1dx, \tag{30}$$

where $dx = (Q^2/2M\nu^2)d\nu$ was used in the last step. The integral $\bar{I}_{\rm TT}$ can thus be treated as a generalized form of the GDH integral and can be determined from the measured values of A_1F_1.

The $Q^2 \to 0$ limit for the integral of Eq. (29) can be obtained by multiplying the RHS of Eq. (27) by the extra factor $(\frac{1}{2})M^2/(8\pi^2\alpha)$. Since at $Q^2 = 0$, $\frac{K}{\nu} = 1$, it reads

$$\bar{I}_{\rm TT}(Q^2 = 0) = -\frac{\kappa^2}{4}. \tag{31}$$

Therefore, measuring $\bar{I}_{\rm TT}$ at very low Q^2 also allows one to test the GDH sum rule.

Using $\bar{I}_{\rm TT}$, the Bjorken sum can be extrapolated to the real photon point as

$$\bar{\Gamma}_1^{p-n}(Q^2)|_{Q^2\to 0} = \frac{Q^2}{2M^2}\bar{I}_{\rm TT}^{p-n} = \frac{Q^2}{8}\left(\frac{\kappa_n^2}{M_n^2} - \frac{\kappa_p^2}{M_p^2}\right), \tag{32}$$

which should have a positive slope given $\kappa_n^2/M_n^2 > \kappa_p^2/M_p^2$.

The above procedure generalizes only the GDH integral but not the GDH sum rule, i.e., the RHS of Eq. (27). Other possible generalizations of the GDH integral as reviewed in Ref. [26] share the same caveat. To generalize the sum rule itself, one needs to note that the integral of g_1 can be related to the first forward virtual Compton scattering amplitude $S_1(\nu, Q^2)$ [14,17,76] using the low-energy theorem [77].

Accordingly, a full generalization of the GDH sum rule is [76]

$$\bar{\Gamma}_1(Q^2) = \int_0^{1^-} g_1(x, Q^2)dx = \frac{Q^2}{8}\bar{S}_1(0, Q^2), \tag{33}$$

where the bars and 1^- indicate that the $x = 1$ elastic contribution (quasielastic for nuclear targets) is excluded. In the quark-parton model, this integral gives the quark polarization within the nucleon weighted by their electric charge squared, and provides one of the ingredients for Ellis-Jaffe sum rule [78] and Bjorken sum rule. For the generalized form of the GDH sum rule, Eq. (33), the amplitude $\bar{S}_1(0, Q^2)$ can be calculated in χEFT if Q^2 is sufficiently low [60,61,79–85]. The generalized GDH integrals have been measured over an extensive Q^2 range and on proton, neutron, deuteron and ^{3}He by CERN [33–41,86–89], DESY [42,90,91], JLab [21,22,52,71,92–104], and SLAC [46–51,105–108]. CERN and SLAC provide the higher Q^2 coverage, with extensive contributions to the moments from the low-x region. JLab data cover the lowest Q^2 domain. All accelerators provide data points in the intermediate Q^2 region of a few GeV or less, including the COMPASS experiment [39–41,87–89] for CERN, E143 [46,47,105–107] for SLAC, and HERMES for DESY [42,90,91].

3. *Forward spin polarizability $\bar{\gamma}_0$*

The interaction of a particle with an electromagnetic field, in our case the reaction of the target particle to the photons exchanged with the electron beam, is dictated at first order in the photon energy by the particle electric charge. If the beam and target are polarized, then the target particle's anomalous magnetic moment also comes into play. Both the electric charge and the magnetic moment reflect the pure elastic reaction expected from a pointlike or perfectly rigid object.

At second order, the particle compositeness and deformability must be considered. The deformation of the particle, viz. its internal rearrangement under the electromagnetic field, are described by its electromagnetic polarizabilities [109]. The forward spin polarizability $\bar{\gamma}_0$ arises for the case when the beam and target are polarized longitudinally to the beam direction. Polarizabilities were initially defined for real photons but, just like the GDH sum, they can be generalized to finite Q^2, becoming Q^2-dependent *generalized polarizabilities*.

There is no practical method known that allows us to directly measure generalized polarizabilities. Instead, sum rules are used to access them. For $\bar{\gamma}_0(Q^2)$, the relevant sum rule involves a higher moment of g_1 and g_2 [110–112]:

$$\bar{\gamma}_0(Q^2) = \frac{16\alpha M^2}{Q^6}\int_0^{1^-} x^2[g_1 - \gamma^2 g_2]dx, \tag{34}$$

which can also be calculated in χEFT [60,61,79–85]. Equivalently, we can write this integral as

$$\bar{\gamma}_0(Q^2) = \frac{16\alpha M^2}{Q^6}\int_0^{1^-} x^2A_1F_1dx. \tag{35}$$

Measurement of $\bar{\gamma}_0$ has been carried out for the proton at the real photon point at MAMI [69]. Measurements at small and intermediate Q^2 have been carried out at JLab on the proton [22,98,102] and neutron [19,98,103,104]. A short review of the experimental data and predictions from χEFT, MAID [113], and SAID [114] models can be found in Ref. [74].

E. Deuteron nuclear model

As discussed above, the GDH sum rule holds for any target with arbitrary spin, once we replace the expressions $\sigma_{3/2}$ and $\sigma_{1/2}$ with the cross sections for target and photon spins aligned versus antialigned.

At the same time, experimental information on free neutrons is not realistically accessible, necessitating measurements on (neutrons bound in) nuclei to access the various structure functions and integrals defined above. For the EG4 experiment, we used the deuteron as a source of information on (bound) neutrons. In the most naïve model, the rather loosely bound deuteron can be thought of as a combination of one neutron and one proton, allowing us in principle to extract neutron structure functions after subtracting the contribution from the proton. In reality, this interpretation is complicated by various nuclear binding effects, including the Fermi motion of both bound nucleons, the depolarization of both nucleons through the D-state admixture in the deuteron ground state wave function, and potential off-shell corrections to the (virtual-) photon-nucleon interaction. In addition, the measured cross section (differences) also contain contributions not present for single free nucleons, including two-body currents, final state interactions and coherent production as well as the two-body breakup of the deuteron, $d(e, e'pn)$.

Ideally, a rigorous test of theoretical models like χEFT would compare observables measured on the deuteron with calculations taking into account all of the above effects. In practice, such calculations do not (yet) exist, and experimentally, covering the entire kinematic range from two-body breakup (2.2 MeV for real photons) to the limit of large $W >$ 2 GeV is also extremely challenging. For example, the GDH sum rule on the deuteron predicts a very small value for the integral of Eq. (27) because the anomalous magnetic moment of the deuteron is much smaller than that of the proton or neutron (0.14 versus 1.8–1.9). This is due to a very strong cancellation between the contribution from the two-body (pn) breakup of the deuteron, dominated by low photon energy of order a few MeV, and the incoherent sum from inelastic channels on both nucleons (e.g., π production with a threshold of over 140 MeV).

In lieu of a full theoretical description of the scattering process on the deuteron, we use an approximation to express structure functions of the deuteron as a sum of structure functions of the proton and the neutron, convoluted with their momentum and spin distribution inside the deuteron. Here we follow the prescription of Ref. [115]. Our approach corrects for the effects of Fermi motion and the effective nucleon polarization due to the deuteron D-state contribution. At the same time, experimentally, we avoid the kinematic region where coherent and two-body breakup effects are expected to be most significant, i.e., low-energy transfer. For this reason, we extract neutron (and deuteron) structure function results only in the region $W > 1.15$ GeV from our data, corresponding to virtual photon energies in excess of 240 MeV even at our lowest Q^2 point. This also minimizes the contribution from quasielastic scattering and its radiative tail to our data, so that we should be dominated by the sum of contributions from the two individual nucleons. Since our lowest Q^2 bin, with a mean value of 0.017 GeV^2, corresponds to a resolution of $\hbar/\sqrt{Q^2} = 1.5$ fm, we can also assume that these contributions largely add incoherently, given the root-mean-square (RMS) separation of the two nucleons in deuterium of nearly 4 fm. The region 1.073 GeV $< W <$ 1.15 GeV, when needed, can be augmented by a parametrization of single-pion production off protons and neutrons from the MAID partial wave analysis [113], where multiparticle final states do not contribute and the MAID parametrization is very reliable.

For moments of spin structure functions, the most conspicuous nuclear effect, viz. smearing of the resonances by Fermi motion, is integrated out. It vanishes exactly for first moments and to a good approximation for higher moments. We studied this assertion using a model for both smeared and unsmeared spin structure functions and found no difference in the first moments, and only minute differences in the higher moments ($\overline{\gamma}_0$) (up to 4.8%, which is small compared to our statistical and systematic uncertainties). Thus, no corrections were applied to the data; we only account for the effective polarization of the nucleons in deuterium when relating integrals for protons, neutrons, and deuterons, while supplementing the region 1.073 GeV $< W <$ 1.15 GeV with the MAID parametrization:

$$\overline{\Gamma}_1^d = (\overline{\Gamma}_1^p + \overline{\Gamma}_1^n)(1 - 1.5\omega_D), \tag{36}$$

$$\overline{I}_{\mathrm{TT}}^d = (\overline{I}_{\mathrm{TT}}^p + \overline{I}_{\mathrm{TT}}^n)(1 - 1.5\omega_D), \tag{37}$$

$$\overline{\gamma}_0^d = (\overline{\gamma}_0^p + \overline{\gamma}_0^n)(1 - 1.5\omega_D), \tag{38}$$

with $\omega_D = 0.056 \pm 0.01$ [116–120] accounting for the nucleon depolarization caused by the deuteron D-state.

III. EG4 EXPERIMENT

The CLAS EG4 experiment [121,122] was carried out at JLab's experimental Hall B in 2006. Data in the range $0.9 \lessapprox W \lessapprox 2.2$ GeV were collected using six beam energies and on longitudinally polarized NH$_3$ and ND$_3$ targets. Since the physics goal of EG4 was focused on the χEFT domain, data were collected with high statistics at very low Q^2 values, which enabled us to form moments down to 0.012 GeV^2 for the NH$_3$ target. As a comparison, the previous CLAS spin structure experiment EG1b [102] measured down to $Q^2 =$ 0.05 GeV^2. Therefore, the data below $Q^2 = 0.1$ GeV^2 were improved significantly from this experiment.

Figure 2 shows the EG4 kinematic coverage for polarized NH$_3$ and ND$_3$ targets. The beam energies used during the experiment were 1.054, 1.338, 1.989, 2.260, and 2.999 GeV. For the ND$_3$ target, only two beam energies 1.34 and 1.99 GeV were used. The beam polarization was on average 85% throughout the experiment, as measured by the Hall B Möller polarimeter. The ranges in the target polarization were (75–90)% and (30–45)% for NH$_3$ and ND$_3$, respectively, measured by the NMR polarimetry.

A. Polarized electron beam and beam monitoring

For each of the three experimental halls during the JLab 6 GeV era, a 499 MHz beam was generated with the desired beam current and polarization at the source. They were then intercalated to form a 1497 MHz beam and accelerated to about 45 MeV by superconducting radio-frequency (SRF) cavities. The beam was then injected into the two 0.4 km LINACs consisting of 20 SRF cavities each. The two LINACs are connected by recirculation arcs, forming a racetrack-shaped accelerator. Each revolution increased the beam energy by up to 1.2 GeV, determined by the settings of the SRF cavities. The beam could be circulated up to 5 times before being separated and dispatched to the three halls.

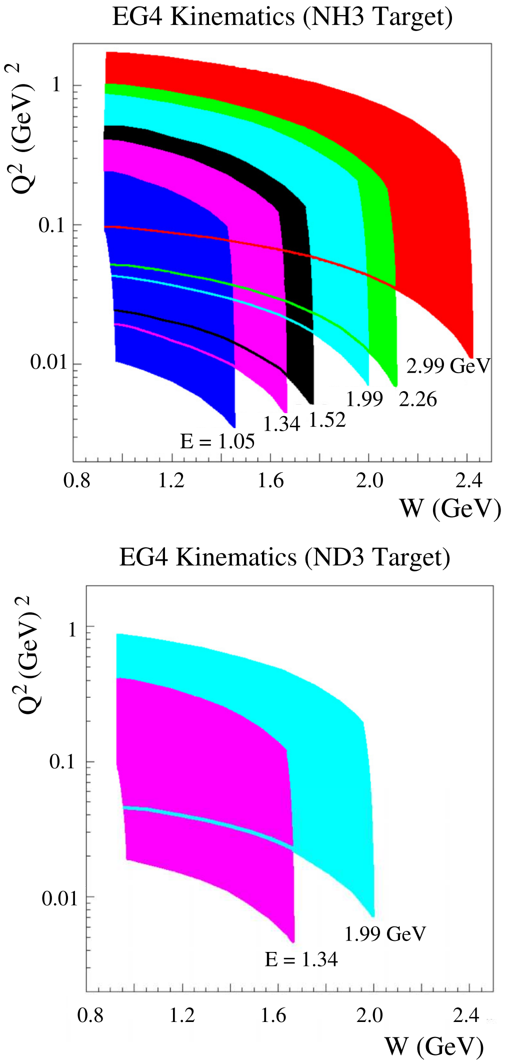

FIG. 2. EG4 kinematic coverage (Q^2 vs W) for the NH_3 (top) and ND_3 (bottom) targets.

The EG4 experiment employed beams circulated between 1 and 3 times, with the beam current ranging from 1 to 3.5 nA. The Hall B beamline is instrumented to measure and monitor the beam properties, namely, position, transverse distribution (beam profile), current, polarization, and charge asymmetry [20].

Nine RF cavities grouped in three beam position monitor (BPM) sets, located 36.0, 24.6, and 8.2 m upstream from the CLAS center, measured both the beam position and current. The latter was also monitored by synchrotron light monitors (SLM) and measured absolutely by a Faraday cup positioned at the end of the beamline, 29.0 m downstream from the CLAS center. The Faraday cup consisted of a 15 cm diameter Pb cylinder of 75 radiation lengths thickness and measured the accumulated charge. Time-derivation of the accumulated charge provided the beam current.

The beam profile was periodically verified by running thin wires ("harps") through the beam and detecting scattered electrons using photomultipliers (PMTs) located 10 cm from the beamline. The harps also served to calibrate the BPMs.

The EG4 experiment used a longitudinally polarized beam. The beam helicity was flipped at 30 Hz, taking the quartet structure of either $+--+$ or $-++-$, with the first helicity window selected from a pseudorandom sequence. The beam polarization was regularly measured by a Möller polarimeter set at the entrance of the Hall. It consisted of detectors, transport and polarizing magnets, and a 25 μm thick Permendur foil (49% Fe, 49% Co, 2% Va) acting as a polarized electron target and oriented at $\pm 20^\circ$ with respect to the beamline. A pair of 120 G Helmholtz coils thermally polarized the foil longitudinally to 7.5%. For each beam polarization measurement, the foil was inserted in the beam for about 30 minutes. The scattered (recoil) electrons were transported to the detectors (two lead-glass blocks) by two quadrupoles. The Möller asymmetry was measured by detecting the two electrons in coincidence and compared to the well-known theoretical expectation to obtain the beam polarization. A 30 min measurement provided a $\approx 1\%$ statistical precision. The beam polarization for EG4 was typically around 86% [23], determined with a $\approx 2.5\%$ systematic uncertainty. Two of the Möller measurements were cross-checked with a Mott polarimeter set in the CEBAF injector that measured the polarization of 5 MeV electrons [123]. These direct measurements were used to check the stability of the beam polarization, while for the data analysis the product of beam and target polarization $P_b P_t$ was directly determined in *ep* elastic or *ed* quasielastic scattering, see Secs. V A and V D.

The beam charge asymmetry, viz. the relative difference in the number of electrons per helicity bunch, was monitored by the BPMs, SLM, and Faraday cup and minimized by feedback to the electron polarized source. Most individual runs had beam charge asymmetry lower than 10^{-3}, with a maximum of several 10^{-3} for some runs.

The Hall B beamline was not equipped with a beam energy measurement device. Instead, the beam energy was calculated from the setting of the CEBAF magnets together with the beam position [124]. The relative accuracy reached on the beam energy measurement was a few 10^{-4}.

In addition to its instrumentation, the Hall B beamline had two pairs of magnetic coils to raster the beam over the target. This was to spread the heat uniformly over the target to avoid depolarization, see next section. The raster used a spiral pattern of 1.2 cm outer diameter.

B. Polarized targets

During EG4 the polarized target was placed 1.01 m upstream from the CLAS center to increase the acceptance at low Q^2 by reducing the minimum angle for scattered electrons.

The targets included frozen $^{15}NH_3$ and $^{15}ND_3$ dynamically polarized at 1 K with a 5 T field, as well as two carbon targets and an empty cell for reference. These were the same as the targets used for previous CLAS double-polarization measurements [125]. The beam was rastered to protect the target from overheating and to minimize depolarization. The target density was 0.917 and 1.056 g/cm^3 for NH_3 and ND_3, respectively.

The structure of the target insert for EG4 is shown in Fig. 3. The target cells were either 1.0 cm or 0.5 cm in length, for

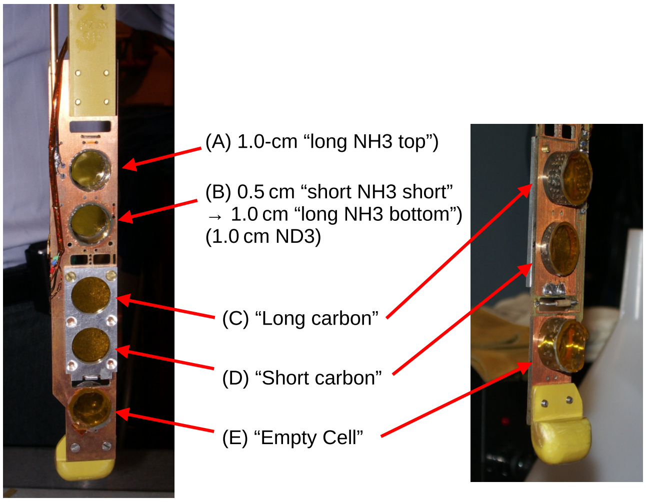

FIG. 3. Target insert used during the EG4 experiment, viewed from the front (left) and back (right). The five target positions are labeled A, B, C, D, and E, as shown, that accommodated polarized cells, and two carbon targets and an empty cell for calibration purposes. Two NH_3 cells, of lengths 1.0 and 0.5 cm, were installed in positions (A) and (B) during the first half of the NH_3 run period, and were called the “long NH_3 top” and the “short NH_3” targets, respectively. During the second half of the NH_3 run, two 1.0 cm NH_3 targets were installed in positions (A) and (B), and were called the “long NH_3 top” and the “long NH_3 bottom” targets, respectively. For the ND_3 run period only a single 1.0 cm ND_3 target was installed in position (B).

systematic studies, and were referred to as the long and short targets, respectively. The insert was placed into the target “banjo,” an approximately 1 liter vessel of 1 K liquid helium at the center of a 5 T superconducting split coil magnet. A complete description of the polarized target can be found in Ref. [126].

C. CLAS spectrometer and the Cherenkov detector

The basic structure of CLAS is shown in Fig. 4. The design of the CLAS detector was based on a toroidal magnetic field that was generated by six superconducting coils arranged around the beamline. In the EG4 experiment, the torus field setting was to bend electrons away from the beamline (outbending configuration). The magnet coils naturally separated the detector into six “sectors”, each functioning as an independent magnetic spectrometer. Each sector included four sub-detectors: drift chambers (DC), Cherenkov counters (CC), time-of-flight scintillator counters (SC), and electromagnetic calorimeters (EC). The drift chambers were located before, within, and after the torus magnetic field and performed charged particle tracking, allowing for the determination of the particle momentum from the curvature of their trajectories. The other sub-detectors were located outside the magnetic field region. To cover the very low Q^2 region with the high detector efficiency necessary for the absolute cross section measurements, a new CC was built by the INFN-Genova group and was installed in Sector 6. The main elements of this detector are shown in Fig. 5. Basic information on the new CC can be found in Ref. [23].

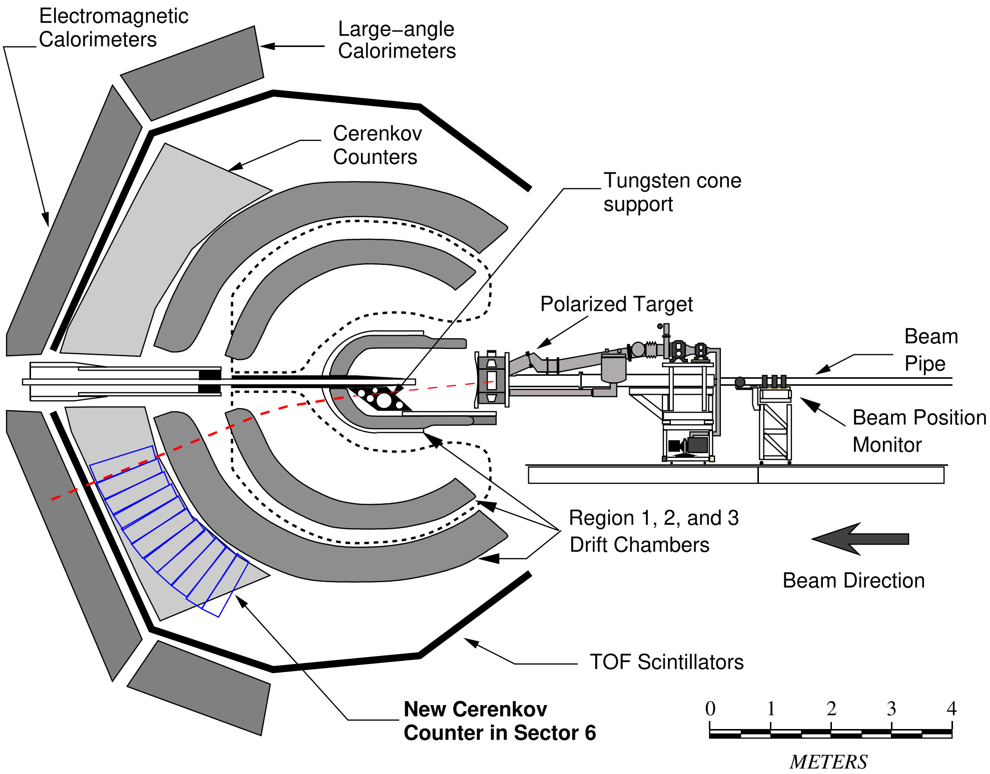

FIG. 4. Side view of CLAS with the outline of the new Cherenkov detector’s segments shown in blue. A typical electron trajectory for the electron outbending setting is shown as the (red) dashed line.

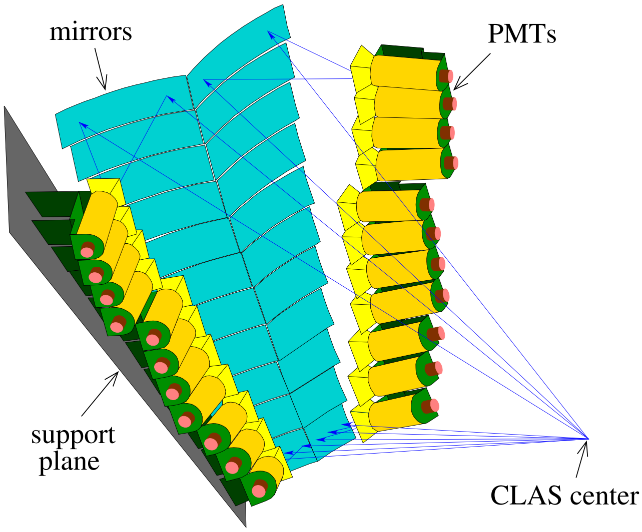

FIG. 5. The new Cherenkov detector used by the EG4 experiment. This detector consists 11 pairs of spherical mirrors that reflect the Cherenkov light to corresponding photomultiplier tubes (PMTs).

Another special feature adopted by EG4 was a new tungsten cone for the Möller shield, shown in Fig. 4, which allowed direct line-of-sight from the target at smaller scattering angles down to 5°.

D. Trigger and data acquisition system

The main electron trigger for EG4 was formed using a coincidence between the signals from the EC and the new CC; consequently only 1/6 of the full azimuthal acceptance of CLAS was used. For calibration of the new CC performance, data were also taken using EC-only triggers.

All photomultiplier-tube (PMT) time-to-digital-converter (TDC) and analog-to-digital-converter (ADC) signals (i.e., SC, EC, and CC signals) generated within 90 ns of the trigger were recorded, along with DC TDC signals [11]. A trigger supervisor (TS) directed all the signals to the data acquisition system.

The offline physics event reconstruction code used geometric parameters and calibration constants to convert the TDC and ADC data into kinematic and particle identification data. The code cycled through particles in the event to search for a single trigger electron—a negatively charged particle that produced a shower in the EC. If more than one candidate was found, then the one with the highest momentum was selected. This particle was traced along its geometric path back to its intersection in the target to determine the path length, which, with the assumption that its velocity $v = c$, determined the event start time. From this start time, the TOF of other particles could then be determined from the SC TDC values. The TDC values from the EC were used when SC values were not available for a given particle.

IV. DATA ANALYSIS

The analysis presented in this section lead to the extraction of both the proton and the deuteron spin structure functions g_1, A_1F_1, and their moments, previously reported in Refs. [21,22]. We will present the general method (Sec. IV A), event selection criteria and kinematic corrections (Sec. IV B), particle identification performance and efficiency analysis of the new CC (Sec. IV C), and background (Sec. IV D).

A. Overview of the analysis methods

In this work, we first extracted the event yield difference between the positive and negative beam helicity states. The polarized cross section differences, Eq. (7), were extracted from the yield differences as follows:

$$\Delta\sigma_{||}(\Delta W, \Delta Q^2) = \int_{\Delta W \Delta Q^2} \left(\frac{d^2\sigma_{\uparrow\Uparrow}}{d\Omega dE'} - \frac{d^2\sigma_{\uparrow\Downarrow}}{d\Omega dE'}\right) dE' d\Omega$$
$$= \left[\frac{N^+}{N_e^+} - \frac{N^-}{N_e^-}\right] \frac{1}{N_{\text{targ}}} \frac{1}{P_b P_t} \frac{1}{\eta_{\text{detector}}}, \quad (39)$$

where $N_e^{\pm}$ is the number of incident electrons with helicity ±, respectively, as recorded by the Faraday cup or beam charge monitors; $N^{\pm}$ is the number of scattered electrons with incident helicity ±, within the bin $\Delta W \Delta Q^2$, that pass through all analysis cuts; N_{targ} is the number of polarized target nucleons per cm^2; $P_b P_t$ is the product of the beam and the target polarizations; and finally, η_{detector} is the product of the acceptance and efficiency of the detector and the trigger.

In practice, we calculated the yield difference in each (W, Q^2) bin and compared to the simulated value that accounts for efficiency and acceptance, and with the same acceptance and fiducial cuts as data.

One important advantage of our method is that contributions from unpolarized material cancel in the yield differences. This is important for experiments utilizing polarized NH$_3$ and ND$_3$ targets because of the presence of significant amounts of unpolarized material, including target windows, support, insulation, liquid helium for cooling, and the nitrogen in the ammonia beads (the nitrogen can be slightly polarized and is treated as a background contribution). The remaining unknowns on the RHS of Eq. (39), $P_b P_t N_{\text{targ}}$, were obtained indirectly by normalizing the yield differences of elastic scattering of the data to simulation, which provided more accurate information than combining beam and target polarimetry data (P_b, P_t) along with information on the polarized material thickness of the target.

After event selection and kinematic correction (see next two sections), the data were divided into the Q^2 bins shown in Table I, with bin limits determined logarithmically (the upper edge of each bin Q^2_{max} is $10^{1/13}$ of the lower edge Q^2_{min}). In practice, proton data exist for all 25 Q^2 bins, and deuteron data from bin 3 to 24. Our neutron results (as presented in Sec. VI B) were extracted from combining proton with deuteron data, and thus also exist from bins 3 to 24 only.

B. Event selection and kinematic corrections

The primary signal of this analysis was the scattered electrons in the inclusive mode. Multiple selection criteria were used to select good electron events, requiring the correct particle charge ($-|e|$) and valid detector signals in DC, SC, EC,

TABLE I. Q^2 bins used for the EG4 inclusive channel analysis. For each bin, both minimum and maximum (lower and upper edge) are shown, with the mean Q^2 value calculated as $Q^2_{\mathrm{mean}} = \sqrt{Q^2_{\mathrm{min}} Q^2_{\mathrm{max}}}$. Note that identical binning was used in the analysis of the earlier CLAS EG1b data [102].

Q^2 bin ID	1	2	3	4	5
min $(\mathrm{GeV}/c)^2$	0.0110	0.0131	0.0156	0.0187	0.0223
mean $(\mathrm{GeV}/c)^2$	0.0120	0.0143	0.0171	0.0204	0.0244
max $(\mathrm{GeV}/c)^2$	0.0131	0.0156	0.0187	0.0223	0.0266
Q^2 bin ID	6	7	8	9	10
min $(\mathrm{GeV}/c)^2$	0.0266	0.0317	0.0379	0.0452	0.0540
mean $(\mathrm{GeV}/c)^2$	0.0290	0.0347	0.0414	0.0494	0.0590
max $(\mathrm{GeV}/c)^2$	0.0317	0.0379	0.0452	0.0540	0.0645
Q^2 bin ID	11	12	13	14	15
min $(\mathrm{GeV}/c)^2$	0.0645	0.0770	0.0919	0.110	0.131
mean $(\mathrm{GeV}/c)^2$	0.0705	0.0841	0.1005	0.1200	0.143
max $(\mathrm{GeV}/c)^2$	0.0770	0.0919	0.110	0.131	0.156
Q^2 bin ID	16	17	18	19	20
min $(\mathrm{GeV}/c)^2$	0.156	0.187	0.223	0.266	0.317
mean $(\mathrm{GeV}/c)^2$	0.171	0.204	0.244	0.290	0.347
max $(\mathrm{GeV}/c)^2$	0.187	0.223	0.266	0.317	0.379
Q^2 bin ID	21	22	23	24	25
min $(\mathrm{GeV}/c)^2$	0.379	0.452	0.540	0.645	0.770
mean $(\mathrm{GeV}/c)^2$	0.414	0.494	0.590	0.705	0.841
max $(\mathrm{GeV}/c)^2$	0.452	0.540	0.645	0.770	0.919

and CC. The quality of the helicity signal recorded in the data stream was examined closely and any quartet sequence with inconsistency was rejected. Kinematic corrections were then applied to each event that consisted of: incoming energy loss correction, raster correction, tracking correction, momentum correction, and outgoing ionization loss correction. These corrections were checked by the position of the W peak of ep elastic scattering, which is required to coincide with the proton mass perfectly.

After kinematic corrections, more selection criteria were applied. First, events must be detected in sector 6 of CLAS. The particle momentum must be between 20% and 100% of the incoming beam energy, and must be higher than 0.37 GeV, corresponding to the trigger threshold set for the experiment. The distribution of the z position along the beamline of the electron vertex was then studied for different Q^2 bins and fitted using a Gaussian function. Only events within three standard deviation ($\pm 3\sigma_z$) of the average z position of that bin were accepted, except for those few bins where the z distribution was rather wide and a tighter cut was used; see Fig. 6. These vertex z cuts ensured that data statistics were maximized while reducing backgrounds from the beamline, and that events scattered from the insulation layers of the target were rejected.

A series of cuts were then applied on the event's momentum p versus polar angle θ as well as θ versus the azimuthal angle ϕ to avoid the fiducial regions where the detector efficiencies were low.

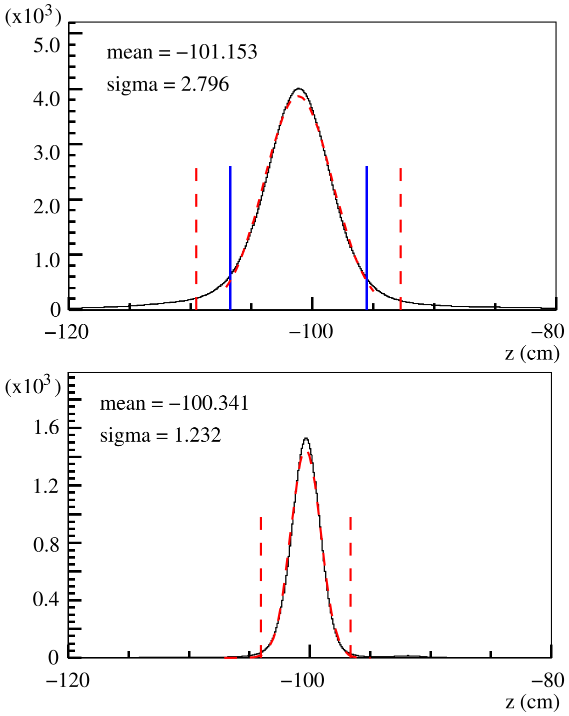

FIG. 6. Vertex z distribution (solid black curves) of the 1.1 GeV NH_3 target data for $Q^2 = (0.011, 0.0131)$ GeV^2 (top) and $Q^2 = (0.0452, 0.054)$ GeV^2 (bottom) bins. The dashed (red) curves show the Gaussian fit with the fitted mean and sigma values (in cm) shown in each panel. The two dashed (red) vertical lines show the $3\sigma_z$ widths. A $3\sigma_z$ cut is used for the bottom figure, while a $2\sigma_z$ (solid blue vertical lines) is used for the top. When making these plots, all good electron cuts except the vertex z cut were applied.

C. Particle identification and Cherenkov efficiency

Particle identification cuts were applied on the EC and CC signals. For the EC, the ratio of the total energy deposited over the particle momentum E_{tot}/p within each Q^2 bin was fit with a Gaussian peak and cuts were applied to select events within 3σ from the peak center. Furthermore, the energy deposited in the inner layer of the EC, E_{in}, was required to be greater than 0.06 GeV. The same 3σ and E_{in} cuts were also applied to the simulation such that a direct comparison with data could be made to account for the efficiency of these PID selection criteria.

Further PID cuts were applied to the number of photoelectrons in the CC signal, requiring $n_{\mathrm{p.e.}} > 2.0$ for NH_3 and $n_{\mathrm{p.e.}} > 2.5$ for ND_3 analysis. The CC signals must also pass conditions that match their timing and geometrical location with those of the EC and DC [127]. Unlike the EC, the CC efficiency due to these PID selection criteria could not be easily obtained from detector simulation, and had to be extracted from data and applied to the simulation. We discuss below the details of the CC efficiency study.

The event distribution in the hit position of the CC, in terms of θ_{vtx}, the polar angle at the interaction point, and ϕ_{DC1}, the azimuthal angle in the first layer of the DC, was studied to determine both $n_{\mathrm{p.e.}}$ yield and the high efficiency region of the new CC. Both the event distribution and the $n_{\mathrm{p.e.}}$ depend

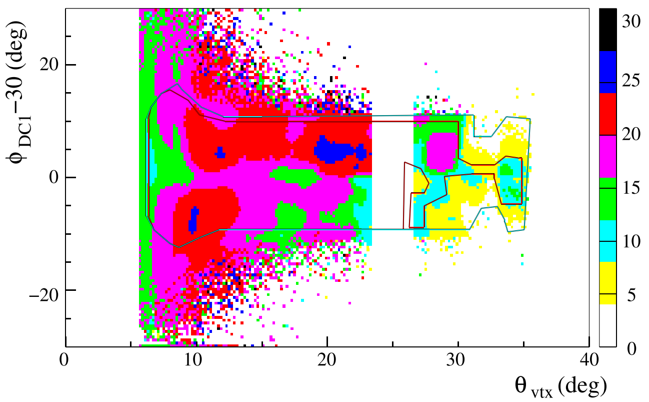

FIG. 7. Fiducial cuts applied to $\phi_{\rm DC1}$ (offset by -30°) vs $\theta_{\rm vtx}(^\circ)$ for the $I_{\rm torus}/2250{\rm A}/p({\rm GeV}) = (0.6, 0.7)$ bin for 2.3 GeV data taken on NH$_3$. The color depth shows the average $n_{\rm p.e.}$ values for each $(\theta_{\rm vtx}, \phi_{\rm DC1})$ bin. When making these plots, all good electron cuts except the $\phi_{\rm DC1}$ vs $\theta_{\rm vtx}$ fiducial cut were applied. The outer contour shows the first-round of fiducial region that traced the region of low event yield. The inner contour, which is the final CC fiducial cut, also rejects regions of low $n_{\rm p.e.}$ values. The blank region near $\theta = 25^\circ$ is due to a low-efficiency region in the DC and is rejected from the analysis and the simulation.

on the event hit position in the CC, and thus vary with the ratio of the CLAS torus current over particle momentum $I_{\rm torus}/p$, where $I_{\rm torus} = 2250$ A for beam energies 2.0, 2.3, and 3.0 GeV and 1500 A for beam energies 1.1 and 1.3 GeV. Figure 7 shows the $n_{\rm p.e.}$ distribution for one representative $I_{\rm torus}/p$ bin, for the 2.3 GeV data collected on NH$_3$.

For a specific $I_{\rm torus}/p$ bin, the CC efficiency for a given $(\theta_{\rm vtx}, \phi_{\rm DC1})$ bin was determined by taking calibration data that utilized EC alone for electron identification. For each bin, we denote the number of electrons recorded in EC-only calibration data to be N_1 and among those events, N_2 electrons also pass the CC selection criteria. The efficiency, and its uncertainty for $N_1 \neq N_2 \neq 0$ case, were calculated as

$$\eta = \frac{N_2}{N_1}, \quad \Delta\eta_{N_2\neq N_1} = \sqrt{\frac{N_2(1-N_2/N_1)}{N_1}}. \tag{40}$$

For the case of $N_2 = N_1$ or if $N_2 = 0$, we must consider the uncertainty due to N_2 being an integer (that is, we cannot detect half of an electron!). If $N_2 = N_1$, then we assign

$$\eta_{N_2=N_1} = \frac{N_2 - 0.25}{N_1}, \quad \Delta\eta_{N_2=N_1} = \frac{0.25}{N_1}. \tag{41}$$

If $N_2 = 0$, then we assign

$$\eta_{N_2=0} = \frac{0.25}{N_1}, \quad \Delta\eta_{N_2=0} = \frac{0.25}{N_1}. \tag{42}$$

Note that the uncertainty due to N_2 being integer also exists for the general case, but was completely negligible compared with Eq. (40) for N_1 as small as 2.

Once we extracted the CC efficiency and its uncertainty map for given $I_{\rm torus}/p$ range and $(\theta_{\rm vtx}, \phi_{\rm DC1})$ bin, we matched it to the $n_{\rm p.e.}$ map for the same bin. Then we fit the values of the efficiency as a function of $n_{\rm p.e.}$ using the Poisson function form, see Fig. 8 top panel. We studied the efficiency fit for both individual $I_{\rm torus}/p$ bins as well as all bins combined. (When combining bins, we combined N_1 and N_2 first and then evaluated the efficiency and its uncertainty.) We found the fit to achieve good results for all cases, and the fit results for individual $I_{\rm torus}/p$ bins were consistent with those achieved by combining all bins, see Fig. 8 bottom panel. These results were used in the simulation to account for the CC efficiency, see Sec. V.

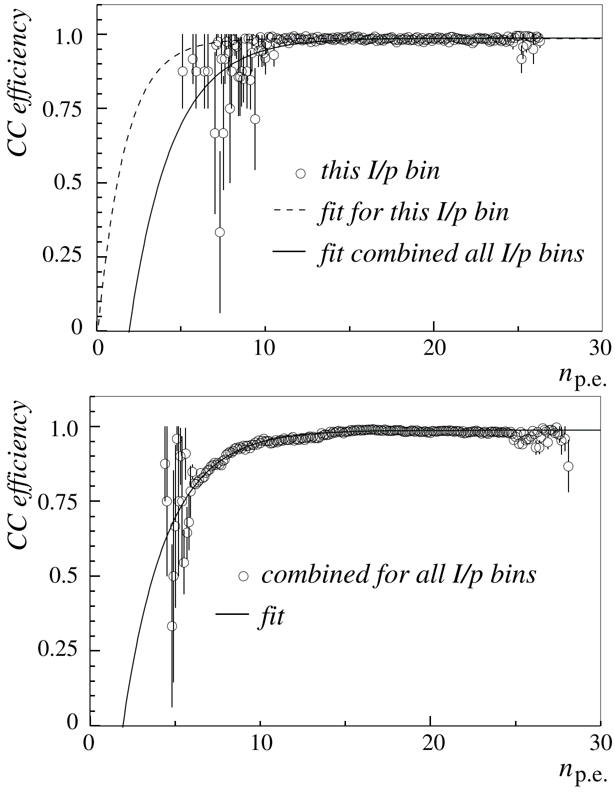

FIG. 8. CC efficiency (open circles) vs the number of photoelectrons $n_{\rm p.e.}$ for the $I_{\rm torus}/2250{\rm A}/p$ (GeV) = (0.6, 0.7) bin (top) and for all $I_{\rm torus}/p$ bins combined (bottom) for 2.3 GeV data taken on the NH$_3$ top long cell. The efficiencies and error bars were evaluated using Eqs. (40)–(42). The fit results for the $I_{\rm torus}/2250{\rm A}/p({\rm GeV}) = (0.6, 0.7)$ bin is $\eta_{cc} = 0.986 - e^{-0.062(x-0.44)}$ (dashed curve), and for the combined results is $\eta_{cc} = 0.987 - e^{-0.040(x-18.8)}$ (solid curve). When making these plots, all good electron cuts were applied, thus there is no entry below $n_{\rm p.e.} = 2$ by definition. Note that even after combining all bins, the region with $n_{\rm p.e.} \leqslant 6$ has low statistics and relatively large uncertainties.

D. Background contamination

For inelastic scattering processes, charged pions can be misidentified as electrons. Similarly, neutral pion decay can produce photons and subsequently electrons via the pair production process. Contamination from these two background processes were studied using charged pion yields, and positron yields taken with the in-bending torus configuration. The pion contamination was found to be less than 1%, and pair production yield was on the order of 10^{-3} for all kinematics. We did not correct these backgrounds, but instead incorporated them into the systematic uncertainties. An additional background is the electron scattering off the ^{15}N in the target. The ^{15}N is slightly polarized, and thus we discuss this background along with its correction in Sec. V H as part of the systematic uncertainties.

V. SIMULATION AND EXTRACTION OF PHYSICS RESULTS

As described in the previous section, this analysis was based on extraction of polarized yield differences $[\frac{N^+}{N_e^+} - \frac{N^-}{N_e^-}]$ from data. This was done for all Q^2 and W ranges covered by the experiment, including both elastic and inelastic scattering. By comparing ("normalizing") the yield difference from simulation and data in the region of the elastic (proton) or quasielastic (deuteron) peak, factors such as beam and target polarizations, luminosity, average trigger efficiency and detector efficiencies of Eq. (39) were accounted for and did not need to be treated or corrected separately. Then, the same normalization was applied to the yield difference from simulation of inelastic scattering. By comparing these differences to the measured spectra, the structure functions g_1 and A_1F_1 can be extracted. In this section we describe the simulation procedure and the extraction of the structure functions.

A. Simulation of (quasi)elastic polarized yield differences

A simulation for *ep* elastic and *ed* quasielastic scattering events was performed using GSIM [128,129], the standard CLAS simulation program, combined with an event generator for (quasi)elastic scattering. Events were generated for ranges of $\theta = (5^\circ, 45^\circ)$ and $\phi = (250^\circ, 325^\circ)$. The θ and ϕ ranges ensured the whole Sector 6 was covered, while keeping a reasonable generator efficiency.

Two functions were used to generate separately the proton elastic peak and its radiative tail with appropriate relative weights. The proton form factors were from Ref. [130], and the radiative tail included both internal and external radiation effects following the prescription of Refs. [131,132]. The depolarization effect of the Bremsstrahlung photons was calculated following Ref. [133].

For the quasielastic events, we used a convolution prescription [115] to calculate the inclusive structure function of the deuteron stemming only from scattering elastically off a moving proton or neutron. Radiative effects were included using the code RCSLACPOL [102], which was based on the treatments of Refs. [131,134]. For the proton contribution, we used the same form factors as for elastic *ep* scattering; for the neutron form factors, we used a continued fraction parametrization [135] for G_M^n and the two-parameter Galster fit [136] for G_E^n.

The simulated data were then passed through the GSIM post processor (GPP) [128] to account for smearing factors in the detectors, and RECSIS [137], the standard CLAS simulation program for event reconstruction. Detailed inputs to the simulation, GPP, and corrections applied in the reconstruction are given below.

TABLE II. Fitting results for the wire-dependent smearing factor used in simulation of the NH$_3$ target. The functional form of Eq. (43) was used for the fit. All three layers of DC used the same smearing factor.

E_b (GeV)	p_0	p_1	p_2
1.1	1.952 ± 0.007	24.13 ± 0.12	14.18 ± 0.04
1.3	1.349 ± 0.014	24.22 ± 0.35	14.47 ± 0.14
2.0	1.837 ± 0.030	15.22 ± 0.37	9.48 ± 0.14
2.23	2.198 ± 0.021	11.07 ± 0.18	7.90 ± 0.06
3.0	2.161 ± 0.040	10.67 ± 0.30	6.70 ± 0.11

B. Energy loss correction

The beam energy measured in the experiment (Sec. III A) was used in the simulations. The quality of the simulation was evaluated by comparing the reconstructed W spectra of the elastic peak to data in all Q^2 bins. Special attention was paid to the position and the width of the elastic peak because both can affect the normalization. Because kinematic corrections were applied to the data, the elastic peak position extracted from data was very close to the proton mass (within ∼1–2 MeV). However, the elastic peak position extracted from the reconstructed simulated events was shifted from the proton mass by several MeV due to energy loss of scattering electrons in the simulation that were not corrected completely in the reconstruction. To correct for this effect, we calculated the correction $E_{\rm corr}$ that should be added to E' to align the W value of the reconstructed simulated elastic peak to the proton mass. A linear dependence on E' was observed when combining simulation of all five beam energies: $E_{\rm corr}(\text{MeV}) \times \cos\theta = 1.812 + 1.399E'$ with E' in GeV, and the $\cos\theta$ factor was to account for the possible θ-dependence due to most of material being oriented perpendicular to the beamline.

C. Smearing factor for DC resolution

By comparing the W peaks of the elastic simulation with those obtained from data, it was found necessary to apply DC smearing in the GPP stage of the simulation. For the ND$_3$ analysis, a single DC smearing factor for each beam energy was used. For the NH$_3$ analysis, we found it necessary to adjust the smearing factor separately for each beam energy. This was done by adopting a wire-number dependence in the DC smearing factor of GPP. The functional form used for the DC smearing factor y is

$$y = 1.0 + \frac{p_0}{1.0 + e^{(x-p_1)/p_2}}, \tag{43}$$

where x is the DC wire number and $p_{0,1,2}$ are fit parameters, see Table II. The smearing factor starts from a value greater than 1 for low wire numbers (small scattering angle) to approximately 1.0 for high wire numbers (large scattering angle). The large smearing factor for small scattering angle was possibly due to limits in the knowledge of the magnetic field of CLAS in that region.

D. Comparison of elastic simulation with data

Figure 9 shows a representative bin for the comparison between data and simulation for elastic *ep* scattering. Data

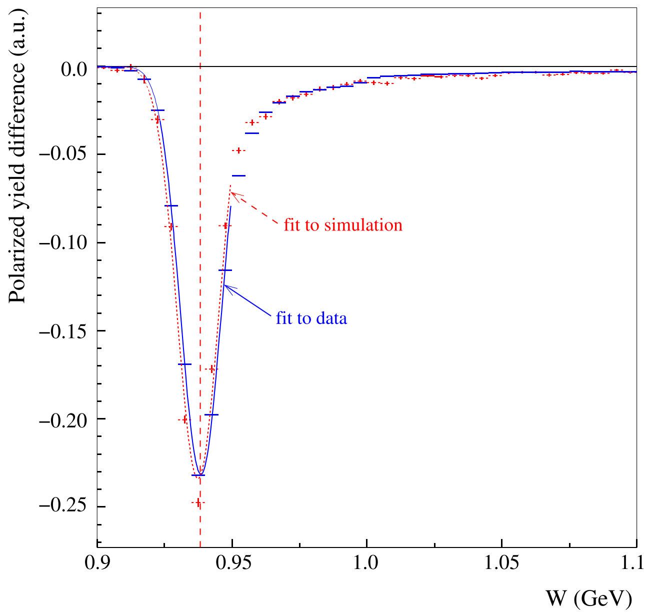

FIG. 9. Comparison of the elastic peak summed over all good Q^2 bins, simulation (red dotted) vs data (blue solid), for the 1.1 GeV data using the NH_3 bottom target cell. The vertical dashed (red) line shows the location of the proton mass. A single normalization factor was tuned until the integral under the simulated elastic peak matches that of data to within 0.2% relative. The solid (blue) and the dashed (red) curves show fits to the proton peak of the data and simulation, which find mean values of 0.9385 and 0.9374 GeV, and the peak widths (σ) of 0.0076 GeV and 0.0077 GeV, respectively. Because of the different beam polarization and target direction combinations, the sign of the elastic peak was arbitrary at this stage, but was corrected for in the extraction of the structure functions.

from low Q^2 bins were not used for normalization because of the ^{15}N elastic contamination (see Sec. V H). Both the energy loss correction and the DC smearing were applied to the simulation.

Careful studies were done for the elastic simulation quality for individual Q^2 bins. Gaussian fits were used to compare the peak location and width of simulation with data to ensure that the simulated elastic peak agrees almost perfectly with the data (and the peak position agrees with the proton mass). Bins where the simulated peak position or shape deviate from data were excluded from the normalization input. This happened only at very low Q^2 bins due to ^{15}N contamination (see Sec. V H), and at very high Q^2 bins due to sensitivity to the low-efficiency area of the DC as shown in Fig. 7. After rejecting the very low and very high Q^2 bins, we normalized the simulated elastic peak to that from data, summed over all Q^2 bins. The normalization for the deuteron data proceeded along the same lines, using the simulation of the quasielastic peak instead.

The uncertainty in the elastic peak normalization included the uncertainty in the proton form factor input [138], which was found to be less than 2% at 1.1 GeV and increased slightly for higher beam energies. The uncertainty due to radiative corrections was found to be ≈1% for all energies. In addition, we compared [130] with a recent proton form factor fit [139] that accounted for the uncertainty in the proton radius, and found the effect to be less than 1%. Overall, we estimated the uncertainty in elastic normalization to be $(1 + E_b)\%$ with E_b the beam energy in GeV. For the deuteron normalization based on the quasielastic peak, we estimated a total uncertainty of 10% for each beam energy, accounting for form factor uncertainties, the observed variation of the measured yield to simulated yield ratio with Q^2, and uncertainties in the folding and radiative correction procedure. These uncertainties were taken into account in our estimate of the systematic uncertainties (see Sec. V I).

E. Simulation of inelastic polarized yield differences

We used an event generator originally developed for Ref. [140] and improved for EG4 to generate events distributed according to the polarized cross section model from RCSLACPOL [102]. The generator worked in two steps: first, it generated separate maps for radiated inclusive polarized cross section differences

$$\Delta\sigma = \sigma_{\uparrow\Uparrow} - \sigma_{\downarrow\Uparrow}$$

for polarized electron scattering off a longitudinally polarized proton or deuteron target. The map covered the 3D space of $(E', \sin\theta, \phi)$ for ranges of $\theta = (5^\circ, 45^\circ)$, $\phi = (250^\circ, 325^\circ)$, and $E' = (0.2\,\text{GeV}, E_b)$. The θ and ϕ ranges were identical to the elastic scattering generator. Two such maps were generated for any given model of the double spin asymmetries A_1, A_2; one for positive values of $\Delta\sigma$ and one for negative values. Next, events were thrown according to the two cross section maps. The events were given vertex coordinates that were uniformly distributed over the volume of a 1 cm long cylinder with a radius of 0.01 cm around the beamline—with the center of this volume being at the EG4 target position of $z = -100.93$ cm. Equal numbers of events were generated for each map of $\Delta\sigma$. The events generated were then fed into the GSIM/GPP/RECSIS chain to create the reconstructed W, Q^2 spectra from the simulation. These spectra were normalized according to the total integrated cross section of each map. The positive and negative $\Delta\sigma$ spectra were then combined to form the full spectra for inelastic scattering. Careful studies were carried out to ensure the radiative tail of elastic scattering was subtracted from the data before they were compared with the inelastic simulation.

F. Extraction of g_1 and A_1F_1

Extraction of g_1 and A_1F_1 was done by varying the structure function model used in the inelastic simulation as follows: First, we constructed the *standard* simulation spectra using the best models for the unpolarized structure functions and asymmetries:

(i) The choice for $F_{1,2}$ and R was based on the latest fit by Bosted/Christy/Kalantarians (dated 2014), interpolating to the real photon point at very low Q^2. The most up-to-date references are [141] and [142].

For asymmetries, the latest fit performed by the EG1b collaboration [102] was used. The parametrization itself is unpublished. The asymmetry model includes three options:

(i) The asymmetries A_1 and A_2 in the resonance region are based on a combination of the deep inelastic scattering (DIS) fit with extensions into the resonance region. A parametrized fit from MAID is used to get the resonance behavior. All JLab data as of the early 2010's, as well as some MIT BATES and NIKHEF data, were used in determining the parametrization. Sum rules are obeyed as much as possible (such as the Burkhardt-Cottingham sum rule [143] and the Soffer inequality [144]).

(ii) The asymmetry A_1 in the DIS region was based on a fit to world data on inclusive spin structure functions in the DIS region (COMPASS, SLAC, HERMES, and JLab early 2010's) [33–39,46–49,51,89,98,102,103,105,106,108,145–147]. The measured $A_1(x, Q^2)$ values were fit, with simple Regge (powers of x) behavior assumed as $x \to 0$. The full uncertainty matrix of the fit was used to evaluate the systematic uncertainties.

(iii) The asymmetry A_2 in the DIS region was determined from g_2^{WW} [148]. To evaluate systematic uncertainties, we added an extra twist-3 term obtained by fitting to the SLAC E155x [149] data.

After establishing the *standard* simulation as above, we varied A_1 by an arbitrary value, +0.1 or −0.1, for all inelastic W values, and generated the difference in the polarized cross section:

$$\Delta\sigma_{\text{diff}} = \Delta\sigma_{\text{nonstd}(A_1\,\text{changed by}\,\pm 0.1)} - \Delta\sigma_{\text{std}}. \tag{44}$$

After applying the same normalization factor as the *standard* simulation, the resulting simulated event count was denoted Δn^{diff} and was added to the *standard* simulation Δn^{sim0} to form the *nonstandard* spectra Δn^{sim1}, which corresponds to the model with A_1 changed by ± 0.1:

$$\Delta n_{\text{diff}} = \Delta n_{\text{nonstd}(A_1\,\text{changed by}\,\pm 0.1)} - \Delta n_{\text{std}}. \tag{45}$$

The polarized yield obtained from data, Δn^{data}, would nominally agree with neither the *standard* Δn^{sim0} nor the *nonstandard* Δn^{sim1}, since neither model would match our data perfectly.

By comparing the polarized yield from our data (Δn^{data}) with that from the *standard* simulation (Δn^{sim0}) and the *nonstandard* simulation (Δn^{sim1}), the value for g_1 was extracted as

$$g_1^{\text{data}} = g_1^{\text{sim0}} + \left(g_1^{\text{sim1}} - g_1^{\text{sim0}}\right)\frac{\Delta n^{\text{data}} - \Delta n^{\text{sim0}}}{\Delta n^{\text{sim1}} - \Delta n^{\text{sim0}}} \tag{46}$$

$$= g_1^{\text{sim0}} + \left(g_1^{\text{sim1}} - g_1^{\text{sim0}}\right)\frac{\Delta n^{\text{data}} - \Delta n^{\text{sim0}}}{\Delta n^{\text{diff}}}, \tag{47}$$

where g_1^{sim0} and g_1^{sim1} are the g_1 values used in the *standard* and the *nonstandard* simulations, respectively. Similarly, the value for A_1F_1 was extracted as

$$\begin{aligned}(A_1F_1)^{\text{data}} &= (A_1F_1)^{\text{sim0}}\\ &\quad + [(A_1F_1)^{\text{sim1}} - (A_1F_1)^{\text{sim0}}]\frac{\Delta n^{\text{data}} - \Delta n^{\text{sim0}}}{\Delta n^{\text{diff}}}.\end{aligned} \tag{48}$$

The ratios of $\Delta n^{\text{diff}}/(g_1^{\text{sim1}} - g_1^{\text{sim0}})$ and $\Delta n^{\text{diff}}/[(A_1F_1)^{\text{sim1}} - (A_1F_1)^{\text{sim0}}]$ on the RHS of Eqs. (47) and (48) describe how the yield varies with the input g_1 or A_1F_1 of the model, and directly affect the extraction of these structure functions. These ratios were sensitive to the statistical fluctuations in Δn^{diff}, which can be large if small W bins are used. In our analysis, these ratios were smoothed out by taking a five-point average of adjacent W bins.

We emphasize that our method of extracting g_1 and A_1F_1 described above does not depend strongly on the specific models used for the Monte Carlo generator, since a larger deviation of the model from the data would simply lead to a larger "correction" in Eqs. (47) and (48), bringing the result to the same final value.

G. Systematic uncertainty due to models used in the extraction

In the extraction of g_1 or A_1F_1 described above, there can be systematic uncertainties due to the models used for $F_{1,2}$, R, A_1, and in particular, for A_2, because only longitudinally polarized targets were used in this experiment. We evaluated the model dependence as follows: a simulation corresponding to a variation of the input structure function was performed, following the same method as the *nonstandard* simulation (where A_1 is changed by ± 0.1). This variation of simulation gave Δn^{var}, with "var" for "variation in the input model." The value for g_1 with this model variation was also calculated, denoted as g_1^{var}. The systematic uncertainty in the extracted g_1 was calculated as

$$\Delta g_1^{\text{syst}} = \left[\frac{\left(g_1^{\text{sim1}} - g_1^{\text{sim0}}\right)}{\Delta n^{\text{diff}}}\right]\Delta n^{\text{var}} - \left(g_1^{\text{var}} - g_1^{\text{sim0}}\right), \tag{49}$$

and similarly for A_1F_1,

$$\begin{aligned}\Delta(A_1F_1)^{\text{syst}} &= \left[\frac{((A_1F_1)^{\text{sim1}} - (A_1F_1)^{\text{sim0}})}{\Delta n^{\text{diff}}}\right]\Delta n^{\text{var}}\\ &\quad - [(A_1F_1)^{\text{var}} - (A_1F_1)^{\text{sim0}}],\end{aligned} \tag{50}$$

where $[\frac{(g_1^{\text{sim1}} - g_1^{\text{sim0}})}{\Delta n^{\text{diff}}}]$ and $[\frac{((A_1F_1)^{\text{sim1}} - (A_1F_1)^{\text{sim0}})}{\Delta n^{\text{diff}}}]$ are the same values as those on the RHS of Eqs. (47) and (48), extracted from comparison between the standard versus the nonstandard simulations. A total of six variations was performed:

(i) Variation 1: Both F_1 and F_2 were increased by 3%;

(ii) Variation 2: R was changed by $R \to R + dR$ with dR the uncertainty of R given by Refs. [141] and [142];

(iii) Variation 3: The value of A_1 in the resonance region was changed to the fit before including the EG1b data (A_2 unchanged);

(iv) Variation 4: The value of A_2 in the resonance was changed to the fit before 2009 (A_1 unchanged);

(v) Variation 5: The value of A_1 in the DIS region was changed by the uncertainty of the DIS fit used in the the *standard* version. The full uncertainty matrix of the fit is used;

(vi) Variation 6: The value of A_2 was changed by adding an extra twist-3 term, obtained by fitting to the SLAC E155x data [149].

Note that the systematic uncertainty evaluated this way can be either positive or negative. When integrating the measured g_1 or A_1F_1 for the moments, the sign of the systematic uncertainty was retained and there can be cancellations. However, when combining these variations to form the total systematic uncertainty, the uncertainty from each variation was added in quadrature for g_1, A_1F_1, and for the moments. Also note that model uncertainties affect both the extraction of g_1 and A_1F_1 directly as well as indirectly through radiative corrections that are based on these models. Our method accounted properly for correlations between these two effects.

H. Contamination from polarized nitrogen

The ^{15}N in the target was slightly polarized, and scattering from the ^{15}N can contribute to the polarized count difference measured in the data. The ^{15}N contribution had three effects: contribution of ^{15}N nuclear elastic scattering to the proton elastic peak; contribution of radiative tail from ^{15}N nuclear elastic scattering to proton inelastic scattering; and contribution from ^{15}N inelastic scattering to proton inelastic scattering. The first affected normalization of the elastic simulation to the data, while the latter two affected the extraction of the structure functions from the inelastic polarized yield.

To account for each contribution from the ^{15}N background, one first needs to obtain the polarization of ^{15}N as follows: the ratio of ^{15}N polarization over that of the proton is about 16% [125], and there are three protons for every ^{15}N nucleus in NH$_3$. Therefore, the ^{15}N contamination to either the inelastic or elastic polarized yield can be obtained by multiplying the calculated ^{15}N unpolarized yield by the effective polarization ratio of $^{15}\mathrm{N}/p = 16\%/3 \approx 5\%$.

The contribution from ^{15}N nuclear elastic scattering was calculated using the ^{15}N form factors [150], and was found to be problematic only in the low Q^2 bins. This is because the invariant mass W for the ^{15}N nuclear elastic scattering, calculated using Eq. (3), is separated from that of the proton elastic peak ($W = M$) by

$$\Delta W = \frac{1}{2}\frac{Q^2}{M^2}\left(\frac{M}{M_{15N}} - 1\right)M < 0, \qquad (51)$$

where M_{15N} is the ^{15}N nuclear mass. Therefore in the W spectra, the separation the between ^{15}N nuclear elastic and proton elastic peaks was large enough for the two peaks to be distinguished from each other in all data except the very low Q^2 bins. The contamination from ^{15}N nuclear elastic scattering to the elastic normalization was kept below 1% by excluding elastic data below $Q^2 = 0.0379$ GeV^2 from the elastic normalization.

The contribution of radiative tails from ^{15}N nuclear elastic scattering to the inelastic polarized yield was calculated and found to be no more than 2% of the proton elastic tail itself. Similarly, the relative contribution from ^{15}N inelastic scattering to the proton inelastic polarized yield difference was found to be below 0.7%. We included both effects in the systematic uncertainty evaluation.

In the case of the deuteron, the possible corrections due to other components in the target were somewhat larger, since the deuteron polarization is typically a factor 2 smaller than that of protons. In addition to the contribution from ^{15}N, there is also the possibility of contamination from ^{14}N and ordinary hydrogen in the target. A detailed study of possible corrections from these contributions showed a maximum effect of 4.5% which we included in the systematic uncertainty budget for the deuteron results.

I. Summary of systematic uncertainties

In the following, we list all systematic uncertainties that enter our final results:

1. Statistical uncertainty from the simulation that enters Eqs. (47) and (48). This is typically negligible compared to data statistics and is not included in the total systematic uncertainty.
2. Model uncertainties, analyzed by using the model variations described in Sec. V G.
3. Systematic uncertainty due to the radiative tail from proton elastic scattering and from radiative corrections included in our Monte Carlo simulation. There are two potential contributions to this uncertainty: the models for the form factors and structure functions that enter these tails and radiative corrections, and the amount of target material traversed by the beam, which affects the *external* radiative tails. The former are “automatically” accounted for by our study of the overall systematic effect of using different structure function models, see Sec. V G, and by trying different form factor parametrizations (see Sec. V D). Note that we modified those model inputs *simultaneously* in the entire analysis chain, and retained the sign and magnitude of all variations to propagate them to the final results for the structure functions and moments, to properly account for correlations. The second uncertainty comes mostly from the uncertainty of the overall areal density of the target material, which in turn is determined by the packing fraction. The packing fraction (PF) is defined as the ratio of the actual quantity of ammonia target material contained in the target cell to the ideal quantity for a complete filling of the cell volume. While PF is not explicit in Eq. (39), it affects the total target thickness and thus the radiative effects in the simulation. To obtain the uncertainty due to PF, we reran the full simulation using a set of “alternate PF values” that differ from the nominal PF values. The data were reanalyzed using the alternate PF simulations and g_1 and A_1F_1 were extracted. The differences in the structure function results and those obtained using nominal PF values were taken as the uncertainty due to PF values. The uncertainty in the PF values themselves is taken to be 0.1. The nominal PF values used in the analysis are shown in Table III.
4. Systematic uncertainty due to normalizing the elastic peak of simulation to data. This includes: an uncertainty of $(1 + E_b)\%$ (with E_b the beam energy in GeV) (see Sec. V D) and the statistical uncertainty of the data elastic or quasielastic peak (Fig. 9).

TABLE III. Nominal packing factor (PF) values used in the analysis for each combination of target type and beam energy. See Fig. 3 for the detailed naming convention of the target cells.

Beam Energy	Target Cell	PF Value
1.1 GeV	long NH_3 top	0.717
	long NH_3 bottom	0.625
1.3 GeV	long NH_3 bottom	0.657
	short NH_3	0.602
	ND_3	0.624
2.0 GeV	long NH_3 top	0.716
	ND_3	0.764
2.3 GeV	long NH_3 top	0.682
	short NH_3	0.720
3.0 GeV	long NH_3 top	0.782

(5) Systematic uncertainty due to CC efficiency. This was obtained by rerunning the analysis without applying the CC efficiency to the simulated spectra. The difference in the extracted g_1 and A_1F_1 from the nominal analysis indicates the effect of the CC efficiency, and 20% of this difference was taken as the systematic uncertainty due to the CC efficiency. Details of CC efficiency analysis were described in Sec. IV C.

(6) Systematic uncertainty due to background contributions. This includes effect from pion and pair production background (1% of the polarized yield, see Sec. IV D); ^{15}N elastic tail in the inelastic region (see Sec. V H); and the ^{15}N inelastic scattering background in the inelastic polarized yield, which contributes 0.7% of the polarized yield estimated by calculating the ^{15}N to proton inelastic polarized cross section ratio and applying the polarization ratio of the two.

(7) Systematic uncertainty due to event reconstruction. Even with momentum corrections applied to both data and simulation, the simulated elastic peak can differ from data in its W position by a small amount (typically 1–2 MeV or smaller). To estimate the uncertainty due to this effect, we shifted the simulated W spectra by +5 or −5 MeV, and reran the analysis. The difference in the extracted g_1 and A_1F_1 from the nominal analysis was then scaled by the actual shift in the elastic peak, obtained from figures such as Fig. 9. This uncertainty is typically very small except near the edge of the acceptance. When evaluating the integral of the structure functions, the data in the single W bin on the edge are not used because of this reason. Another reason to exclude data from the edges is that they very likely do not cover the full W range of the bin.

VI. RESULTS ON THE STRUCTURE FUNCTIONS

We present in this section results on the proton and the deuteron structure functions g_1 and A_1F_1, which were reported previously in Refs. [21,22]. We also present new results on the neutron g_1^n as extracted from the proton and deuteron data, as well as their isovector combination g_1^{p-n}.

A. Results on g_1 and A_1F_1 for the proton and deuteron

In the previous section, we described the method of extracting g_1 and A_1F_1 and the determination of systematic uncertainties on our results. The g_1 and A_1F_1 results obtained from all target types and beam energies were then combined. When doing so, we first checked whether any two data sets were compatible with each other, using Student's t-test to compare the distributions of both data sets in the region of common kinematics. The data were found to be consistent.

When combining the five beam energies, the spin structure function and its statistical uncertainty were determined as

$$g_1^{\rm combined} = \frac{\sum_i \frac{g_{1,E_b^i}}{\delta g^2_{1,E_b^i,\rm stat}}}{\sum_i \frac{1}{\delta g^2_{1,E_b^i,\rm stat}}}, \tag{52}$$

$$\delta g_{1,\rm stat}^{\rm combined} = \sqrt{\frac{1}{\sum_i \frac{1}{\delta g^2_{1,E_b^i,\rm stat}}}}, \tag{53}$$

where g_{1,E_b^i} and $\delta g_{1,E_b^i,\rm stat}$ are the g_1 value and its statistical uncertainty obtained from beam energy E_b^i $(i = 1, 2, 3, 4, 5)$. The systematic uncertainty was calculated as

$$\delta g_{1,\rm syst}^{\rm combined} = \frac{\sum_i \frac{\delta g_{1,E_b^i,\rm syst}}{\delta g^2_{1,E_b^i,\rm stat}}}{\sum_i \frac{1}{\delta g^2_{1,E_b^i,\rm stat}}}, \tag{54}$$

where $\delta g_{1,E_b^i,\rm syst}$ is the systematic uncertainty obtained for the data taken with beam energy E_b^i. That is, both experimental systematic and model uncertainties were weighted by the relevant statistical uncertainties of each beam energy. The same method was applied when combining data from different target cell types.

Our final results for g_1 and A_1F_1 of the proton and the deuteron are shown in Figs. 10 through 13. Our results are consistent with the previous data [102,103] where their coverage overlap, but extend the measured Q^2 range to three times smaller values, below the pion mass squared (m_π^2). This makes it possible to rigorously test χEFT calculations for the nucleon spin structure functions. Comparing to our existing A_1 model, which was based on existing data prior to EG4, one can see that it tends to be more positive than the data points, especially at lower Q^2. Our new data can help improve this model.

B. Results on neutron g_1

From our results on g_1 of the proton and the deuteron, we further extracted values for the neutron spin structure function, g_1^n, which were not available previously. This extraction is based on the simplified model of the deuteron structure functions described in Sec. II E, where the structure functions of the deuteron are expressed as sum of the two nucleon structure functions, convoluted with their spin and momentum distributions in the deuteron [115]. To extract the deconvoluted structure functions for a neutron at rest, we followed a

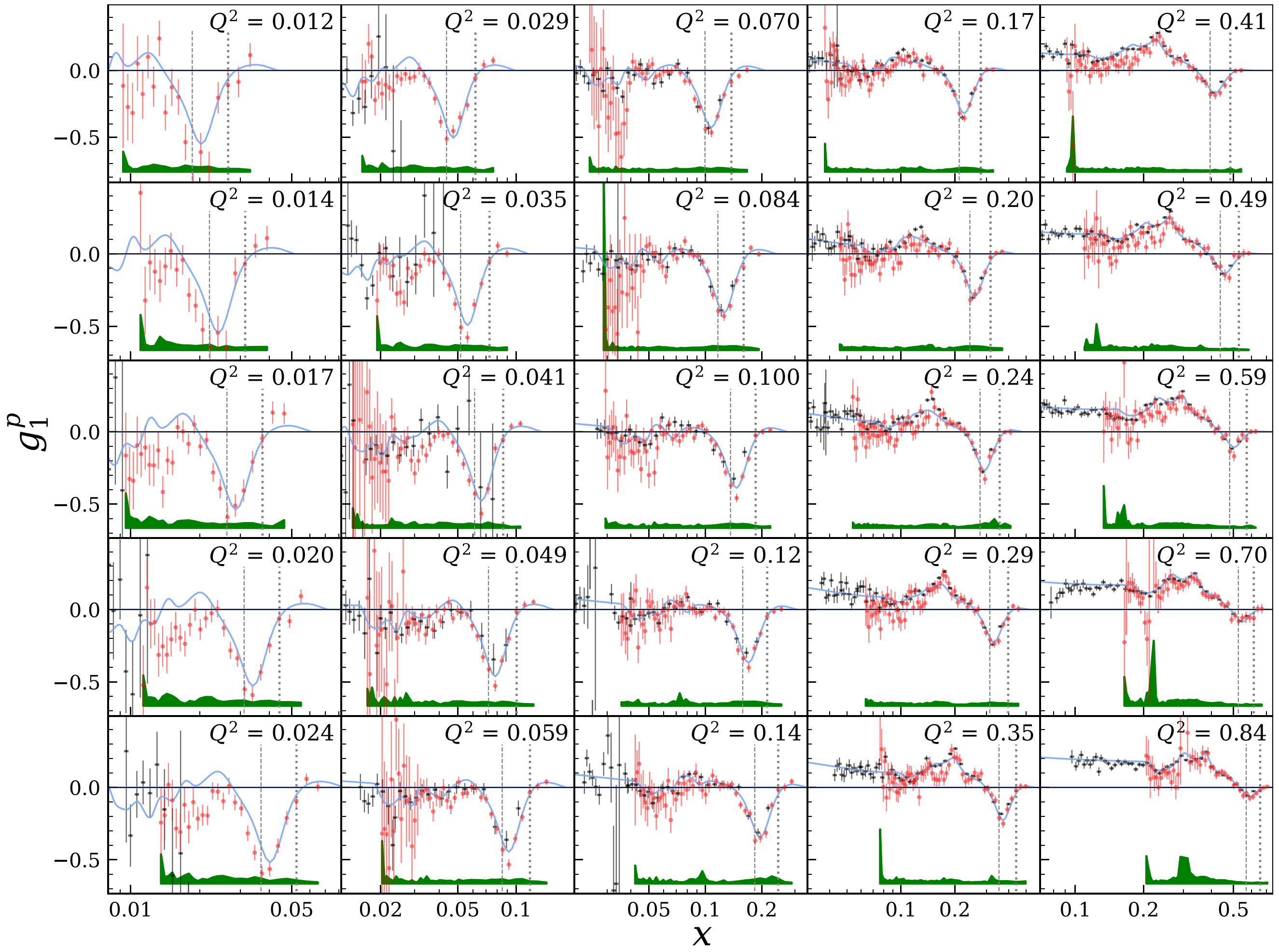

FIG. 10. Results on g_1 of the proton (red solid circles) plotted vs x, compared with our standard parametrization (blue curves) and results from EG1b (black crossbars) [102]. The error bars are statistical only. The total systematic uncertainty is shown as the green band on the bottom edge of each panel and includes both experimental systematics and that from models used in the analysis. The size of the total systematic uncertainty varies from 0.013−0.15 to 0.0045−0.19, and the relative size of the total systematic to statistical uncertainties varies from (8.0−33)% to (16−140)%, from the lowest to the highest Q^2 bins. The two vertical lines in each panel indicate the location of the Δ(1232) and the integration limit $x_{\rm hi}$ that corresponds to $W = 1.15$ GeV; see Sec. VII A. Note that the Q^2 bins (in GeV^2) are ordered column-wise, first from top to bottom, then from left to right.

similar procedure as for the extraction of $g_1^{p,d}$ from the data on the proton and deuteron, described in detail below.

As a first step, we took our g_1^p results and converted them to the contribution from the bound proton to the deuteron spin structure function using the folding technique of Ref. [115]. The bound g_1^p were then subtracted from our g_1^d results to obtain g_1 data for the bound neutron $g_1^{n,\rm data,bound}$. The data $g_1^{n,\rm data,bound}$ were compared with expected values for the bound neutron, $g_1^{n,\rm model,bound}$, produced using our model of the free neutron processed by the same folding technique, and any observed difference is attributed to how the input g_1^n model of the free neutron differs from reality. We then produced a *modification* of the base model $g_1^{n,\rm model-a(b),bound}$ where A_1 was changed by +0.1 (−0.1) in the input, and the difference between the *modified* and the original model provides information on how much the g_1^n model of the free neutron should be adjusted to match data. More specifically, g_1 for the free neutron is extracted as

$$g_1^{n,\rm (data,free)} = g_1^{n,\rm model,free} + \left(g_1^{n,\rm model-a(b),free} - g_1^{n,\rm model,free}\right) \times \frac{g_1^{n,\rm data,bound} - g_1^{n,\rm model,bound}}{g_1^{n,\rm model-a(b),bound} - g_1^{n,\rm model,bound}}. \quad (55)$$

Note that the two versions (a, b) of the modification produce nearly identical results. The statistical and experimental systematic uncertainties of each of the input g_1^p and g_1^d were propagated to produce the experimental uncertainties in the extracted g_1^n. The uncertainty in this extraction was studied using a similar method as in Sec. V G, but now by changing the initial model for the neutron.

Our results for g_1^n are shown in Fig. 14. Similar to the proton and the deuteron case, we see that the new results from EG4 are consistent with previous results in the region where

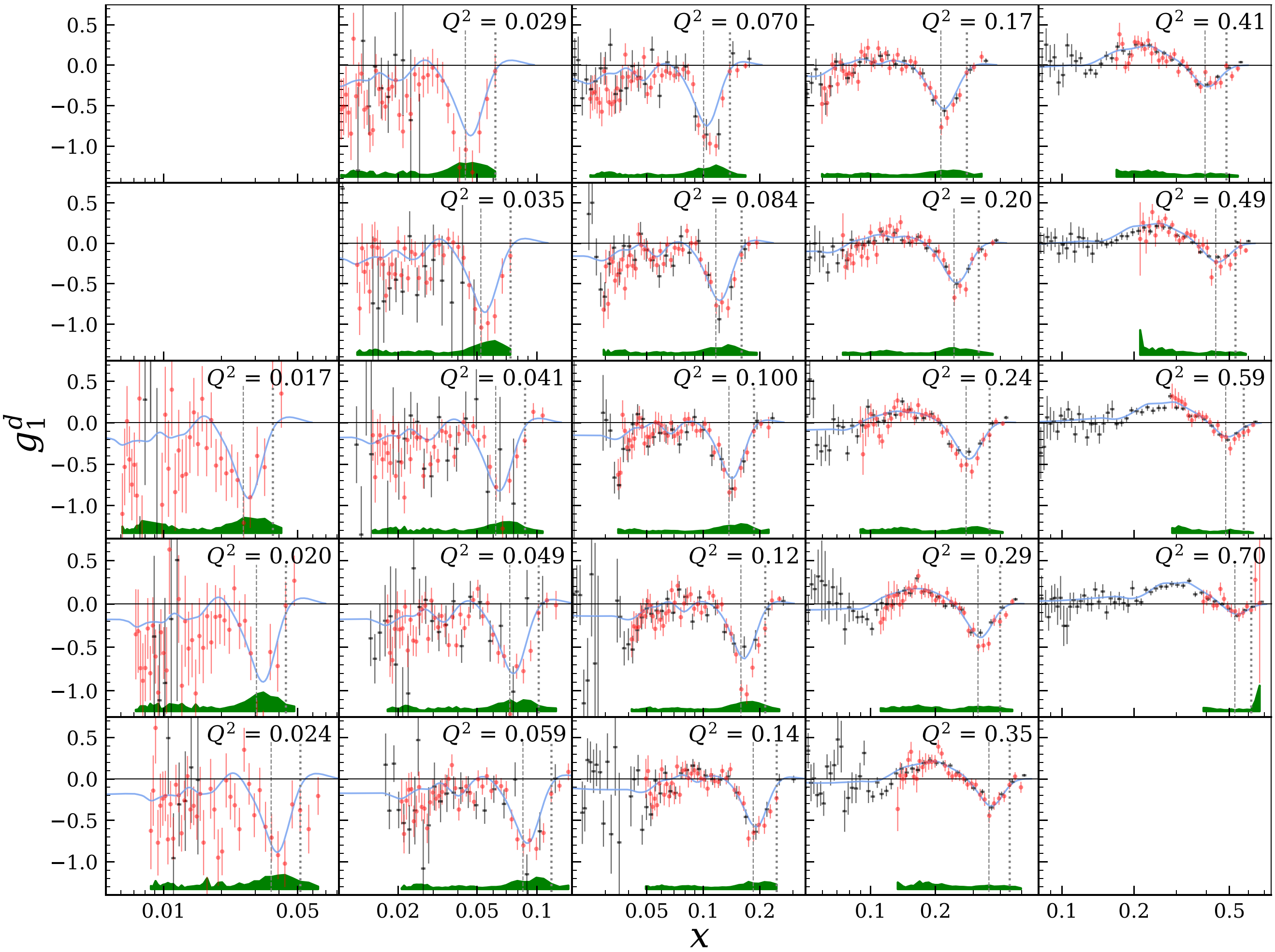

FIG. 11. Results on g_1 of the deuteron. The size of the total systematic uncertainty varies from 0.020−0.183 to 0.010−0.294, and the relative size of the systematic to statistical uncertainty varies from (4.3−52)% to (16−55)%, from the lowest to the highest Q^2 bins. See Fig. 10 caption for more details.

they overlap, but the best A_1 model can be improved in the lowest Q^2 bins, below about 0.1 GeV^2.

Finally, we show the isovector combination $g_1^{p-n}(x, Q^2)$ in Fig. 15. Comparing with Figs. 10, 11, and 14, one clearly observes the suppression in the isovector component of the $\Delta^{(1232)}$. This has important consequences for the Bjorken integral (i.e., the first moment of $g_1^{p-n}(x, Q^2)$), see Sec. VII F, and its comparison to χEFT [151]. Like the other EG4 results on g_1 and A_1F_1, Fig. 15 also makes clear that in the (x, Q^2) domain covered by EG4, the parametrization of the world data (continuous blue line) needs to be revised.

VII. RESULTS ON MOMENTS OF STRUCTURE FUNCTIONS

Similar to the previous section(s), we summarize the procedure to form the moments of the proton and the deuteron structure functions, and present the results that were reported previously in Refs. [21,22] but with updated χPT calculations. We also present new results on the moments of the neutron extracted directly from the moments of the proton and the deuteron, as well as their isospin combinations $\overline{\Gamma}_1^{p-n}$ and $\overline{\gamma}_0^{p\mp n}$.

A. General procedure used to form the integrals

To form moments of g_1 and A_1F_1, we integrated these quantities over the full range of $10^{-3} \leqslant x \leqslant x_{\text{th}}$ (x_{th} corresponds to the electroproduction threshold), using our model for the low and high x region beyond the data coverage. In addition, for a few high Q^2 bins the coverage of our data has gaps at intermediate W values because of disabled DC wires. The integrand over these gap regions was provided by the model as well. The full integral, e.g., $\overline{\Gamma}_1(Q^2)$ was therefore evaluated as

$$\begin{aligned}\overline{\Gamma}_1(Q^2) = & \int_{0.001}^{x_{\text{lo}}} g_1^{\text{mod}}(x, Q^2)dx \\ & + \int_{x_{\text{lo}}}^{x_{\text{hi}}} g_1^{\text{EG4 data}}(x, Q^2)dx + \int_{x_{\text{hi}}}^{x_{\text{th}}} g_1^{\text{mod}}(x, Q^2)dx \\ & + \int_{\text{gaps (when applicable)}} g_1^{\text{mod}}(x, Q^2)dx, \end{aligned} \tag{56}$$

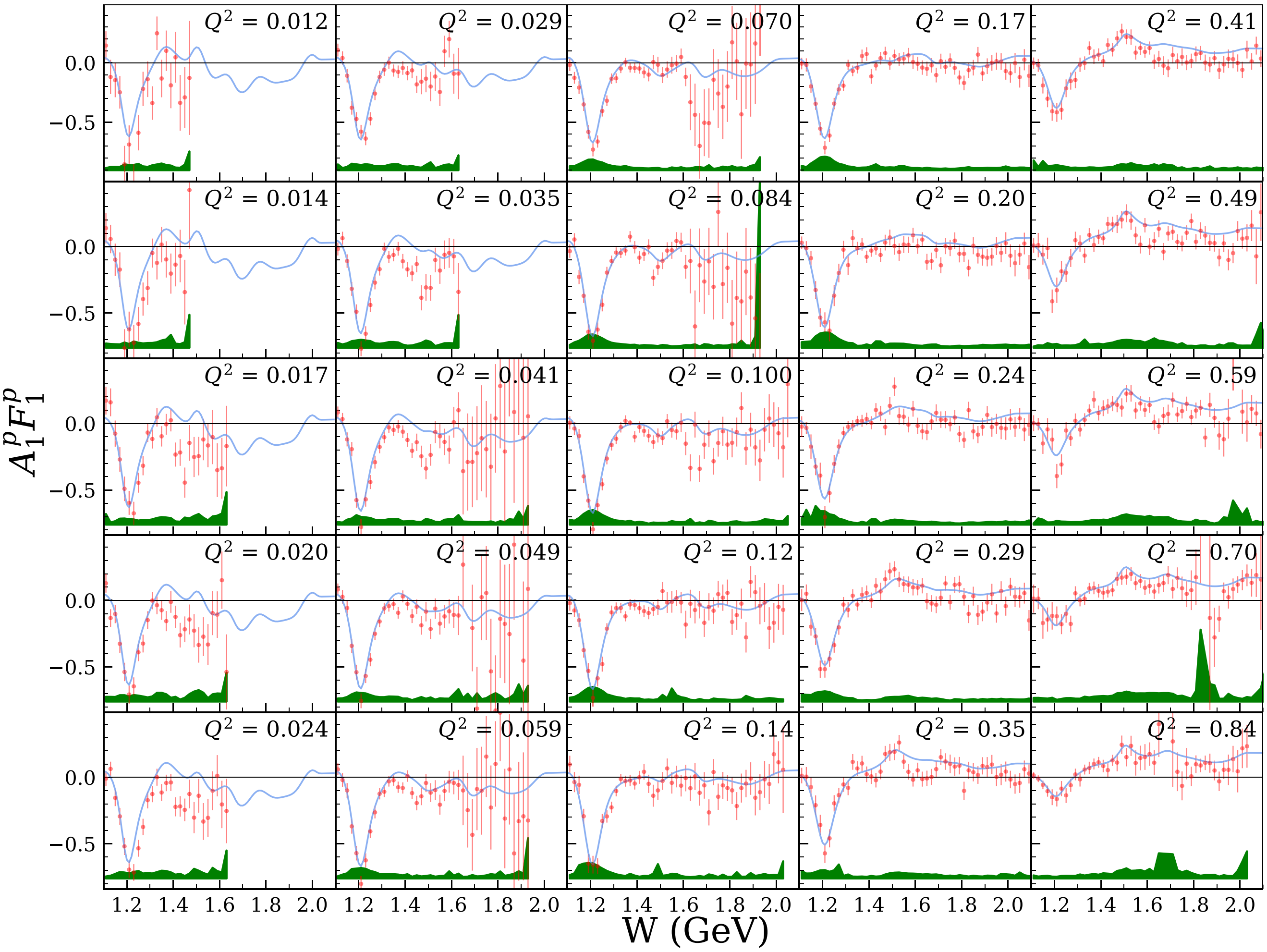

FIG. 12. Results on A_1F_1 of the proton plotted vs W to emphasize the contribution of different resonance regions. The size of the total systematic uncertainty varies from 0.0134−0.151 to 0.0045−0.190, and the relative size of the systematic to statistical uncertainty varies from (8.2−33)% to (8.0−118)%, from the lowest to the highest Q^2 bins. Note that earlier CLAS data [102] are not available for this quantity. See Fig. 10 caption for more details.

where $x_{\rm lo}$ and $x_{\rm hi}$ are the lower and upper limits of the data integration, $g_1^{\rm mod}$ is the estimate from our best model described in Sec. V F and $g_1^{\rm EG4\,data}$ is our data. The low-x integration starts at $x = 10^{-3}$ and the step size was set to $dx = 10^{-5}$.

The range $(x_{\rm lo}, x_{\rm hi})$ of the data integration in Eq. (56) is slightly narrower than the actual kinematic coverage of the experiment because the data uncertainties on the edge of the coverage are large: At large x, near the pion threshold $W \approx$ 1.07 GeV, the polarized yield is dominated by the radiative tail from elastic scattering and the measured polarized yield is not sensitive to the value of g_1 or A_1F_1; while for the low x or large W edge of the data, the spectrometer acceptance drops and the statistics of the data is low, see Sec. V I. Thus, the value of $x_{\rm hi}$ was chosen to be at $W = 1.15$ GeV and $x_{\rm lo}$ was set at a few tens of MeV below the maximum W covered by the data. The upper x limits of the data integration ranges are shown in Figs. 10 and 11.

Uncertainties in the model enters the integral in two ways. First, the model enters the extraction of the data itself, as described in Sec. V G. Second, the uncertainty of the model integration below $x_{\rm lo}$ and above $x_{\rm hi}$ was evaluated by variation of the model parameters, similar to the method described in Sec. V G. When evaluating model uncertainties of the data integral, the sign of each model uncertainty of g_1 or A_1F_1 is retained to allow partial cancellation when integrating. The total uncertainty on the full integral was formed by adding all experimental and model uncertainties in quadrature.

B. Latest χEFT moment predictions

In the following sections, we will compare the EG4 result on the moments to theoretical predictions, in particular from χEFT. We will display only two recent predictions, from Refs. [60,61], as they supersede earlier χEFT calculations [79,81,83,152]. The crucial advance of the latest calculations is that they account rigorously for the $\Delta^{(1232)}$ excitation. At the same time, the approaches by Refs. [60,61] have significant differences. The chief reason is the effective accounting of higher-order contributions of the χEFT series by Ref. [61], which uses a phenomenological form factor. It softens the steep Q^2-dependence otherwise seen in Ref. [60]. The softening form factor of Ref. [61] accounts for their typically

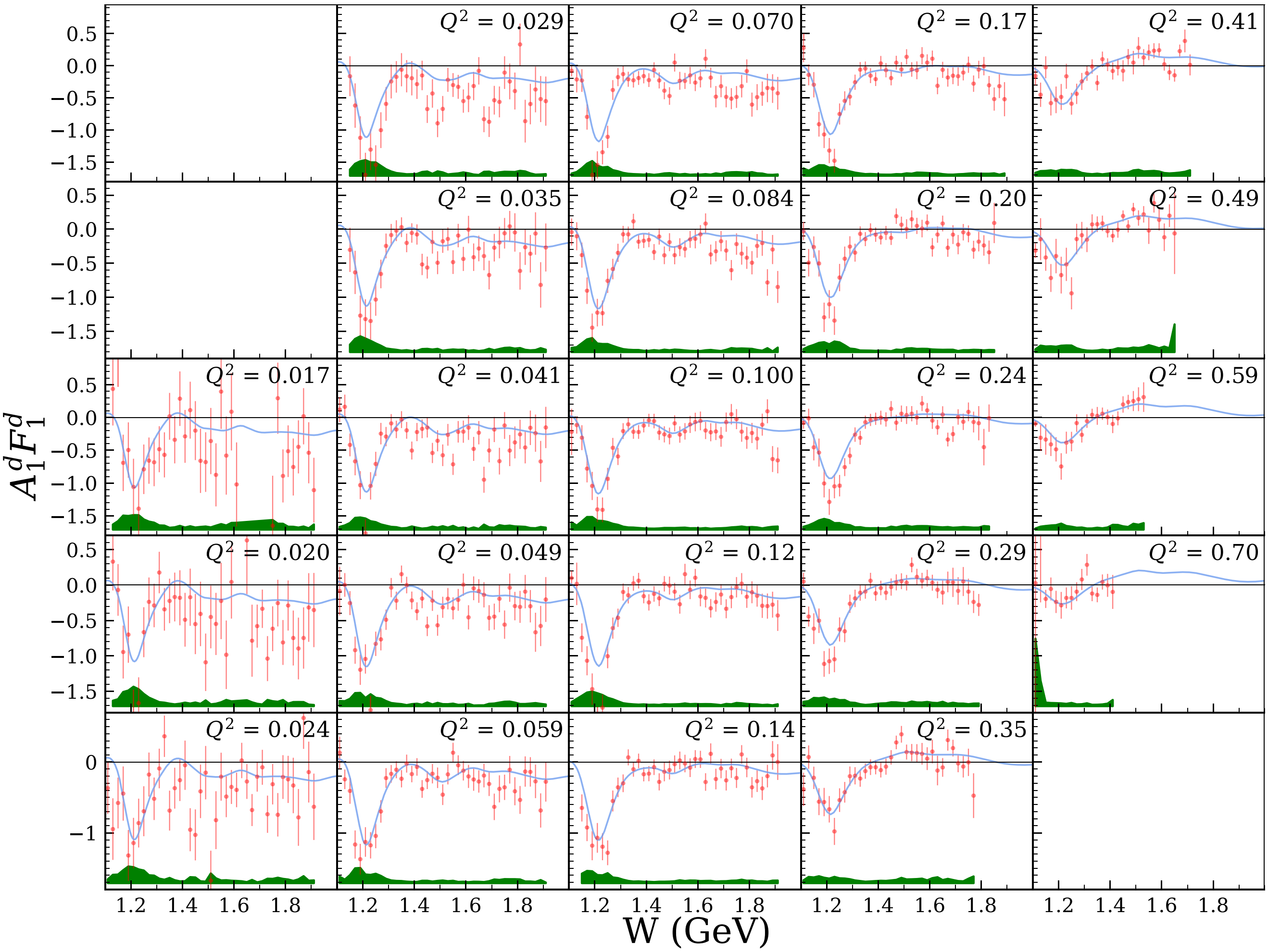

FIG. 13. Results on A_1F_1 of the deuteron plotted vs W to emphasize the contribution of different resonance regions. The size of the total systematic uncertainty varies from 0.020−0.22 to 0.019−0.952, and the relative size of the systematic to statistical uncertainty varies from (4.3−55)% in the lowest Q2 bin, to (18−39)%, from the lowest to the highest Q^2 bins. Note that earlier CLAS data [102] are not available for this quantity. See Fig. 10 caption for more details.

better description of the Q^2-dependence of moments. The methodological differences between the two calculations are detailed in Sec. VII G.

C. Moments of the proton spin structure functions

Our results on $\overline{\Gamma}_1^p(Q^2)$ [Eq. (33)] are shown in Fig. 16. They agree with the most recent χEFT predictions [60,61] up to $Q^2 \approx 0.03$ GeV^2, above which only that of Ref. [61] agrees with the data. The new $\overline{\Gamma}_1^p(Q^2)$ results generally agree with a previous experiment [102] in the overlapping Q^2 region within their uncertainties. However, it is visible that the parametrization based on Ref. [102] (purple solid curve) can be improved by including the new results. The phenomenological models Burkert and Ioffe [54,55] and Pasechnik *et al.* [57] agree well with the new results for all Q^2 values. They predict the behavior of $\overline{\Gamma}_1$ in the nonperturbative domain of QCD and beyond: The Burkert and Ioffe model [54,55] extrapolates DIS data using vector meson dominance and a parametrization of resonance contributions; while the Pasechnik *et al.* model [57], improved upon the earlier Soffer-Teryaev model [56], employs the analytical perturbation theory (APT) approach that extrapolates DIS data to low Q^2, accounting for the mild Q^2-dependence of $g_1 + g_2$. Lastly, the MAID unitary isobar phenomenological model [113] is a parametrization of experimental pion production data based on a partial wave analysis in the resonance region, and includes nonresonant background. MAID does not account for multiparticle final states and therefore provides a partial $\overline{\Gamma}_1(Q^2)$ in the resonance region, without the low-x (high-W) contribution. Consequently, it can be roughly compared with the experimentally measured $\overline{\Gamma}_1(Q^2)$ (open blue circles), although it does not necessarily have the same integration limits. With these caveats in mind, MAID and the EG4 measured sum agree well up to $Q^2 = 0.2$ GeV^2, after which the model is below the data.

Our results on $\overline{I}_{\rm TT}^p(Q^2)$ [Eq. (30)] are shown in Fig. 17. Compared with the χEFT predictions, similar conclusions as for $\overline{\Gamma}_1^p(Q^2)$ are reached. The MAID model still agrees with the experimentally measured integral within uncertainties. Finally, the difference between the new results and the parametrization of previous data [102]

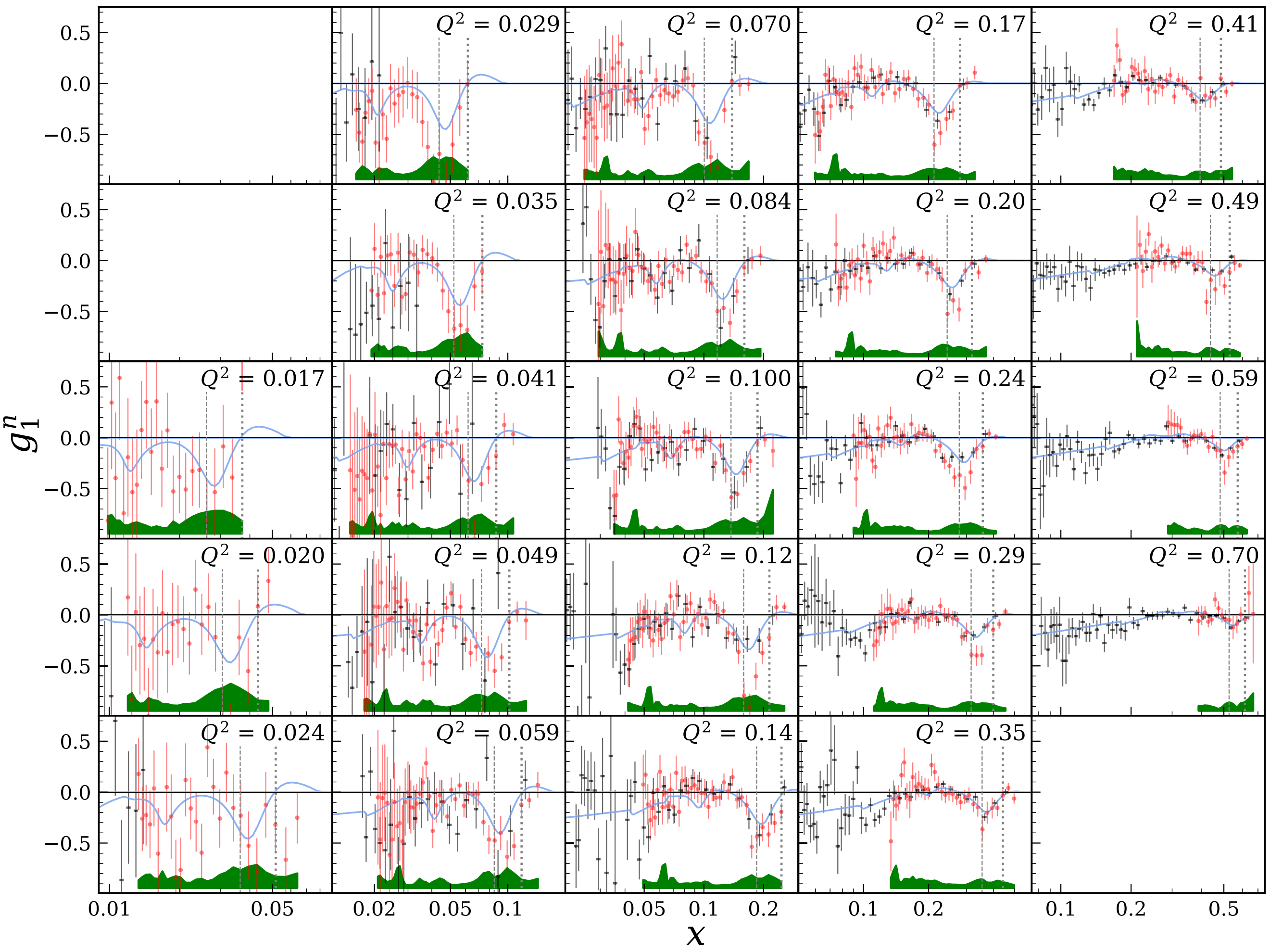

FIG. 14. Results on g_1 of the neutron (red solid circles) vs x extracted from deuteron and proton data. These are compared with our standard parametrization with the best A_1 model (blue curves) and results from EG1b (black crossbars) [102]. The error bars are statistical only. The total systematic uncertainty is shown as the green band on the bottom edge of each panel that includes both experimental systematics and that from models used in the analysis. The size of the total systematic uncertainty varies from 0.040−0.305 to 0.023−0.160, and the relative size of the systematic to statistical uncertainty varies from (10.7−55)% to (32−170)%, from the lowest to the highest Q^2 bins.

is more visible and the parametrization can clearly be improved.

Extrapolating our $\overline{I}^{p}_{\mathrm{TT}}(Q^2)$ results to $Q^2 = 0$ yields [22]

$$\overline{I}^{p\,\mathrm{EG4}}_{\mathrm{TT}}(Q^2 \to 0) = -0.798 \pm 0.042\,(\mathrm{tot}). \qquad (57)$$

This agrees well with the GDH sum rule prediction $I^{p\,\mathrm{theo}}_{\mathrm{TT}} = -\kappa^2/4 = -0.804(0)$ and the experimental photoproduction result $\overline{I}^{p\,\mathrm{exp}}_{\mathrm{TT}}(0) = -0.832 \pm 0.023\,(\mathrm{stat}) \pm 0.063\,(\mathrm{syst})$ [65–68]. We note that the uncertainties from Refs. [65–68] and Eq. (57) are comparable. For EG4, the uncertainty due to the $Q^2 \to 0$ extrapolation is compensated by the fact that inclusive electroproduction automatically sums over all reaction channels, removing uncertainties due to the detection of all final states needed in photoproduction. The EG4 data thus provide the first test of the GDH sum rule with a different technique than photoproduction.

One more moment that can be formed from the EG4 data is the generalized longitudinal spin polarizability $\overline{\gamma}_0(Q^2)$ [Eq. (35)]. Compared to $\overline{I}_{\mathrm{TT}}$ [Eq. (30)], the x^2-weighting in Eq. (35) indicates that $\overline{I}_{\mathrm{TT}}$ and $\overline{\gamma}_0$ have different contributions from both systematic and model uncertainties. Results for $\overline{\gamma}^{p}_0(Q^2)$ are shown in Fig. 18. They agree with χEFT calculation from Bernard *et al.* [60] only at very low Q^2 (below ≈0.03 GeV^2) and agree marginally with Alarcon *et al.* [61], though both calculations have large uncertainties. However, when combined with the photoproduction data point [153], the EG4 results support the larger slope at very low Q^2 predicted by Bernard *et al.* [60]. The agreement between the measured integrals and the MAID model is similar to both $\overline{\Gamma}^{p}_1$ and $\overline{I}^{p}_{\mathrm{TT}}$. The recent calculation by Bigazzi *et al.* [154] (not shown in the figure) based on the anti-de Sitter/conformal field theory (AdS/CFT) correspondence [155] applied to QCD [156] recovers the sign and qualitative behavior of $\overline{\gamma}^{p}_0(Q^2)$, albeit up to a normalization factor.

D. Moments of the deuteron spin structure functions

Results for the deuteron moments $\overline{I}^{d}_{\mathrm{TT}}$, $\overline{\Gamma}^{d}_1$, and $\overline{\gamma}^{d}_0$ are shown in Figs. 19–21, respectively. The bar now indicates

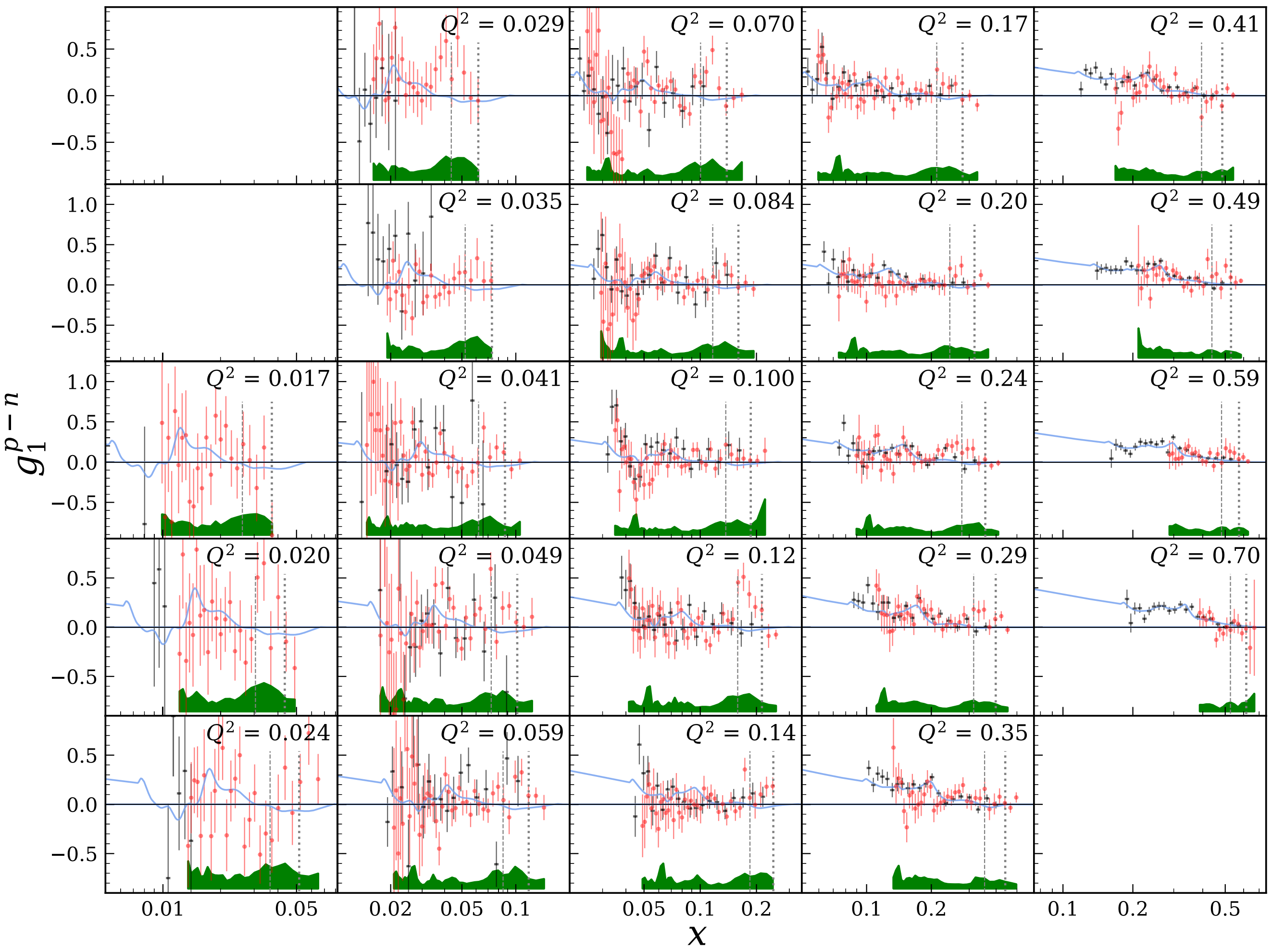

FIG. 15. Results on the isovector component g_1^{p-n}. Across all Q^2 bins, the size of the total systematic uncertainty varies from 0.022 to 1.013, while the relative size of the total systematic to statistical uncertainty varies within (7.7−173)%. See Fig. 14 caption for more details.

that, in addition to the elastic reaction, the deuteron electrodisintegration contribution is also excluded from the integrals. Therefore, they approximately correspond to the sum of the proton and neutron moments rather than to the deuteron nucleus (see Sec. II E).

Similar observations as for the proton measurements can be drawn: the EG4 data agree with the previous data from CLAS [102] (and from SLAC E143 [107], not shown in the figure). The measured $\overline{\Gamma}_1^d$ and $\overline{I}_{\mathrm{TT}}^{d\,\mathrm{exp}}(Q^2)$ agree with the χEFT results for the sum of proton and neutron (multiplied with the D-state depolarization, see Sec. II E) of Alarcón *et al.* [61], and of Bernard *et al.* [60] for the lowest Q^2 points. The models of Pasechnik *et al.* [57] and Burkert-Ioffe [54,55] agree well with the $\overline{\Gamma}_1^d$ data, while the parametrization [102] is systematically slightly larger. The comparison between the MAID model and the data is similar to that of the proton for all three integrals.

Extrapolating the $\overline{I}_{\mathrm{TT}}^d(Q^2)$ data to $Q^2 = 0$ yields [21]

$$\overline{I}_{\mathrm{TT}}^{d\,\mathrm{EG4}}(Q^2 \to 0) = -1.724 \pm 0.057\,(\mathrm{tot}), \tag{58}$$

which agrees at the 1.5σ level with the GDH sum rule prediction -1.574 ± 0.026, obtained using Eq. (37), where the uncertainty is from the deuteron D-state correction. This can be compared with the data using real photons of energy between $0.2 < \nu < 1.8$ GeV, $\overline{I}_{\mathrm{TT}}^{d\,\mathrm{exp}}(0) = -1.986 \pm 0.008\,(\mathrm{stat}) \pm 0.010\,(\mathrm{syst})$ [65]. Note that the systematic uncertainty of [65] does not include that from the unmeasured low and large ν contributions.

Regarding the generalized spin polarizability $\overline{\gamma}_0^d$, the EG4 results are clearly outside the range predicted by Alarcón *et al.* [61], but agree with the Bernard *et al.* calculation for the lowest Q^2 points. The parametrization [102] does not describe the data well below $Q^2 = 0.1$ GeV^2, similarly to the $\overline{I}_{\mathrm{TT}}^d(Q^2)$ case.

E. Moments of the neutron spin structure functions

Moments of the neutron spin structure function can be extracted directly from those of the proton and neutron results, see Sec. II E. Understanding the deuteron moments as "per nucleus" (rather than "per nucleon"), we rewrite Eqs. (36)–(38) as

$$\overline{\Gamma}_1^n = \overline{\Gamma}_1^d/(1-1.5\omega_D) - \overline{\Gamma}_1^p, \tag{59}$$

$$\overline{I}_{\mathrm{TT}}^n = \overline{I}_{\mathrm{TT}}^d/(1-1.5\omega_D) - \overline{I}_{\mathrm{TT}}^p, \tag{60}$$

$$\overline{\gamma}_0^n = \overline{\gamma}_0^d/(1-1.5\omega_D) - \overline{\gamma}_0^p, \tag{61}$$

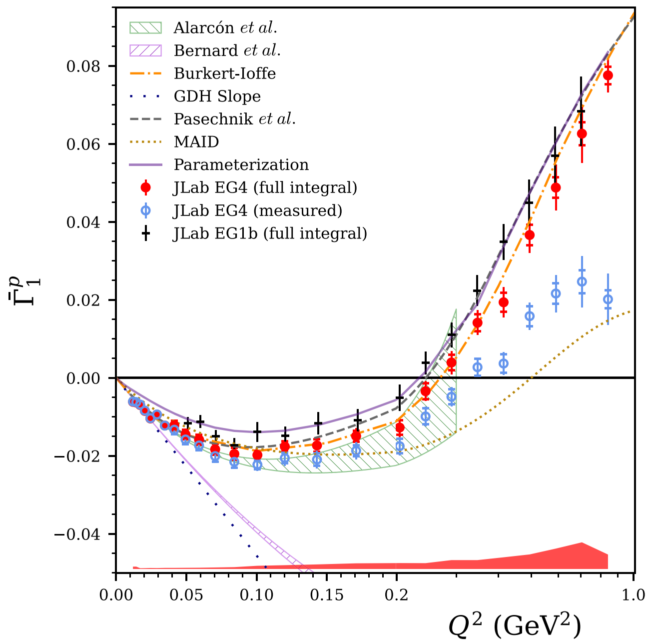

FIG. 16. EG4 results on the proton $\overline{\Gamma}_1^p(Q^2)$. Integrals over the full (experimentally covered) x range are shown as solid red (open blue) circles. The inner and the outer error bars (sometimes too small to be seen) are for statistical and total uncertainties, respectively. To illustrate their relative contributions, we also show the systematic uncertainty as the (red colored) band at the bottom of the figure, which includes both experimental systematic and model uncertainties. Across all Q^2 bins, the size of the systematic uncertainty varies from 0.0002 to 0.0068, while the relative size of the systematic to statistical uncertainty varies within (23−233)%. These results are compared with earlier data from CLAS [102] (solid black crossbars), χEFT predictions by Alarcón *et al.* [61] (green backslash hatched band) and Bernard *et al.* [60] (magenta forward-slash hatched band), phenomenological models by Burkert and Ioffe [54,55] (orange dot-dashed curve) and Pasechnik *et al.* [57] (gray dashed curve), and our own spin structure function parametrization [102] (purple solid curve). The MAID model [113] that includes only one-pion production contributions is shown by the (yellow) dotted curve. The GDH slope (black dotted line) is the GDH sum rule expectation for $Q^2 \to 0$. See texts for detailed discussions.

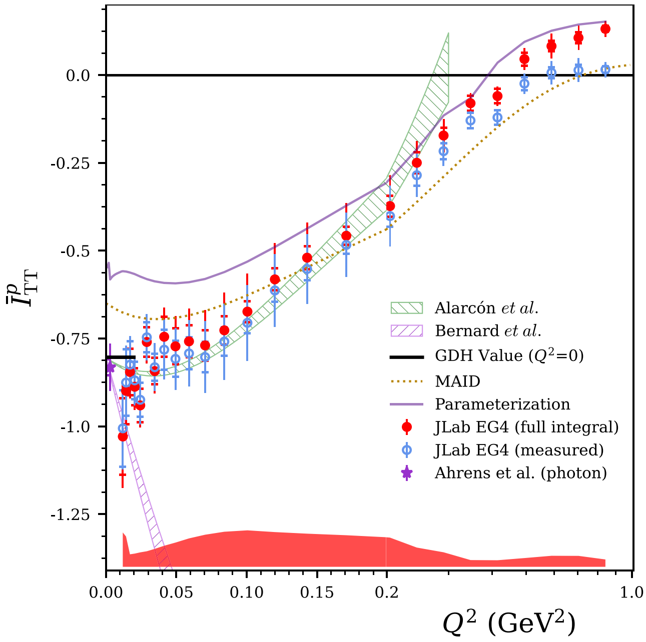

FIG. 17. EG4 results on the proton $\overline{I}_{\mathrm{TT}}^p(Q^2)$. Across all Q^2 bins, the size of the systematic uncertainty (red colored band) varies from 0.186 to 0.104, while the relative size of the systematic to statistical uncertainty varies within (54−357)%. The GDH value is shown as the short horizontal line, at $\overline{I}_{\mathrm{TT}}^p(0) = -0.804$. The result from the photoproduction experiment [65–68] is shown as the solid purple star at $Q^2 = 0$. Note that earlier CLAS data [102] and the phenomenological model predictions [55,57] are not available for this integral. See Fig. 16 caption for more details.

with ω_D given previously under Eq. (38). When extracting the neutron moments as above, we added in quadrature the proton and deuteron statistical uncertainties, as well as the systematic uncertainties.

The resulting $\overline{\Gamma}_1^n(Q^2)$ and $\overline{I}_{\mathrm{TT}}^n(Q^2)$ are shown in Figs. 22 and 23, respectively. They agree with previous data from E143 [107], EG1a [94,95], and EG1b [102,103] where the neutron information was extracted from the combined deuteron and proton data, as well as those from E94-010 [93] and E97-110 [71] for which the neutron information was extracted from ^{3}He data. There is also agreement with the phenomenological models of Burkert and Ioffe [54,55] and Pasechnik *et al.* [57] (when available) and with the χEFT predictions from Bernard *et al.* [60] (up to $Q^2 \simeq 0.08$ GeV^2) and, to a lesser extent, with Alarcón *et al.* [61]. The MAID model prediction is systematically more positive than the data. Like in the case of $\overline{\gamma}_0^n$, the calculation of [154] (not shown in the figure) agrees in sign and behavior with the $\overline{\gamma}_0^n(Q^2)$, up to a similar normalization factor as for $\overline{\gamma}_0^p(Q^2)$.

The real photon GDH sum for the neutron can be deduced from Eqs. (57) and (58):

$$\overline{I}_{\mathrm{TT}}^{n\,\mathrm{EG4}}(Q^2 \to 0) = -1.084 \pm 0.130\,(\mathrm{tot}), \qquad (62)$$

where the uncertainty arises from the uncertainties of proton, deuteron, and the D-state component added linearly. This agrees within $\approx 1.3\sigma$ from the sum rule expectation, $\overline{I}_{\mathrm{TT}}^{n\,\mathrm{theo}}(0) = -0.915(0)$.

Results on the generalized longitudinal spin polarizability on the neutron are shown in Fig. 24, along with earlier results from JLab (EG1b [102,103], E97-110 [71], and E94-010 [93]). The EG4 neutron results generally agree with the earlier data, though there is a tension between EG4 and E97-110 for $Q^2 \lesssim 0.1$ GeV^2. Adding the EG4 deuteron and proton systematic uncertainties linearly, rather than in quadrature, does not remove the tension. It contrasts with the agreement between EG4 and E97-110 for the neutron data on $\overline{\Gamma}_1^n$ or $\overline{I}_{\mathrm{TT}}^n$, suggesting the discrepancy arises from the high-x (near pion threshold) contribution. The EG4 results agree with χEFT calculation from Ref. [60] up to $Q^2 \approx 0.1$ GeV^2 but not with that of Alarcón *et al.* [61].

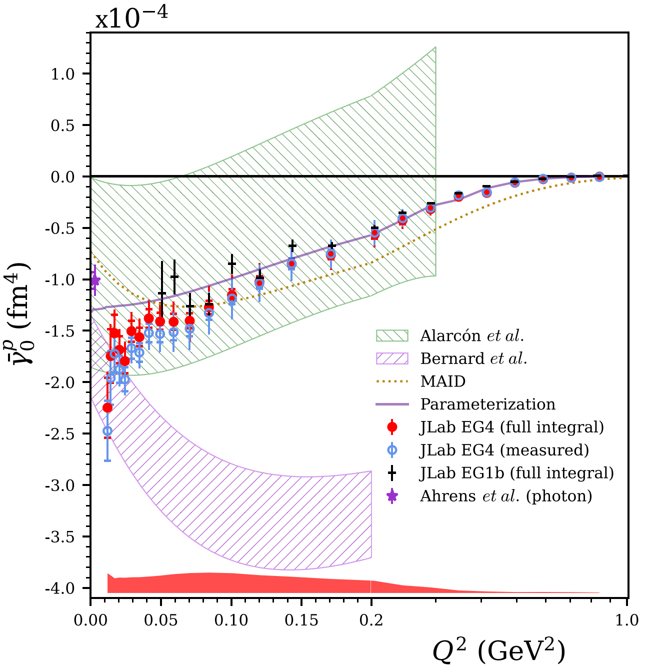

FIG. 18. EG4 results on the proton $\overline{\gamma}_0^p(Q^2)$. Across all Q^2 bins, the size of the systematic uncertainty (red colored band) varies from 0.0045 to 0.198 ($\times 10^{-4}$ fm^4), while the relative size of the systematic to statistical uncertainty varies within (66–364)%. The photoproduction data point [153] is slightly displaced from $Q^2 = 0$ (purple star). Note that phenomenological model predictions [55,57] are not available for this integral. See Fig. 16 caption for more details.

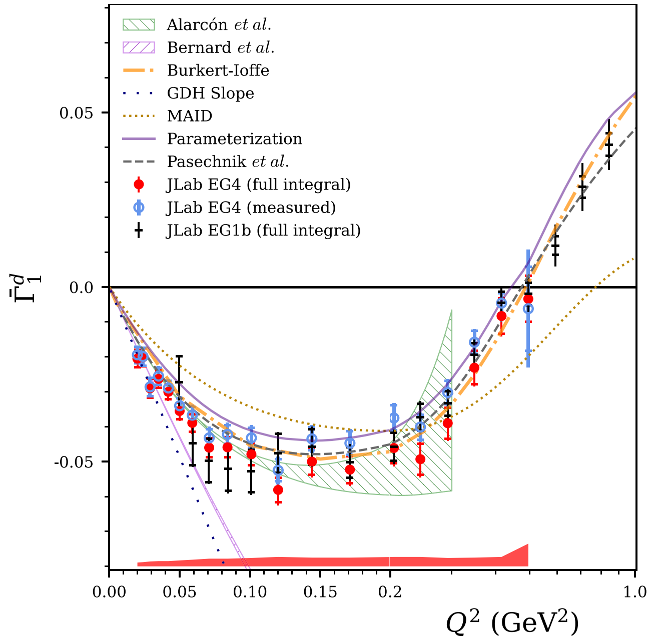

FIG. 19. EG4 results on the deuteron $\overline{\Gamma}_1^d(Q^2)$. The size of the systematic uncertainty (red colored band) varies from 0.0011 to 0.0065, while the relative size of the systematic to statistical uncertainty varies within (44–98)%, from the lowest to the highest Q^2 bins. See Fig. 16 caption for more details.

F. Isospin analysis on the moments of spin structure functions

Results on the proton and deuteron moments presented in the previous sections can be used to form various isospin combinations based on the description in Sec. II E. The isoscalar $(p+n)$ combination would be similar to the deuteron results, up to a factor $\approx 1/0.92$ from the deuteron D-state. For isovector $(p-n)$ moments, the proton and deuteron results were combined as

$$\overline{\Gamma}_1^{p-n} = 2\overline{\Gamma}_1^p - \overline{\Gamma}_1^d/(1-1.5\omega_D), \tag{63}$$

$$\overline{\gamma}_0^{p-n} = 2\overline{\gamma}_0^p - \overline{\gamma}_0^d/(1-1.5\omega_D), \tag{64}$$

where ω_D is given under Eq. (38) and with the deuteron moments understood as "per nucleus." Alternatively to using the EG4 proton and deuteron data, one can use the proton results from EG4 and the neutron results obtained from ^{3}He data such as those from JLab E97-110 [71] to perform the isospin separation.

The isovector moments are expected to be simpler to compute than the isoscalar or nucleon moments. For lattice QCD simulations, this is because the disconnected diagrams are suppressed [17]. For χEFT calculations, e.g., Refs. [61,151], the inclusion of the $\Delta^{(1232)}\,3/2^+$ excitation is often difficult, which would cancel in the isovector combination. However, the consequence of the expectation that the χEFT predictions are more robust has been upheld only with data on the Bjorken sum $\overline{\Gamma}_1^{p-n}$ [43–45], but not with $\overline{\gamma}_0^{p-n}$ [44], nor with the longitudinal-transverse interference polarizability δ_{LT} [19,104] for which the $\Delta^{(1232)}$ contribution is also expected to cancel. Our results provide improved tests of this expectation thanks to the lower Q^2 coverage and higher precision of EG4 data.

1. *Results on the Bjorken sum* $\overline{\Gamma}_1^{p-n}(Q^2)$

The isovector combination $\overline{\Gamma}_1(Q^2)$ is the Bjorken sum [28,29], see Eqs. (25)–(32). Our results on $\overline{\Gamma}_1^{p-n}(Q^2)$ are shown in Fig. 25, compared with data from earlier experiments [43–45,106]. Besides the models already discussed in connection with Figs. 16–24, we also show predictions from holographic light-front QCD (HLFQCD) [156]. In HLFQCD, the QCD coupling α_s is derived in the g_1 scheme following the effective charge prescription [7,8,157], from which the Bjorken sum can be obtained [158–160].

Note the comparison between the $\overline{\Gamma}_1^{p-n}$ results obtained from EG4's proton and deuteron data and those extracted from the EG4 proton and E97-110 neutron (^{3}He) data. An agreement between the two different approaches was not assured since the nuclear structures of the deuteron and ^{3}He are quite different: ^{3}He is strongly bound compared to the deuteron, therefore more sensitive to potential nuclear modification of the proton. Our treatment of the deuteron is minimal and consists of accounting for its D-state [116–120], while treatment of the ^{3}He data accounted for the nucleon effective polarizations [162]. As shown in Fig. 25, the two approaches agree well with each other. This suggests that, at least for $\overline{\Gamma}_1^{p-n}$, the nuclear corrections applied to the deuteron and ^{3}He data to

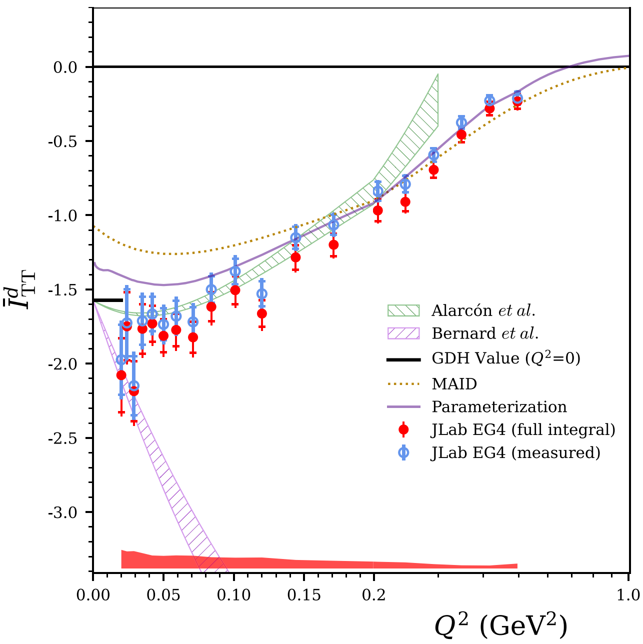

FIG. 20. EG4 results for the deuteron $\bar{I}^d_{\rm TT}(Q^2)$. Across all Q^2 bins, the size of the systematic uncertainty (red colored band) varies from 0.0198 to 0.125, while the relative size of the systematic to statistical uncertainty varies within (42–83)%. The expected GDH value $\bar{I}^d_{\rm TT}(0) = -1.574 \pm 0.026$ is shown by the short horizontal line. Note that earlier CLAS data [102] and the phenomenological model predictions [55,57] are not available for this integral. See Fig. 16 caption for more details.

obtain the neutron information appear sufficient at these low Q^2 values.

Both the EG4 and EG4/E97-110 results on $\overline{\Gamma}_1^{p-n}$ are systematically above χEFT and model predictions, except that of HLFQCD [59] and [161], which agree with the data. To allow a quantitative comparison between the data and theory, we employed a fit of the form $bQ^2 + cQ^4$ to the entire world data set, based on Eq. (32) [53], where b is expected to be the GDH slope. Our results are shown in Table IV. The "*uncor*" uncertainty designates the point-to-point uncorrelated uncertainty. It is the quadratic sum of the statistical uncertainty and a fraction of the systematic uncertainty determined so that $\chi^2/\text{n.d.f} = 1$ for the best fit. The "*cor*" uncertainty is the correlated uncertainty estimated from the remaining fraction of the systematic uncertainty.

We note that our value for b deviates significantly from that expected from the GDH sum rule. This is partially due to the large cancellation for the GDH sum rule in the p-n combination, which is only 1/4 of the value for the individual nucleons. Experimentally, because of the nearly perfect cancellation of the large contribution from the $\Delta^{(1232)}$ resonance in the p-n difference, the isovector integral is much more strongly affected by small-x contributions than the other moments, with relatively large uncertainties for $g_1^p - g_1^n$. Of course, our results could also indicate a much stronger Q^2-dependence near the photon point than can be captured by a two-parameter fit. In any case, they do not indicate a violation of the GDH

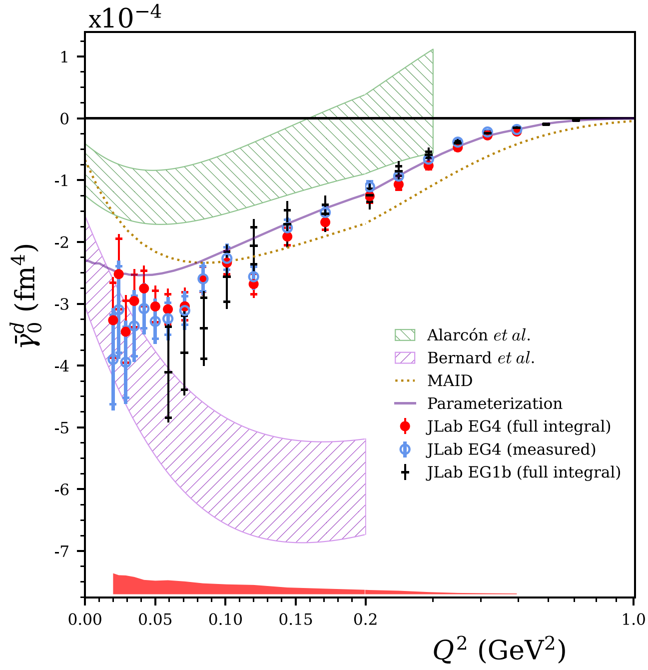

FIG. 21. EG4 results on the deuteron $\overline{\gamma}^d_0(Q^2)$. Across all Q^2 bins, the size of the systematic uncertainty (red colored band) varies from 0.0123 to 0.339 ($\times 10^{-4}$ fm^4), while the relative size of the systematic to statistical uncertainty varies within (37–93)%. Note that phenomenological model predictions [55,57] are not available for this integral. See Fig. 16 caption for more details.

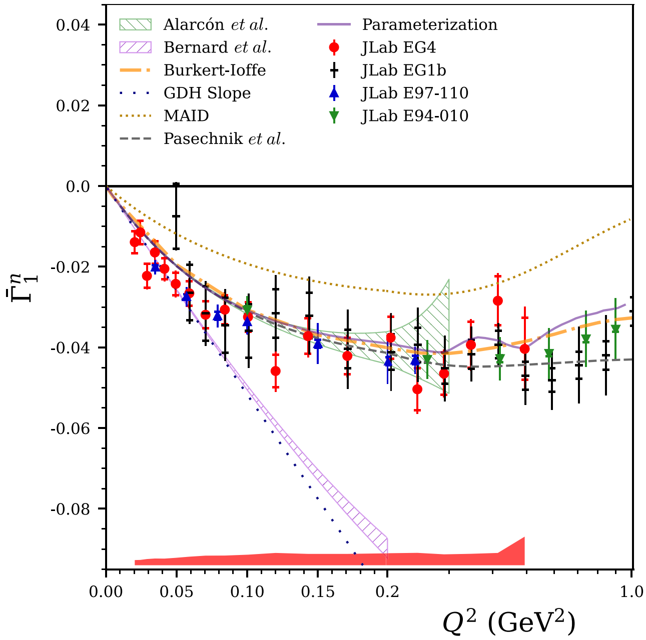

FIG. 22. EG4 results on the neutron $\overline{\Gamma}^n_1(Q^2)$, compared with earlier results from EG1b (d,p) [102,103] (black crossbars), JLab E97-110 (neutron extracted from ^{3}He) [71] (blue triangles), and E94-010 (^{3}He) [93] (green triangles). The size of the systematic uncertainty (red colored band) varies from 0.0013 to 0.0071, while the relative size of the systematic to statistical uncertainty varies from (45–92)%, from the lowest to the highest Q^2 bins. See Fig. 16 caption for more details.

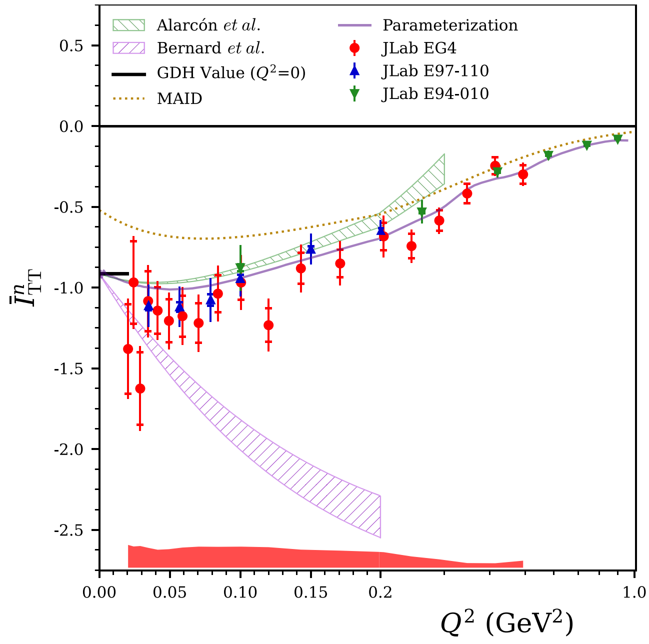

FIG. 23. EG4 results on the neutron $\bar{I}^n_{\mathrm{TT}}(Q^2)$, compared with results from JLab E94-010 (^{3}He) [92] (green triangles) and E97-110 (^{3}He) [71] (blue triangles). Across all Q^2 bins, the size of the systematic uncertainty varies from 0.0275 to 0.141, while the relative size of the systematic to statistical uncertainty varies within (49−123)%. The GDH value is shown as the short horizontal line at $\bar{I}^n_{\mathrm{TT}}(0) = -0.915$. Note that earlier CLAS data [102] and the phenomenological model predictions [55,57] are not available for this integral. See Fig. 16 caption for more details.

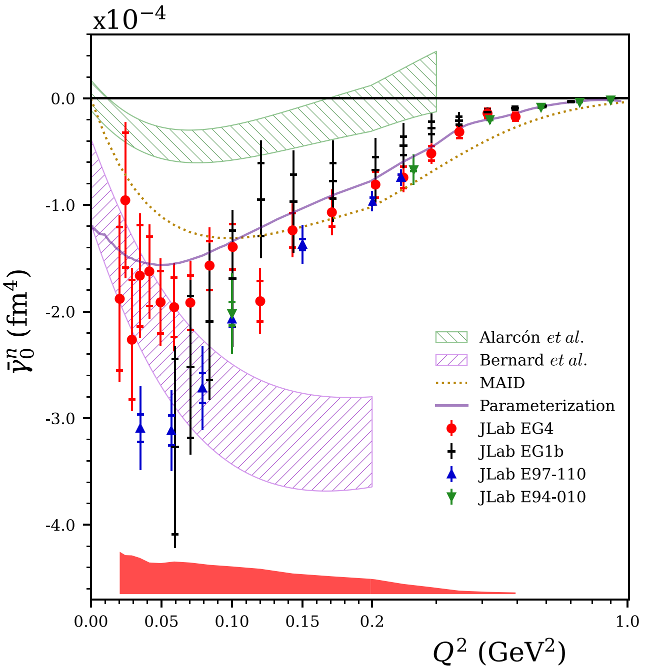

FIG. 24. EG4 results on the generalized spin polarizability $\bar{\gamma}^n_0$, compared with earlier results from JLab EG1b (proton and deuteron) [102,103] (black crossbars), E97-110 (^{3}He) [71] (blue triangles), and E94-010 (^{3}He) [93] (green triangles). Across all Q^2 bins, the size of the systematic uncertainty varies from 0.0158 to 0.397 ($\times 10^{-4}$ fm^4), while the relative size of the systematic to statistical uncertainty varies from (40−124)%. Note that phenomenological model predictions [55,57] are not available for this integral. See Fig. 16 caption for more details.

sum rule since, as shown in the previous section, our results for the proton and neutron are individually consistent with the sum rule within (1–1.3)σ. Further discussions on the possible discrepancy between the b parameter and the GDH slope can be found in Ref. [53].

2. Isospin study of $\bar{\gamma}_0(Q^2)$

Our results on the isovector and isoscalar combination of $\bar{\gamma}_0(Q^2)$ from EG4 are shown in Fig. 26. We also provide results based on EG4 p data and E97-110 n(^{3}He) data [104]. The total experimental systematic uncertainties on the proton and deuteron/neutron(^{3}He) are combined quadratically, as are the statistical uncertainties. The low-x uncertainties are added linearly. The results shown in Fig. 26 agree reasonably well with those from the previous experiments EG1b and EG1b/E94-010 [44]. However, unlike for $\bar{\Gamma}^{p-n}_1$, results from the EG4-only and EG4/E97-110 approaches agree only at the higher Q^2 points. On the other hand, if we combine linearly the total systematic uncertainties of the two experiments, then the tension at low Q^2 vanishes.

For $\bar{\gamma}^{p-n}_0(Q^2)$, both the EG4 and EG4/E97-110 results indicate that it stays positive in the measured Q^2 range, conversely to the χEFT and MAID predictions. In the case of $\bar{\gamma}_0(Q^2)^{p+n}$, both the EG4 and EG4/E97-110 combinations agree with Bernard *et al.* in the lower Q^2 range, but disagree with the Alarcón *et al.* prediction.

G. Discussions

As discussed in previous sections, the success of χEFT in describing our results on the moments of the spin structure function remains limited. One reason for this limited success may be coming from the difficulty to fully account for the $\Delta^{(1232)}$ degree of freedom in the calculation. In fact, early χEFT calculations [79,152] did not include explicitly the $\Delta^{(1232)}$ excitation, which slows the convergence of the χEFT perturbation series, or they included it phenomenologically [81,83]. This was thought to not be important for some observables for which the $\Delta^{(1232)}$ contribution was expected to be suppressed, such as the longitudinal-transverse spin polarizability δ_{LT} and the isovector quantities $\bar{\Gamma}^{p-n}_1$ [151] or $\bar{\gamma}^{p-n}_0$. It therefore came as a surprise that much of the early nucleon spin structure function data [92] disagreed with calculations [79,81,83,152], noticeably δ^n_{LT} and $\bar{\gamma}^{p-n}_0$. This puzzle prompted refined χEFT calculations [60,61] and a new experimental program at JLab optimized to cover the χEFT domain [21,71,163], including the EG4 experiment reported here.

The latest χEFT calculations by Bernard *et al.* [60] and Alarcón *et al.* [61] both included the $\Delta^{(1232)}$ but differ in their expansion method for the π(pion)-$\Delta^{(1232)}$ corrections. In χEFT, the general expansion parameter is $m_\pi/\Lambda_{\chi\mathrm{SB}}$, where $m_\pi \approx 0.1$ GeV and $\Lambda_{\chi\mathrm{SB}} \approx 1$ GeV is the chiral symmetry breaking scale. To explicitly account for the $\Delta^{(1232)}$, the

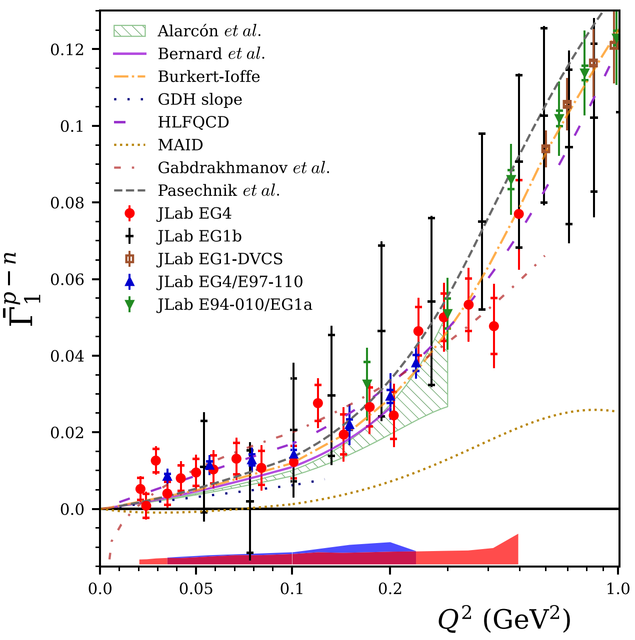

FIG. 25. The Bjorken sum $\overline{\Gamma}_1^{p-n}(Q^2)$ from EG4 (solid red circles) and from the EG4 proton data combined with the JLab E97-110 neutron data [71] (blue triangles). Also shown are earlier data from E94-010/EG1a [43] (green triangles), CLAS EG1b [44] (black crossbars), and EG1dvcs [45] (brown open squares). The inner (outer) error bars on the data points give their statistical (total) uncertainties, while the systematic uncertainties of EG4 and EG4/E97-110 are also given by the red and the blue bands, respectively. Across all Q^2 bins, the size of the systematic uncertainty of the EG4 results (red colored band) varies from 0.0017 to 0.0115, while the relative size of the systematic to statistical uncertainty varies from (58−131)%. The χEFT predictions from Alarcón *et al.* [61] and Bernard *et al.* [60] (the latter without error band as given in Ref. [60]) are shown along with phenomenological model predictions from Burkert-Ioffe [54,55], Pasechnik *et al.* [57], MAID [113], HLFQCD [59], and Gabdrakhmanov *et al.* [161].

TABLE IV. Best fit of the world data on $\overline{\Gamma}_1^{p-n}$ over the range $0.021 \leqslant Q^2 \leqslant 0.244$ GeV^2. The fit form used is $bQ^2 + cQ^4$. The meaning of the "uncor" and "cor" uncertainties is explained in the main text. Also shown are the GDH sum rule expectation and the results of the fit applied to the theoretical predictions.

Data set	b [GeV^{-2}]	c [GeV^{-4}]
World data	$0.182^{\pm 0.016\,\text{(uncor)}}_{\pm 0.040\,\text{(cor)}}$	$-0.124^{\pm 0.089\,\text{(uncor)}}_{\pm 0.112\,\text{(cor)}}$
GDH sum rule [62]	0.0618	–
χEFT Bernard *et al.* [60]	0.07	0.3
χEFT Alarcón *et al.* [61]	0.066(4)	0.25(12)
Burkert-Ioffe [54,55]	0.09	0.3
Pasechnik *et al.* [57]	0.09	0.4
HLFQCD [59]	0.177	−0.067

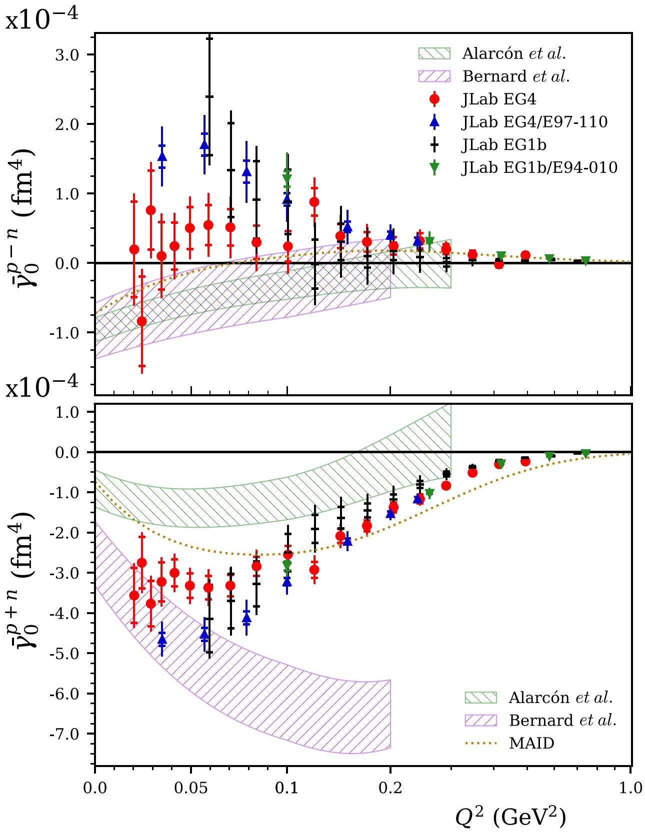

FIG. 26. EG4 results on the isovector (top) and isoscalar (bottom) combinations of the generalized longitudinal spin polarizability $\overline{\gamma}_0(Q^2)$. The EG4-only data are shown by the red circles, compared with the earlier EG1b-only (black crossbars), the combination of EG4 p and E97-110 $n(^3\text{He})$ data (blue triangles), and the combination of EG1b p and E94-010 $n(^3\text{He})$ data (green triangles). For $\overline{\gamma}_0^{p-n}(Q^2)$, the size of the systematic uncertainty varies from 0.026 to 0.522 ($\times 10^{-4}$ fm^4), while the relative size of the systematic to statistical uncertainty varies from (58−216)%. For $\overline{\gamma}_0^{p+n}(Q^2)$, the size of the systematic uncertainty varies from 0.013 to 0.367 ($\times 10^{-4}$ fm^4), while the relative size of the systematic to statistical uncertainty varies from (36−93)%. The results are compared with χEFT predictions from Alarcón *et al.* [61] and Bernard *et al.*, as well as the MAID model. The prediction by Bernard *et al.* [60] does not provide uncertainty bands for the proton-neutron difference; for illustration, we show a band whose width is the larger of the proton and the neutron uncertainties.

nucleon-$\Delta^{(1232)}$ mass difference $m_{N\Delta} \approx 0.3$ GeV must be included in the chiral expansion. Bernard *et al.* [60] treated $m_{N\Delta}$ as a small parameter of the same order as m_π. Alarcón *et al.* [61] used $m_{N\Delta}$ as an intermediate scale so that $m_{N\Delta}/\Lambda_{\chi\text{SB}} \approx m_\pi/m_{N\Delta}$ is the expansion parameter for the π-$\Delta^{(1232)}$ corrections. This is referred to as the "δ-expansion scheme." Additionally, Alarcón *et al.* included a phenomenological form factor, viz. not derived within χEFT, that suppresses the Q^2-dependence of observables at large Q^2. This clearly extends the range of applicability of the Alarcón *et al.* prediction [61] to higher Q^2 compared to that of Bernard *et al.* [60], albeit by introducing an extra scale factor.

An important outcome that can be drawn from the results shown in this section is that χEFT, although successful in many instances, remains challenged by results from dedicated polarized experiments at low Q^2. This includes not only EG4, but also other experiments that used different detectors, methods, and spin observables [71,104,163]. To address this problem, further improvements on χEFT would be required, although it is very difficult to upgrade the predictions to the next order. Since χEFT is the leading QCD-rooted approach to calculating the effects of the strong force at large distances, this difficulty poses a problem in our pursuit of a complete description of nature. Alternatively or complementarily, it would be helpful to have predictions from other nonperturbative approaches to QCD, such as lattice QCD, the Dyson-Schwinger Equations, or the AdS/CFT methods. Recent progress in calculating doubly virtual Compton scattering (VVCS) amplitudes in lattice QCD now makes moments involved in sum rules within reach of this method, see, e.g., Refs. [164,165] for recent development. At present, only calculations for spin-independent VVCS amplitudes are available; these calculations are difficult because they involve computing four-point correlation functions, in contrast to usual Lattice QCD calculations that require less computing-extensive two- and three-point correlations functions. Only recently, advances in methods and computer power have allowed such a computation. There is no difficulty in extending these calculations to computing the spin-flip VVCS amplitudes that enter our sum rules. Our results and their mixed level of agreement with χEFT predictions are strong incentives to extend these calculations to spin-dependent VVCS amplitudes, allowing lattice QCD predictions to be extensively tested.

Apart from tests of fundamental predictions in the hadronic spin sector, our data will also provide input for calculations of two-photon effects in the hyperfine splitting of the hydrogen (or muonic hydrogen) ground state. The lack of proton spin data at low enough Q^2 has made this contribution the dominant source of uncertainty in that calculation. The EG4 longitudinal spin data combined with the transverse spin data from the recent JLab Hall A experiment E08-027 [163] will help to remedy this situation [166].

VIII. SUMMARY AND CONCLUSIONS

In this archival paper, we present the details of the Jefferson Lab EG4 experiment and our final results for proton and the deuteron spin structure function data for Q^2 values as low as 0.012 and 0.017 GeV^2, respectively. We include results on the proton and the deuteron g_1, A_1F_1, and their moments, reported previously in Refs. [21,22], along with details of the simulation and data analysis procedure that led to these results. Our results agree well with previous JLab experiments, but the significantly improved precision of the new data reveal that the world knowledge on low Q^2 spin structure functions, mostly encapsulated in the parametrization [102], must be updated.

We also present new results on the neutron g_1^n and various moments, extracted by combining the corresponding observable of the proton and deuteron and using a simple deuteron model to correct for Fermi smearing and the deuteron D-state component. Our results on the neutron moments agree with earlier results that used polarized ^{3}He targets.

Extrapolating the lowest Q^2 EG4 data $\bar{I}_{\mathrm{TT}}(Q^2)$ to $Q^2 = 0$ provides a check of the GDH sum rule validity, independent from exclusive photoproduction ($Q^2 = 0$) method. This technique using quasireal photons tests the sum rule with a competitive accuracy compared to real photon experiments. It provides results in excellent agreement with the GDH expectation for the proton, and reasonable agreement for the neutron and the deuteron. By combining the proton with neutron results, isovector or isoscalar moments can be formed, which provide complementary tests of theory predictions at low Q^2. We also compared the new results on moments to several phenomenological models, and found a mixed level of success.

Finally, our results test extensively χEFT predictions using eight distinct moments representing diverse x-weightings and isospin components. The new data are of high precision and are at Q^2 values well into domain of χEFT. Despite these advantages and the recent improvements on the χEFT calculation, there is mixed level of agreement between data and χEFT depending on the observable, Q^2 range, and type of calculations. Clearly, χEFT remains challenged by the experimental data at low Q^2. We hope other methods, such as lattice QCD, Dyson-Schwinger Equations, and AdS/CFT, will soon provide predictions that can be compared with experimental results at low Q^2, advancing the theoretical nonperturbative approaches to the strong interaction.

ACKNOWLEDGMENTS

We acknowledge the outstanding efforts of the staff of the Accelerator, the Target Group, and the Physics Divisions at Jefferson Lab that made this experiment possible. This work was supported in part by the U.S. Department of Energy, the U.S. National Science Foundation, the U.S. Jeffress Memorial Trust; the United Kingdom Science and Technology Facilities Council, the Italian Istituto Nazionale di Fisica Nucleare; the French Institut National de Physique Nucléaire et de Physique des Particules, the French Centre National de la Recherche Scientifique; and the National Research Foundation of Korea. J.Z. and X.Z. are supported by the U.S. Department of Energy, Office of Science, Office of Nuclear Physics under Contract No. DE-SC0014434. This material is based upon work supported by the U.S. Department of Energy, Office of Science, Office of Nuclear Physics under contract DE-AC05-06OR23177. We are grateful to J. M. Alarcón, A. Kotikov, R. Pasechnik, and D. Volkova for sending us the predictions from their models.

---

[1] R. Frisch and O. Stern, Magnetic deviation of hydrogen molecules and the magnetic moment of the proton. I, Z. Phys. **85**, 4 (1933).

[2] I. Esterman and O. Stern, Magnetic deviation of hydrogen molecules and the magnetic moment of the proton. II, Z. Phys. **85**, 17 (1933).

[3] R. Hofstadter, H. R. Fechter, and J. A. McIntyre, Scattering of high-energy electrons and the method of nuclear recoil, Phys. Rev. **91**, 422 (1953).

[4] S. Narison, *QCD as a Theory of Hadrons—From Partons to Confinement, Cambridge Monographs on Particle Physics, Nuclear Physics and Cosmology* (Cambridge University Press, Cambridge, UK, 2004).

[5] R. Roberts, *The Structure of the Proton, Cambridge Monographs on Mathematical Physics* (Cambridge University Press, Cambridge, UK, 1990).

[6] G. M. Prosperi, M. Raciti, and C. Simolo, On the running coupling constant in QCD, Prog. Part. Nucl. Phys. **58**, 387 (2007).

[7] A. Deur, S. J. Brodsky, and G. F. de Téramond, The QCD running coupling, Prog. Part. Nucl. Phys. **90**, 1 (2016).

[8] A. Deur, S. J. Brodsky, and C. D. Roberts, QCD running couplings and effective charges, Prog. Part. Nucl. Phys. **134**, 104081 (2024).

[9] V. Bernard, N. Kaiser, and U.-G. Meissner, Chiral dynamics in nucleons and nuclei, Int. J. Mod. Phys. E **04**, 193 (1995).

[10] M. Anselmino, A. Efremov, and E. Leader, The theory and phenomenology of polarized deep inelastic scattering, Phys. Rep. **261**, 1 (1995).

[11] S. D. Bass, The spin structure of the proton, Rev. Mod. Phys. **77**, 1257 (2005).

[12] J.-P. Chen, A. Deur, and Z.-E. Meziani, Sum rules and moments of the nucleon spin structure functions, Mod. Phys. Lett. A **20**, 2745 (2005).

[13] M. Burkardt, C. A. Miller, and W. D. Nowak, Spin-polarized high-energy scattering of charged leptons on nucleons, Rep. Prog. Phys. **73**, 016201 (2010).

[14] S. E. Kuhn, J. P. Chen, and E. Leader, Spin structure of the nucleon—Status and recent results, Prog. Part. Nucl. Phys. **63**, 1 (2009).

[15] J. P. Chen, Moments of spin structure functions: Sum rules and polarizabilities, Int. J. Mod. Phys. E **19**, 1893 (2010).

[16] C. A. Aidala, S. D. Bass, D. Hasch, and G. K. Mallot, The spin structure of the nucleon, Rev. Mod. Phys. **85**, 655 (2013).

[17] A. Deur, S. J. Brodsky, and G. F. De Téramond, The spin structure of the nucleon, Rep. Prog. Phys. **82**, 076201 (2019).

[18] X. Ji, F. Yuan, and Y. Zhao, What we know and what we don't know about the proton spin after 30 years, Nat. Rev. Phys. **3**, 27 (2021).

[19] M. Amarian *et al.* (Jefferson Lab E94-010 Collaboration), Measurement of the generalized forward spin polarizabilities of the neutron, Phys. Rev. Lett. **93**, 152301 (2004).

[20] B. A. Mecking *et al.*, The CEBAF Large Acceptance Spectrometer (CLAS), Nucl. Instrum. Methods Phys. Res., Sect. A **503**, 513 (2003).

[21] K. P. Adhikari *et al.* (CLAS Collaboration), Measurement of the Q^2 dependence of the deuteron spin structure function g_1 and its moments at low Q^2 with CLAS, Phys. Rev. Lett. **120**, 062501 (2018).

[22] X. Zheng *et al.* (CLAS Collaboration), Measurement of the proton spin structure at long distances, Nat. Phys. **17**, 736 (2021).

[23] X. Zheng *et al.* (CLAS Collaboration), Measurement of target and double-spin asymmetries for the $\vec{e}\vec{p} \to e\pi^+(n)$ reaction in the nucleon resonance region at low Q^2, Phys. Rev. C **94**, 045206 (2016).

[24] See Supplemental Material at http://link.aps.org/supplemental/10.1103/PhysRevC.111.035202 for all the results on the structure functions and their moments reported in this article.

[25] J. D. Bjorken, Asymptotic sum rules at infinite momentum, Phys. Rev. **179**, 1547 (1969).

[26] D. Drechsel, S. S. Kamalov, and L. Tiator, The GDH sum rule and related integrals, Phys. Rev. D **63**, 114010 (2001).

[27] M. Gorchtein, D. Drechsel, M. M. Giannini, E. Santopinto, and L. Tiator, Generalized sum rules of the nucleon in the constituent quark model, Phys. Rev. C **70**, 055202 (2004).

[28] J. D. Bjorken, Applications of the chiral $U(6) \times U(6)$ algebra of current densities, Phys. Rev. **148**, 1467 (1966).

[29] J. D. Bjorken, Inelastic scattering of polarized leptons from polarized nucleons, Phys. Rev. D **1**, 1376 (1970).

[30] A. L. Kataev, The ellis-jaffe sum rule: The estimates of the next to next-to-leading order QCD corrections, Phys. Rev. D **50**, R5469 (1994).

[31] A. L. Kataev, Deep inelastic sum rules at the boundaries between perturbative and nonperturbative QCD, Mod. Phys. Lett. A **20**, 2007 (2005).

[32] P. A. Baikov, K. G. Chetyrkin, and J. H. Kuhn, Adler function, Bjorken sum rule, and the Crewther relation to order α_s^4 in a general gauge theory, Phys. Rev. Lett. **104**, 132004 (2010).

[33] B. Adeva *et al.* (Spin Muon Collaboration), Measurement of the spin dependent structure function $g_1(x)$ of the deuteron, Phys. Lett. B **302**, 533 (1993).

[34] B. Adeva *et al.* (Spin Muon (SMC) Collaboration), The spin dependent structure function $g_1(\mathrm{x})$ of the proton from polarized deep inelastic muon scattering, Phys. Lett. B **412**, 414 (1997).

[35] D. Adams *et al.* (Spin Muon (SMC) Collaboration), Measurement of the spin dependent structure function $g_1(x)$ of the proton, Phys. Lett. B **329**, 399 (1994).

[36] D. Adams *et al.* (Spin Muon Collaboration), A new measurement of the spin dependent structure function $g_1(x)$ of the deuteron, Phys. Lett. B **357**, 248 (1995).

[37] D. Adams *et al.* (Spin Muon (SMC) Collaboration), The spin dependent structure function $g_1(x)$ of the deuteron from polarized deep inelastic muon scattering, Phys. Lett. B **396**, 338 (1997).

[38] D. Adams *et al.* (Spin Muon (SMC) Collaboration), Spin structure of the proton from polarized inclusive deep inelastic muon - proton scattering, Phys. Rev. D **56**, 5330 (1997).

[39] M. G. Alekseev *et al.* (COMPASS Collaboration), The spin-dependent structure function of the proton g_1^p and a test of the Bjorken sum rule, Phys. Lett. B **690**, 466 (2010).

[40] C. Adolph *et al.* (COMPASS Collaboration), The spin structure function g_1^{p} of the proton and a test of the bjorken sum rule, Phys. Lett. B **753**, 18 (2016).

[41] C. Adolph *et al.* (COMPASS Collaboration), Final compass results on the deuteron spin-dependent structure function g_1^{d} and the bjorken sum rule, Phys. Lett. B **769**, 34 (2017).

[42] A. Airapetian *et al.* (HERMES Collaboration), The Q^2 dependence of the generalized Gerasimov-Drell-Hearn integral for the deuteron, proton and neutron, Eur. Phys. J. C **26**, 527 (2003).

[43] A. Deur *et al.*, Experimental determination of the evolution of the Bjorken integral at low Q^2, Phys. Rev. Lett. **93**, 212001 (2004).

[44] A. Deur *et al.*, Experimental study of isovector spin sum rules, Phys. Rev. D **78**, 032001 (2008).

[45] A. Deur, Y. Prok, V. Burkert, D. Crabb, F.X. Girod, K.A. Griffioen, N. Guler, S.E. Kuhn, and N. Kvaltine, High precision determination of the Q^2 evolution of the Bjorken sum, Phys. Rev. D **90**, 012009 (2014).

[46] K. Abe *et al.*, Precision measurement of the deuteron spin structure function g_1^d, Phys. Rev. Lett. **75**, 25 (1995).

[47] K. Abe *et al.* (E143 Collaboration), Measurements of the Q^2 dependence of the proton and deuteron spin structure functions g_1^d and g_1^d, Phys. Lett. B **364**, 61 (1995).

[48] K. Abe *et al.* (E154 Collaboration), Precision determination of the neutron spin structure function g_1^n, Phys. Rev. Lett. **79**, 26 (1997).

[49] K. Abe *et al.* (E143 Collaboration), Measurements of the proton and deuteron spin structure functions g_1 and g_2, Phys. Rev. D **58**, 112003 (1998).

[50] K. Abe *et al.* (E154 Collaboration), Next-to-leading order QCD analysis of polarized deep inelastic scattering data, Phys. Lett. B **405**, 180 (1997).

[51] P. L. Anthony *et al.* (E155 Collaboration), Measurements of the Q^2 dependence of the proton and neutron spin structure functions g_1^p and g_1^n, Phys. Lett. B **493**, 19 (2000).

[52] K. Slifer *et al.* (Resonance Spin Structure Collaboration), Probing quark-gluon interactions with transverse polarized scattering, Phys. Rev. Lett. **105**, 101601 (2010).

[53] A. Deur *et al.*, Experimental study of the behavior of the Bjorken sum at very low Q^2, Phys. Lett. B **825**, 136878 (2022).

[54] V. D. Burkert and B. L. Ioffe, On the Q^2 variation of spin-dependent deep-inelastic electron-proton scattering, Phys. Lett. B **296**, 223 (1992).

[55] V. D. Burkert and B. L. Ioffe, Polarized structure functions of proton and neutron and the Gerasimov-Drell-Hearn and Bjorken sum rules, J. Exp. Theor. Phys. **78**, 619 (1994).

[56] J. Soffer and O. Teryaev, QCD radiative and power corrections and generalized GDH sum rules, Phys. Rev. D **70**, 116004 (2004).

[57] R. S. Pasechnik, J. Soffer, and O. V. Teryaev, Nucleon spin structure at low momentum transfers, Phys. Rev. D **82**, 076007 (2010).

[58] R. S. Pasechnik, D. V. Shirkov, O. V. Teryaev, O. P. Solovtsova, and V. L. Khandramai, Nucleon spin structure and pQCD frontier on the move, Phys. Rev. D **81**, 016010 (2010).

[59] S. J. Brodsky, G. F. de Téramond, and A. Deur, Nonperturbative QCD coupling and its β-function from light-front holography, Phys. Rev. D **81**, 096010 (2010).

[60] V. Bernard, E. Epelbaum, H. Krebs, and Ulf-G. Meissner, New insights into the spin structure of the nucleon, Phys. Rev. D **87**, 054032 (2013).

[61] J. M. Alarcón, F. Hagelstein, V. Lensky, and V. Pascalutsa, Forward doubly-virtual Compton scattering off the nucleon in chiral perturbation theory: II. Spin polarizabilities and moments of polarized structure functions, Phys. Rev. D **102**, 114026 (2020).

[62] S. B. Gerasimov, A sum rule for magnetic moments and the damping of the nucleon magnetic moment in nuclei, Yad. Fiz. **2**, 598 (1965).

[63] S. D. Drell and A. C. Hearn, Exact sum rule for nucleon magnetic moments, Phys. Rev. Lett. **16**, 908 (1966).

[64] K. Helbing, The Gerasimov-Drell-Hearn sum rule, Prog. Part. Nucl. Phys. **57**, 405 (2006).

[65] J. Ahrens *et al.* (GDH, A2 Collaboration), First measurement of the Gerasimov-Drell-Hearn integral for hydrogen from 200 to 800 MeV, Phys. Rev. Lett. **87**, 022003 (2001).

[66] J. Ahrens *et al.*, Measurement of the Gerasimov-Drell-Hearn integrand for H-2 from 200-MeV to 800-MeV, Phys. Rev. Lett. **97**, 202303 (2006).

[67] H. Dutz *et al.* (GDH Collaboration), First measurement of the Gerasimov-Drell-Hearn sum rule for H-1 from 0.7-GeV to 1.8-GeV at ELSA, Phys. Rev. Lett. **91**, 192001 (2003).

[68] H. Dutz *et al.* (GDH Collaboration), Measurement of helicity-dependent photoabsorption cross sections on the neutron from 815-MeV to 1825-MeV, Phys. Rev. Lett. **94**, 162001 (2005).

[69] H. Dutz *et al.*, Experimental check of the Gerasimov-Drell-Hearn sum rule for H-1, Phys. Rev. Lett. **93**, 032003 (2004).

[70] S. Hoblit *et al.* (LSC Collaboration), Measurements of H-polarized D-polarized (gamma-polarized, pi) and implications for convergence of the GDH integral, Phys. Rev. Lett. **102**, 172002 (2009).

[71] V. Sulkosky *et al.* (Jefferson Lab E97-110 Collaboration), Measurement of the ^{3}He spin-structure functions and of neutron (3He) spin-dependent sum rules at $0.035 \leqslant \mathrm{Q}^2 \leqslant 0.24$ GeV^2, Phys. Lett. B **805**, 135428 (2020).

[72] F. Renard (GRAAL Collaboration), Polarisation program at GRAAL and GDH, in *Symposium on the Gerasimov-Drell-Hearn Sum Rule and the Nucleon Spin Structure in the Resonance Region (GDH 2000), Mainz, Germany, 14–17 June 2000*, edited by D. Drechsel and L. Tiator (World Scientific, 2000), pp. 299–306.

[73] H. R. Weller (TUNL, GDH Collaboration), A study of the GDH sum rule integrand for the deuteron at TUNL and HIgammas near photodisintegration threshold, in *2nd International Symposium on the Gerasimov-Drell-Hearn Sum Rule and the Spin Structure of the Nucleon (GDH 2002), Genova, Italy, July 3–6, 2002* (World Scientific, 2002), pp. 173–182.

[74] I. Strakovsky, S. Širca, W. J. Briscoe, A. Deur, A. Schmidt, and R. L. Workman, Single-pion contribution to the Gerasimov-Drell-Hearn sum rule and related integrals, Phys. Rev. C **105**, 045202 (2022).

[75] M. Anselmino, B. L. Ioffe, and E. Leader, On possible resolutions of the spin crisis in the parton model, Sov. J. Nucl. Phys. **49**, 136 (1989).

[76] X.-D. Ji and J. Osborne, Generalized sum rules for spin dependent structure functions of the nucleon, J. Phys. G: Nucl. Part. Phys. **27**, 127 (2001).

[77] F. E. Low, Scattering of light of very low frequency by systems of spin 1/2, Phys. Rev. **96**, 1428 (1954).

[78] J. R. Ellis and R. L. Jaffe, A sum rule for deep inelastic electroproduction from polarized protons, Phys. Rev. D **9**, 1444 (1974).

[79] X.-D. Ji, C.-W. Kao, and J. Osborne, Generalized Drell-Hearn-Gerasimov sum rule at order $\mathrm{O}(\mathrm{p}^4)$ in chiral perturbation theory, Phys. Lett. B **472**, 1 (2000).

[80] X.-D. Ji, C.-W. Kao, and J. Osborne, The nucleon spin polarizability at order $\mathrm{O}(\mathrm{p}^4)$ in chiral perturbation theory, Phys. Rev. D **61**, 074003 (2000).

[81] V. Bernard, T. R. Hemmert, and U.-G. Meissner, Novel analysis of chiral loop effects in the generalized Gerasimov-Drell-Hearn sum rule, Phys. Lett. B **545**, 105 (2002).

[82] V. Bernard, T. R. Hemmert, and Ulf-G. Meissner, Spin structure of the nucleon at low-energies, Phys. Rev. D **67**, 076008 (2003).

[83] C. W. Kao, T. Spitzenberg, and M. Vanderhaeghen, Burkhardt-Cottingham sum rule and forward spin polarizabilities in heavy baryon chiral perturbation theory, Phys. Rev. D **67**, 016001 (2003).

[84] V. Lensky, J. M. Alarcón, and V. Pascalutsa, Moments of nucleon structure functions at next-to-leading order in baryon chiral perturbation theory, Phys. Rev. C **90**, 055202 (2014).

[85] V. Lensky, V. Pascalutsa, and M. Vanderhaeghen, Generalized polarizabilities of the nucleon in baryon chiral perturbation theory, Eur. Phys. J. C **77**, 119 (2017).

[86] J. Ashman *et al.* (European Muon Collaboration), A measurement of the spin asymmetry and determination of the structure function g_1 in deep inelastic muon-proton scattering, Phys. Lett. B **206**, 364 (1988).

[87] E. S. Ageev *et al.* (COMPASS Collaboration), Measurement of the spin structure of the deuteron in the dis region, Phys. Lett. B **612**, 154 (2005).

[88] V. Y. Alexakhin *et al.* (COMPASS Collaboration), The deuteron spin-dependent structure function g_1^d and its first moment, Phys. Lett. B **647**, 8 (2007).

[89] M. Aghasyan *et al.* (COMPASS Collaboration), Longitudinal double-spin asymmetry a_1^{p} and spin-dependent structure function g_1^{p} of the proton at small values of x and q^2, Phys. Lett. B **781**, 464 (2018).

[90] A. Airapetian *et al.* (HERMES Collaboration), The Q^2 dependence of the generalized Gerasimov-Drell-Hearn integral for the proton, Phys. Lett. B **494**, 1 (2000).

[91] K. Ackerstaff *et al.* (HERMES Collaboration), Determination of the deep inelastic contribution to the generalized Gerasimov-Drell-Hearn integral for the proton and neutron, Phys. Lett. B **444**, 531 (1998).

[92] M. Amarian *et al.*, The Q^2 evolution of the generalized Gerasimov-Drell-Hearn integral for the neutron using a ^{3}He target, Phys. Rev. Lett. **89**, 242301 (2002).

[93] M. Amarian *et al.* (Jefferson Lab E94-010 Collaboration), Q^2 evolution of the neutron spin structure moments using a ^{3}He target, Phys. Rev. Lett. **92**, 022301 (2004).

[94] J. Yun *et al.* (CLAS Collaboration), Measurement of inclusive spin structure functions of the deuteron, Phys. Rev. C **67**, 055204 (2003).

[95] R. Fatemi *et al.* (CLAS Collaboration), Measurement of the proton spin structure function $g_1(x, Q^2)$ for Q^2 from 0.15 to 1.6 GeV^2 with CLAS, Phys. Rev. Lett. **91**, 222002 (2003).

[96] F. R. Wesselmann *et al.* (RSS Collaboration), Proton spin structure in the resonance region, Phys. Rev. Lett. **98**, 132003 (2007).

[97] K. V. Dharmawardane *et al.* (CLAS Collaboration), Measurement of the x- and Q^2-dependence of the asymmetry A_1 on the nucleon, Phys. Lett. B **641**, 11 (2006).

[98] Y. Prok *et al.* (CLAS Collaboration), Moments of the spin structure functions g_1^p and g_1^d for $0.05 < Q^2 < 3.0$-GeV^2, Phys. Lett. B **672**, 12 (2009).

[99] P. Solvignon *et al.* (Jefferson Lab E01-012 Collaboration), Quark-hadron duality in neutron (^{3}He) spin structure, Phys. Rev. Lett. **101**, 182502 (2008).

[100] P. Solvignon *et al.* (E01-012 Collaboration), Moments of the neutron g_2 structure function at intermediate q^2, Phys. Rev. C **92**, 015208 (2015).

[101] Y. Prok *et al.* (CLAS Collaboration), Precision measurements of g_1 of the proton and the deuteron with 6 GeV electrons, Phys. Rev. C **90**, 025212 (2014).

[102] R. Fersch *et al.* (CLAS Collaboration), Determination of the proton spin structure functions for $0.05 < Q^2 < 5\,\mathrm{GeV}^2$ using CLAS, Phys. Rev. C **96**, 065208 (2017).

[103] N. Guler *et al.* (CLAS Collaboration), Precise determination of the deuteron spin structure at low to moderate Q^2 with CLAS and extraction of the neutron contribution, Phys. Rev. C **92**, 055201 (2015).

[104] V. Sulkosky *et al.* (E97-110 Collaboration), Measurement of the generalized spin polarizabilities of the neutron in the low-Q^2 region, Nat. Phys. **17**, 687 (2021).

[105] P. L. Anthony *et al.* (E142 Collaboration), Deep inelastic scattering of polarized electrons by polarized ^{3}He and the study of the neutron spin structure, Phys. Rev. D **54**, 6620 (1996).

[106] K. Abe *et al.* (E143 Collaboration), Precision measurement of the proton spin structure function g_1^d, Phys. Rev. Lett. **74**, 346 (1995).

[107] K. Abe *et al.* (E143 Collaboration), Measurements of the proton and deuteron spin structure function g_1 in the resonance region, Phys. Rev. Lett. **78**, 815 (1997).

[108] P. L. Anthony *et al.* (E155 Collaboration), Measurement of the deuteron spin structure function $g_1^d(x)$ for 1-(GeV/c)$^2 < Q^2 <$ 40-(GeV/c)^2, Phys. Lett. B **463**, 339 (1999).

[109] F. Hagelstein, R. Miskimen, and V. Pascalutsa, Nucleon polarizabilities: from Compton scattering to hydrogen atom, Prog. Part. Nucl. Phys. **88**, 29 (2016).

[110] M. Gell-Mann, M. L. Goldberger, and W. E. Thirring, Use of causality conditions in quantum theory, Phys. Rev. **95**, 1612 (1954).

[111] P. A. M. Guichon, G. Q. Liu, and A. W. Thomas, Virtual compton scattering and generalized polarizabilities of the proton, Nucl. Phys. A **591**, 606 (1995).

[112] D. Drechsel, B. Pasquini, and M. Vanderhaeghen, Dispersion relations in real and virtual Compton scattering, Phys. Rep. **378**, 99 (2003).

[113] D. Drechsel, O. Hanstein, S. S. Kamalov, and L. Tiator, A unitary isobar model for pion photoproduction and electroproduction on the proton up to 1-GeV, Nucl. Phys. A **645**, 145 (1999).

[114] R. L. Workman, M. W. Paris, W. J. Briscoe, and I. I. Strakovsky, Unified Chew-Mandelstam SAID analysis of pion photoproduction data, Phys. Rev. C **86**, 015202 (2012).

[115] Y. Kahn, W. Melnitchouk, and S. A. Kulagin, New method for extracting neutron structure functions from nuclear data, Phys. Rev. C **79**, 035205 (2009).

[116] M. Lacombe, B. Loiseau, J. M. Richard, R. Vinh Mau, J. Cote, P. Pires, and R. de Tourreil, Parametrization of the Paris n n potential, Phys. Rev. C **21**, 861 (1980).

[117] R. Machleidt, K. Holinde, and C. Elster, The Bonn meson exchange model for the nucleon nucleon interaction, Phys. Rep. **149**, 1 (1987).

[118] M. J. Zuilhof and J. A. Tjon, Electromagnetic properties of the deuteron and the Bethe-Salpeter equation with one boson exchange, Phys. Rev. C **22**, 2369 (1980).

[119] K. Kotthoff, R. Machleidt, and D. Schutte, Meson exchange corrections and properties of nuclear matter and neutron matter, Nucl. Phys. A **264**, 484 (1976).

[120] B. Desplanques, Deuteron D state probability and energy dependent NN interactions, Phys. Lett. B **203**, 200 (1988).

[121] M. Battaglieri, R. De Vita, A. Deur, and M. Ripani, The GDH sum rule with nearly real photons and the proton g_1 structure function at low momentum transfer, Jefferson Lab Experiment E03-006, 2003.

[122] A. Deur, D. G, and K. Slifer, Measurement of the Gerasimov-Drell-Hearn integral at low Q^2 on the neutron and deuteron, Jefferson Lab Experiment E05-011, 2005.

[123] J. S. Price, B. M. Poelker, C. K. Sinclair, P. M. Rutt, D. J. Mack, and J. M. Grames, Recent measurements with the Jefferson Lab 5-MeV Mott polarimeter, in *13th International Symposium on High-Energy Spin Physics (SPIN 98), 8–12 September 1998, Protvino, Russian Federation* (World Scientific, 1998), pp. 554–556.

[124] G. A. Krafft, J. C. Denard, R. W. Dickson, R. Kazimi, V. A. Lebedev, and M. G. Tiefenback, Measuring and controlling the energy spread in CEBAF, eConf **C00082**, TH205 (2000).

[125] D. G. Crabb and D. B. Day, The Virginia/Basel/SLAC polarized target: Operation and performance during experiment E143 at slac, Nucl. Instrum. Methods Phys. Res., Sect. A **356**, 9 (1995).

[126] C. D. Keith *et al.*, A polarized target for the CLAS detector, Nucl. Instrum. Methods Phys. Res., Sect. A **501**, 327 (2003).

[127] M. Osipenko, A. Vlassov, and M. Taiuti, Matching between the electron candidate track and the cherenkov counter hit, JLab CLAS-Note 2004-020, CLAS notes archive, 2004.

[128] M. U. Mozer and D. S. Carman, Comparison of GSIM Monte Carlo and geometric acceptance functions for CLAS, JLab CLAS note 2002-005, CLAS notes archive, 2002.

[129] M. Bellis, Reliability and limitations of GSIM, JLab CLAS note 2002-016, CLAS notes archive (2002).

[130] J. Arrington, W. Melnitchouk, and J. A. Tjon, Global analysis of proton elastic form factor data with two-photon exchange corrections, Phys. Rev. C **76**, 035205 (2007).

[131] L. W. Mo and Y.-S. Tsai, Radiative corrections to elastic and inelastic ep and up scattering, Rev. Mod. Phys. **41**, 205 (1969).

[132] Y.-S. Tsai, Pair production and bremsstrahlung of charged leptons, Rev. Mod. Phys. **46**, 815 (1974).

[133] H. Olsen and L. C. Maximon, Photon and electron polarization in high-energy bremsstrahlung and pair production with screening, Phys. Rev. **114**, 887 (1959).

[134] T. V. Kuchto and N. M. Shumeiko, Radiative effects in deep inelastic scattering of polarized leptons by polarized nucleons, Nucl. Phys. B **219**, 412 (1983).

[135] G. Kubon *et al.*, Precise neutron magnetic form-factors, Phys. Lett. B **524**, 26 (2002).

[136] R. Madey *et al.* (E93-038 Collaboration), Measurements of G_E^n/G_M^n from the $^2\mathrm{H}(\vec{e}, e'\vec{n})^1\mathrm{H}$ reaction to $Q^2 = 1.45\,(\mathrm{GeV}/c)^2$, Phys. Rev. Lett. **91**, 122002 (2003).

[137] W. A. Maniatty and P. Stoler, An extended RECSIS tutorial, Available on CiteSeerX, 1997.

[138] J. Arrington, Implications of the discrepancy between proton form-factor measurements, Phys. Rev. C **69**, 022201(R) (2004).

[139] K. Griffioen, C. Carlson, and S. Maddox, Consistency of electron scattering data with a small proton radius, Phys. Rev. C **93**, 065207 (2016).

[140] M. Osipenko *et al.* (CLAS Collaboration), A kinematically complete measurement of the proton structure function F_2 in the resonance region and evaluation of its moments, Phys. Rev. D **67**, 092001 (2003).

[141] P. E. Bosted and M. E. Christy, Empirical fit to inelastic electron-deuteron and electron-neutron resonance region transverse cross-sections, Phys. Rev. C **77**, 065206 (2008).

[142] M. E. Christy and P. E. Bosted, Empirical fit to precision inclusive electron-proton cross- sections in the resonance region, Phys. Rev. C **81**, 055213 (2010).

[143] H. Burkhardt and W. N. Cottingham, Sum rules for forward virtual Compton scattering, Ann. Phys. **56**, 453 (1970).

[144] J. Soffer, Positivity constraints for spin dependent parton distributions, Phys. Rev. Lett. **74**, 1292 (1995).

[145] K. Ackerstaff *et al.* (HERMES Collaboration), Measurement of the neutron spin structure function g_1^n with a polarized ^{3}He internal target, Phys. Lett. B **404**, 383 (1997).

[146] A. Airapetian *et al.* (HERMES Collaboration), Precise determination of the spin structure function g_1 of the proton, deuteron and neutron, Phys. Rev. D **75**, 012007 (2007).

[147] X. Zheng *et al.* (Jefferson Lab Hall A Collaboration), Precision measurement of the neutron spin asymmetries and spin-dependent structure functions in the valence quark region, Phys. Rev. C **70**, 065207 (2004).

[148] S. Wandzura and F. Wilczek, Sum rules for spin dependent electroproduction: Test of relativistic constituent quarks, Phys. Lett. B **72**, 195 (1977).

[149] P. L. Anthony *et al.* (E155 Collaboration), Precision measurement of the proton and deuteron spin structure functions g_2 and asymmetries A_2, Phys. Lett. B **553**, 18 (2003).

[150] E. B. Dally, M. G. Croissiaux, and B. Schweitz, Scattering of high-energy electrons by nitrogen-14 and -15, Phys. Rev. C **2**, 2057 (1970).

[151] V. D. Burkert, Comment on the generalized Gerasimov-Drell-Hearn sum rule in chiral perturbation theory, Phys. Rev. D **63**, 097904 (2001).

[152] V. Bernard, N. Kaiser, and Ulf-G. Meissner, Small momentum evolution of the extended Drell-Hearn-Gerasimov sum rule, Phys. Rev. D **48**, 3062 (1993).

[153] G. M. Gurevich and V. P. Lisin, Measurement of the proton spin polarizabilities at MAMI, Phys. Part. Nucl. **48**, 111 (2017).

[154] F. Bigazzi and F. Castellani, Resonance contributions to nucleon spin structure in holographic QCD, J. High Energy Phys. 04 (2024) 037.

[155] J. M. Maldacena, The large n limit of superconformal field theories and supergravity, Adv. Theor. Math. Phys. **2**, 231 (1998).

[156] S. J. Brodsky, G. F. de Téramond, H. G. Dosch, and J. Erlich, Light-front holographic QCD and emerging confinement, Phys. Rep. **584**, 1 (2015).

[157] G. Grunberg, Renormalization group improved perturbative QCD, Phys. Lett. B **95**, 70 (1980).

[158] A. Deur, V. Burkert, J.-P. Chen, and W. Korsch, Experimental determination of the effective strong coupling constant, Phys. Lett. B **650**, 244 (2007).

[159] A. Deur, V. Burkert, J. P. Chen, and W. Korsch, Determination of the effective strong coupling constant $\alpha_{s,g_1}(Q^2)$ from CLAS spin structure function data, Phys. Lett. B **665**, 349 (2008).

[160] A. Deur, V. Burkert, J. P. Chen, and W. Korsch, Experimental determination of the QCD effective charge $\alpha_{g_1}(Q)$, Particles **5**, 171 (2022).

[161] I. R. Gabdrakhmanov, N. A. Gramotkov, A. V. Kotikov, D. A. Volkova, and I. A. Zemlyakov, Bjorken sum rule with analytic coupling at low Q2 values, JETP Lett. **118**, 478 (2023).

[162] C. Ciofi degli Atti and S. Scopetta, On the extraction of the neutron spin structure functions and the Gerasimov-Drell-Hearn integral from $^3\vec{\mathrm{H}}\mathrm{e}(\vec{e}, e')$, Phys. Lett. B **404**, 223 (1997).

[163] D. Ruth *et al.* (Jefferson Lab Hall A g_2^p Collaboration), Proton spin structure and generalized polarizabilities in the strong quantum chromodynamics regime, Nat. Phys. **18**, 1441 (2022).

[164] F. X. Lee, W. Wilcox, A. Alexandru, and C. Culver, Magnetic polarizability of a charged pion from four-point functions in lattice QCD, Phys. Rev. D **108**, 054510 (2023).

[165] X.-H. Wang, C.-L. Fan, X. Feng, L.-C. Jin, and Z.-L. Zhang, Nucleon electric polarizabilities and nucleon-pion scattering at physical pion mass, Phys. Rev. Lett. **133**, 141901 (2024).

[166] D. Ruth *et al.*, New spin structure constraints on hyperfine splitting and proton size, Phys. Lett. B **859**, 139116 (2024).